Università degli Studi di Pisa
Facoltà di Ingegneria

Corso di Laurea in

Ingegneria Meccanica

Study of electromechanical effects in high field accelerator magnets

Tesi di

Marco Danuso

Relatori:

Prof. Ing. M. Beghini

Dott. A. Zlobin

Dott. Ing. E. Barzi

Anno Accademico 2007-2008

Aknowledgment

I would like to thank all the people who helped me during these months of work at Fermilab. In particular my supervisors Emanuela Barzi and Alexander Zlobin, who guided and stimulated me in solving the most critical problems; Danuele Turrioni, for always having a good piece of advice; Al Rusy and Tom Van Raes, who provided essential help in laboratory work with his vast experience; all the people who came at my presentations, for making me feel important.

I also want to thank Kristine Ewald, for hanging out with my sister, and Marco Trovato for the mind–blowing trip to Six Flags; Emanuela, Prashant, Hideyuki, Vito, Gabriella for making me feel at home overseas.

Finally, many thanks to Emanuela Barzi, Alezander Zlobin, Mike Lamm and my family who gave me this unique opportunity to visit and do research in such a great laboratory as Fermilab.

Contents

List of Figures

Abstract **– Future upgrades of machines like the LHC at CERN require pushing accelerator magnets beyond 10 T. Larger magnet sizes and more performing superconductors introduce additional challenges. This work improves existing analytical models of the magnetic field and stress of dipole and quadrupole sector windings, addressing how far the engineering of High Field Magnets can be pushed. Problems and limitations of Nb3Sn magnets are identified by correlating the field intensity and the loss of field quality to the magnetic and mechanical properties of the material.**

Chapter 1

The Fermi National Accelerator Laboratory

1.1 Introduction

A substantial effort is presently spent at Fermilab in developing new high field superconducting magnets for next generation accelerators. The vanishing electrical resistance of superconducting coils and their ability to provide magnetic fields far beyond those of saturated iron is the main motivation for the use of superconductor technology in every new large proton, antiproton and heavy ion circular accelerators. Superconductivity does not only open the way to much higher particle energies, but at the same time leads to a substantial reduction of operating costs. Beam energies in the TeV regime are hardly accessible with standard technology, due to the enormous power they would require. The electrical power consumption of an accelerator cryogenic plant may easily be 1–2 orders of magnitude lower than the power needed in an equivalent warm machine of the same energy. Following a hypothetical trace that starts from current generation accelerator machines (in particular Fermilab accelerators), and brings us to explore their main constituents, the superconducting magnets, up to cables and wires, that are the magnet core, we will then describe the next generation machines and the research and development programs performed at the Fermilab Technical Division (TD).

1.2 High energy accelerators

High energy accelerators are mainly motivated by the need of completing our present understanding of the Standard Model, which includes the origin of symmetry breaking of electroweak interactions of elementary particles, the

Figure 1.1: Fermilab site.

origin of their masses and of the masses of the force carriers and the reason why matter predominates over anti–matter in the universe. Future observations could lead to extend the theory and hopefully reach the unification of gravity with the other forces. New observations might also lead to understand what is the composition of dark matter in the universe. These searches are carried out by smashing particles of very high energy into each other, and by analysing the nature and the characteristics of the new particles produced at the expense of the collision energy. These interactions are obtained either by blasting high momentum particles onto a fixed target or by making them collide head–on among themselves. In head–on colliders, in order to achieve high event rates, the particles are bunched together and the bunches are formatted into high intensity beams. For the deepest studies of particle structures and for the production of more massive new particles, higher and higher energies are needed, and of course the more complex are the accelerators. Accelerators can be divided in two types: *linear accelerators* and *circular accelerators*.

In a *linear accelerator*, charged particles travel along a straight trajectory and go through a number of accelerating structures. An outstanding example is the 45 GeV electron/positron LINAC at SLAC, Stanford University, CA, USA.

Two international projects are trying to fix the energy limit for these machines to the TeV level, building an e^+/e^- linear accelerator. The first one is

the Next Linear Collider (NLC) a 32 Km long warm accelerator mostly supported by a US–Japan collaboration. The second is TESLA (TeV Energy Superconducting Linear Accelerator) a 33 km long superconducting accelerator mostly supported by the European countries. Moreover two other projects are pursued: CLIC (Compact Linear Collider) at CERN and JLC at KEK. These project are more ambitious but in an earlier R&D stage.

In a *circular accelerator*, the beam is circulated many times in the closed orbit along which a number of accelerating stations are present. Bending magnets and focusing elements are distributed over the accelerator arcs to keep the particles, during and after acceleration, on the same orbit and within the accelerator acceptance.

Beside the Tevatron, which will be described in more detail below, LHC at CERN, Geneva, Switzerland, and HERA at DESY, Hamburg, Germany, are examples of circular accelerators.

LHC will be activated in 2008. It is a proton–proton Collider of maximum energy 7x7 TeV. HERA is a proton–electron collider, whose superconducting proton ring has an energy of 820 GeV, whereas its electron/positron ring has an energy of 28 GeV.

1.3 The Tevatron

Fermilab was started in 1967. The first large circular accelerator operating on site was the Main Ring with its injection stages consisting of a proton source, a linear accelerator (LINAC) and a Booster ring. The Main Ring, shown at the center of Fig. 1.2, had a circumference of 6.2 Km. The proton beam had a maximum energy of 450 GeV. It was ejected and used against fixed targets.

A few years later, the Tevatron, the first accelerator made with superconducting magnets, was built in the same tunnel. The Main Ring served as last injection element to the Tevatron. The proton beam energy doubled to 900 GeV. In 1984, the Antiproton Source became integral part of Fermilab accelerator complex, allowing the Tevatron to operate as a proton–antiproton collider with a center of mass energy of 1800 GeV. More recently, the Main Injector, to replace the Main Ring and increase the intensity of the primary proton beam, and the Antiproton Recycler, to increase the intensity of the antiproton source, were built.

Several stages progressively raise the beam energy. The accelerating steps of the proton beam at Fermilab include (see Fig. 1.2):

- Cockcroft–Walton electrostatic accelerator;

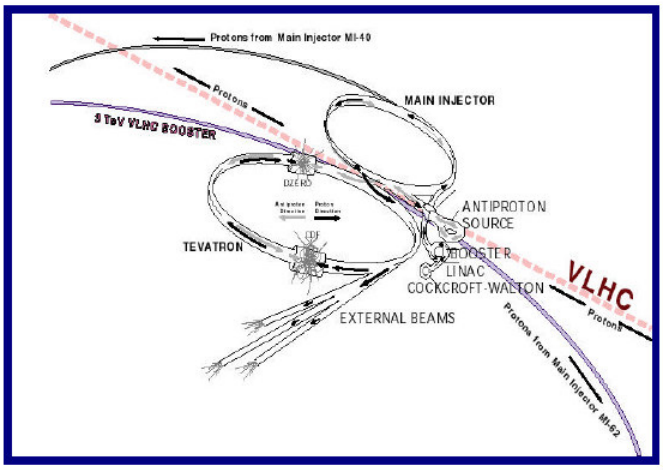

Figure 1.2: Accelerators at Fermilab.

- LINAC;
- Booster;
- Main Injector;
- Tevatron.

For the collider mode of the Tevatron, the Main Injector, beyond being used as injector for the Tevatron itself, also feed an antiproton source. The source comprises an external target where antiprotons are generated, a debuncher ring, where antiproton shots are first collected, debunched and partially cooled, an accumulator ring fed by the debuncher. The Recycler ring is used as an additional antiproton accumulator to store beams of higher intensity. It is made of permanent magnets, and it is located in the same tunnel as the Main Injector.

The Cockcroft–Walton provides the first stage of acceleration. In this device, electrons are added to hydrogen atoms. The resulting negative ions, each consisting of two electrons and one proton, are attracted by a positive voltage and accelerated to energy of 750 KeV.

After leaving the Cockcroft–Walton the negative hydrogen ions enter a linear accelerator called the LINAC. The LINAC consists of five tank containing sets of drift tubes. An oscillating electric field is applied to the tubes. The particles travel through the drift tubes in phase with the electric field, shielded by the tubes when the electric field would slow them down, and

emerging in the gaps In between the tubes when the field is accelerating. In a recent upgrade the LINAC energy was increased to 400 MeV.

After exiting the LINAC, the ions are stripped of their electrons by a carbon foil, resulting in a proton beam that is injected into the Booster synchrotron ring. The Booster accelerates the protons to an energy of 8 GeV, and, via pulsed operation, it organizes the high frequency sequence of LINAC pulsed into a smaller number of bunches for injection into the Main Injector. The Main Injector accelerates alternatively protons and antiprotons, up to 150 GeV for injection in the Tevatron. Alternatively it sends a 120 GeV beam to the antiproton production target.

The final stage of acceleration is provided by the Tevatron, a superconducting synchrotron of 2 Km in diameter, with bending dipole magnets reaching a 4.5T magnetic field. In collider mode, protons and antiprotons are injected separately into the Tevatron and circulate in the same beam pipe. The acceleration in the Tevatron is provided by a set of RF superconducting cavities.

The luminosity in the Tevatron collider is proportional to the beam currents, the antiproton current being critical element.

Collisions of the beam bunches must occur at the center of the particle detectors surrounding the beam pipe at specific location around the Tevatron ring. The two main detectors operating at Tevatron Collider are CDF (Collider Detector at Fermilab) and D0. These detectors discovered the Top Quark in 1995.

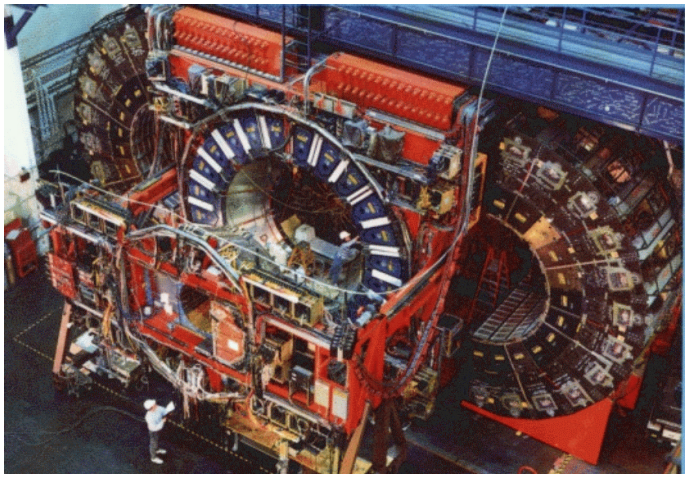

Figure 1.3: CDF in the assembly pit.

The accelerating chain is quite complex since many machines are used in series. All of them have to be synchronized and must work to specifica-

tion in order to obtain the optimum beam configuration for which is also fundamental the field provided by superconducting magnets.

Tevatron magnet ring is based on the FODO (Focusing–drift–defocusingdrift) cell magnet sequence. Magnets with NbTi technology are used, for both superconducting dipole and quadrupole magnets. In the next paragraphs some highlights on superconducting magnets and cables used to build them are presented.

1.4 Superconducting magnets

Keeping the charged particles confined around a circular orbit requires both bending and focusing forces generated by electromagnetic fields. The Lorentz force is given by:

$$\vec{F} = e\left(\vec{E} + v \times \vec{B}\right), \tag{1.1}$$

where:

$\vec{E}$ is the electric field,

e is the electron charge,

$\vec{v}$ is the particle velocity, and

$\vec{B}$ is the magnetic field.

The electric term in equation 1.1 must be used for acceleration, while the magnetic term that does not do work can only be used for bending. At high energy, where $v = c$, a magnetic field of barely 1 T generates the same Lorentz force as an electric field of $3 \times 108\, V/m$. Although they do not increase the particle energy, magnetic field are very effective in bending the trajectory.

The Tevatron magnets are of two different types: dipole and quadrupole magnets. The dipole magnet consists of two poles. Magnetic lines of force emerge from one pole (North) and re–enter the magnet at the other pole (South).

In the space between the poles, where the beam pipe resides, the field is nearly uniform. Magnet builders arrange these dipoles around the circumference of a circle, and have all their field pointing straight up, which is just what is needed to get a beam of protons to circulate around the circle in a clockwise direction. Antiprotons, having negative charges, would circulate around the same magnets counter clockwise. The dipoles are all Fermilab would need were it not for the fact that a beam of protons is a disorderly bunch. They are not all moving in exactly the same direction, but, instead some want to drift sideways while others want to move up or down, away

from the plane of the ring. To keep them in line, we need another type of magnet called a quadrupole, which means a fourpole magnet (two North and two South poles).

The field in this type of magnet is zero at dead center, but grows linearly as you move further away from the center. This means that a well–behaved proton moving along the center, where it's supposed to go, will be left alone by the quadrupole. But an unruly proton, wandering off the beam axis, will be pushed back towards the center. The further away it is the harder it gets pushed. This results in focusing of the beam of protons.

The focusing lattice most frequently used in a circular accelerator is a series of identical cells, each containing focusing (F) and defocusing (D) quadrupole magnets separated by drift (O) spaces (FODO lattice). In between the focusing cells are positioned the dipole bending magnets. This structure is called separated function, to distinguish it from systems with integrated functions, where the bending magnets have radial dependent bending field that is also capable of performing the required focusing. Using magnets with separated functions allows greater design and operation flexibility. The challenging requirements in superconducting magnet design are [2]:

- *Field strength.* The general rule is the higher the field strength, the better. Not only bending, but also focusing and defocusing is more efficient at higher fields;

- *Field quality.* Since the beam has to circulate many times around the same orbit, small imperfections in the field decrease the beam lifetime;

- *Magnet bore size.* The cost of the magnet increases dramatically with the bore size. However, from the point of view of beam acceptance, the larger the bore size, the better it is. At high energy, the beam size can be small but induced fields misalignments and other factors may force to make the acceptance much larger then beam size;

- *AC–DC behavior.* To keep the particle in orbit during acceleration, the magnets have to be ramped. However at maximum beam energy and in collider mode operation, the field must be very stable for many hours;

- *Radiation hardness.* The magnet has to survive in a high radiation area for the entire expected life of the machine;

- *Reliability.* The malfunctioning of a single magnet can cause the loss of the entire beam. With more than one thousand magnets in the ring, this clearly imposes strict reliability requirements on each of them.

- *Cost.* Because of the large number of magnets, both their production and their maintenance cost should be kept as low as possible.

Despite the anticipated strong saving in operating cost, the introduction of superconducting magnets generated other problems like:

- *Persistent eddy currents.* Eddy currents in the superconducting filaments are induced during the magnet current ramp. Because of the vanishing resistance of the material, they do not decay and generate dipolar and higher multipolar fields;
- *Quench behavior.* If one of the critical parameters in the superconductor is exceeded the magnet quenches to the normal resistance state. The machine must be protected from possible damage, and must be able to recover quickly from quenches;
- *Cryogenics.* An accurate study on the cryogenic plant and transport lines is needed in order to avoid high costs for refrigeration.

The key elements of the magnet design are coil cross–section and conductor distribution over it. Given bore size and magnetic field, conductor volume and field quality should be optimized by a careful design of these parameters. For the former, composite wires with very fine filaments, briefly described in the next paragraph, are needed to reduce their magnetization and the associated field error. To reduce the cost, the critical current density should be pushed as high as possible.

1.5 Superconducting strand and cable

In order to wind the coil of a magnet, the multifilamentary strands are bound together in a cable. The multi–strand cable is preferred to a single wire for the following reasons:

- It limits the length requirement for wire manufacturing. A coil wound with a cable having n strands requires piece lengths 1/n shorter with respect to a similar coil wound with a single wire;
- It allows strand to strand current redistribution in the case of localized defects or when a quench originates in one strand;
- It limits the number of turns and facilitates coil winding;
- It limits coil inductance.

The most commonly adopted cable is the so–called Rutherford type, in which the wires are twisted and compressed in two flat layers with trapezoidal shape, as shown in Fig. 1.4 and 1.5.

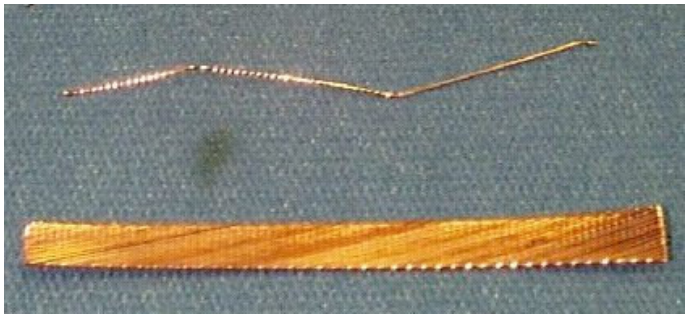

Figure 1.4: Superconducting Rutherford cable and extracted.

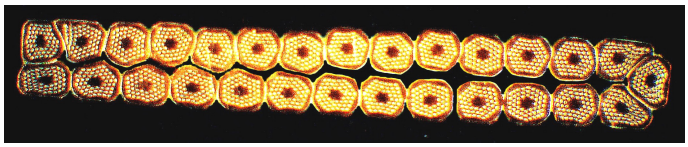

Figure 1.5: Cross section of Rutherford cable.

1.6 The next generation machines

In a few years (possibly in 2008), the LHC proton–proton collider at CERN will operate in the circular tunnel where LEP was in function until the 2001. For a given accelerator energy the two parameters that can be adjusted, the radius of the machine and the field of its magnets, are not independent of each other. The higher the field in the magnets, the smaller is the machine. With a circumference of 27 km and an 8.4 T bending magnetic field, the LHC proton beams will reach a maximum energy of 7 TeV each. Since the LHC collides protons on protons, special "2 in 1" magnets are employed, which accommodate the two separate beams circulating in opposite directions. Being the machine approximately circular, bending radius, bending field, and beam energy are related by the simple relationship:

$$E_{GeV} = 0.3 q B_m r, \tag{1.2}$$

where:

q is the particle charge, in units of electron charge,

B_m is the bending field of the magnets in Tesla,
r is the radius of the circular accelerator in meters.

A fraction of the LHC magnets have been built in the US, and Fermilab is the most important center for the US LHC project. Superconducting $NbTi$ technology was chosen for the LHC magnets, as was done for the Tevatron first and for HERA next, with maximum dipole fields of 4.5 T and 6.2 T respectively. The nominal operating field of LHC is 8.4 T. Because of their higher field, the use of superconducting magnets allows for reduction of tunnelling costs. However as the field increases, better superconductor properties are required, rising costs again. Superconducting $NbTi$ is a ductile alloy, which is ideal for manufacturing composite strands, for making cables out of them, and eventually wind magnet coils. Nevertheless, with an upper critical field of about 11.5 T at 4.2 K, the LHC $NbTi$ coils would have to be pushed near their critical current limits to operate at 8.4 T, requiring a huge amount of conductor. The $NbTi$ performance was enhanced by lowering the magnet operating temperature to 1.9 K (superfluid Helium). At this temperature the $NbTi$ upper critical field rises to 14 T. This choice moved the technological effort more onto the cryogenic system than on the superconducting material R&D.

More cost–effective solutions are presently being studied for a post–LHC Very Large Hadron Collider (VLHC) [3]. At the Snowmass 96 Summer Study on New Directions for High Energy Physics (HEP), a goal was set of a 50 TeV x 50 TeV proton–proton collider with a 3 TeV injector. Fermilab could possibly be the site for the VLHC. In 2001 a detailed Design study for a Staged Very Large Hadron Collider was presented.

A two stage project have been proposed in order to allow the reduction of costs and the possibility to commission the machine in a reasonable time scale while pushing the energy level to the cutting edge limits.

A 233 km long tunnel will initially accommodate low field super–ferric magnets in order to reach an energy of 40 TeV. These magnets will be replaced during the second stage (after the scientific potential of the first stage will be fully realized) by 12T high filed magnets that will allow to reach an energy of 175 TeV with twice the luminosity.

Whereas for the low field magnets $NbTi$ can be used, in the case of the high field option other kinds of superconductors have to be considered. Multifilamentary Nb_3Sn is one of the most promising materials.

High Field Magnet R&D is carried out in very few universities and research centers in the world, between which, one of which is the Fermilab Technical Division.

1.7 Technical Division

The Technical Division develops, designs, fabricates or procures, and tests accelerator and detector components. Not only does the Technical Division personnel build the components of the accelerators and detectors of today and the near feature, but also think far in advance, preparing for high–energy physics machines and experiments of generation to come.

The main projects ongoing projects and R&D programs at the TD are:

- LHC IR low–beta quadrupoles;
- BTeV;
- High Field Magnets/Superconductor R&D;
- International Linear Collider
- Proton Driver

1.7.1 The High Field Magnet Group

The Fermilab Technical Division is a World leader in high–field superconducting magnet development, the bedrock technology for all high–energy particle accelerators. Discoveries in high–energy physics are directly linked to advances in high–field magnet technology. Materials science, the physics of superconductivity, mechanics, electrodynamics and cryogenics all contribute to high–field magnet development.

Chapter 2

Superconductivity

2.1 Introduction

The aim of this chapter is to introduce briefly the basic features of superconductivity. We start with the experimental discovery of superconductivity by K. Onnes and the fundamental experiment of Meissner and Ochsenfeld. The two-fluid thermodynamic theory and the approach of the London brothers are then presented, followed by the rigorous BCS theory, which fully explains the phenomenon. Fundamental parameters like critical magnetic field and temperature, superconducting screening currents, elementary quantized fluxoids, penetration depth and pinning force are dealt with and the Type I and Type II superconductors are described.

2.2 The discovery of superconductivity

The discovery of superconductivity by H.K. Onnes in Leyden was due to research activities in two domains: the liquefaction of gases, leading in 1908 to the liquefaction of helium, and the investigation of electric conductivity of metals at a temperature approaching absolute zero.

According to Mathiessen's rule the total metal resistivity, ρ, is given by sum of two terms: a temperature dependent dynamic resistivity, $\rho_d(T)$, due to the scattering of electrons of thermal origin when subjected to an electric field, and a residual static resistivity, ρ_0 due to the lattice impurities.

Onnes had chosen distilled, purified mercury of very low residual resistivity and expected to find the dynamic component decreasing to zero with the temperature. The result of his experiment is shown in 2.1.

At the critical temperature, $T_{C0} = 4.15\,K$, mercury became superconductive (term given to the phenomenon by Onnes himself). It was established

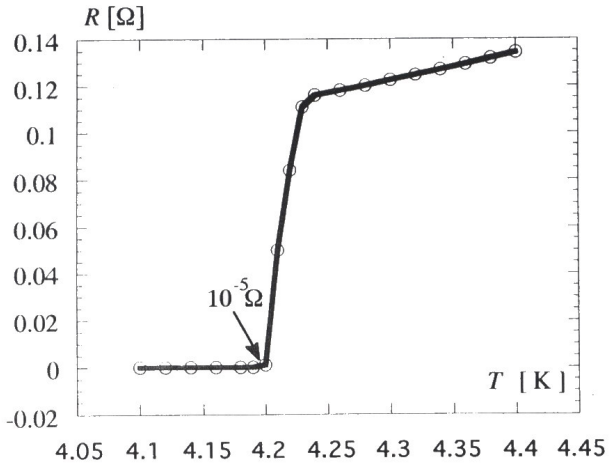

Figure 2.1: The experiment of K. Onnes.

that T_{C0} does not depend upon electric field but on the magnetic field (or induction), H. To any temperature $T < T_{C0}$ there is associated a critical magnetic field $H_C(T)$ that determines a transition or critical magnet field H_{C0} beyond which no superconductive state exists.

$$H_C = H_{C0}\left\{1 - \left(\frac{T}{T_{C0}}\right)^2\right\}. \tag{2.1}$$

This equation was verified in 1933 by the Meissner and Ochsenfeld experiment: a needle-shaped sample of superconductor with a pickup coil were first cooled to $T < T_{C0}$ and next placed in an external parallel field. As long as $H < H_C(T)$ superconductive screening currents (surface current induced in the sample) keep H out of the superconductor (these currents flowing on the material surface generate an induced magnetic field that exactly cancels the applied field in the bulk of superconductor). At $H = H_C(T)$ the magnetic field penetrates the superconductor and a signal appears across the pickup coil.

So far superconductivity could be explained as a limiting case of normal conductivity with zero resistivity:

$$rot\vec{E} = rot\vec{j}\rho = -\frac{\partial}{\partial t}\mu_0 H = 0 \tag{2.2}$$

even if, from a physical point of view, the current must penetrate a certain distance into the metal.

Table 2.1: Superconductors properties

METAL	Nb	Pb	Ta	Hg	Sn	In	Ag
$T_{C0}\,[K]$	9.45	7.2	4.45	4.15	3.72	3.4	1.2
$H_{C0}\,[T]$	0.198	0.0803	0.083	0.0412	0.0309	0.029	0.0078

The experiment was then repeated with an inversion of the two operations: the sample was first exposed to the external field and then cooled to T¡ TC (H); they did not expect any signal when crossing TC because the field remained unchanged, but surprisingly a signal appeared corresponding to the total expulsion of magnetic flux in the sample.

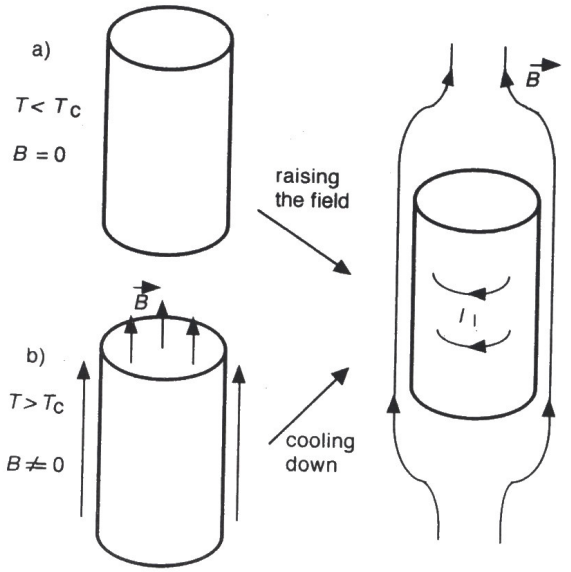

Figure 2.2: Explaination of the Meissner-Ochsenfeld effect by the behaviour of a lead cylinder in a magnetic field.

Materials exhibiting this effect are called Type I superconductor. In Table 2.1 are shown T_{C0} and H_{C0} values for pure metal, Type I superconductors.

At this point the superconductivity could not be explained by extending the metallic conduction theory to $\rho_d = 0$, and other ways had to be investigated.

2.3 Two-fluid thermodynamic theory

The transition from the perfectly diamagnetic superconducting phase to the non-magnetic normal phase is a reversible transition in the thermodynamic sense as shown by experiments. Thermodynamic arguments can therefore be applied to a superconductor.

In 1934 Goter and Kasimir developed a thermodynamic, two-fluid model of normal and superconductive electrons, which contributed to a better understanding of superconductivity. In analogy with the gaseous, liquid and solid phases of atoms and molecules, depending on pressure and temperature, the H (T) curve was interpreted as a borderline between two systems: the inner, condensed, superconductive one, where the dc current is transported without resistance, and the outer, normal conducting region, of resistive electron conduction. The twophase variables are T and H; along the separation line normal conductance and superconductivity coexist in the sample.

Applying the two-fluid theory to phase transitions in superconductors, the following experiment was performed: at constant $T < TC0$ a needle-shaped superconductive sample of volume V $[m3]$ was placed into a collinear external magnetic field H with a sizeable gradient $-\frac{\partial H}{\partial x}$. Due to the interaction between the screening current Il and the field gradient the sample is submitted to a repulsive force

$$f = -\mu_0 V I_t \frac{\partial H}{\partial x} - \tag{2.3}$$

To reach the critical field HC the sample must be pushed backwards; the equivalent mechanical work is:

$$W = \int f\, dx = \int_0^{H_C} \mu_0 V H\, dH = \mu_0 V \frac{H_c^2}{2}. \tag{2.4}$$

If U is the inner energy and S the entropy of the system, the difference between free energies (defined as $F = U - TS$) of two states is:

$$dF = dU - TdS - SdT. \tag{2.5}$$

For an isothermal process with constant temperature, $dT = 0$, the differential heat (defined as $Q = TS$) between the two states could be written as $dQ = TdS$ and the equation becomes:

$$dF = dU - dQ. \tag{2.6}$$

The inner energy of a system is $U = Q + W$, so we can write:

$$dF = dW \rightarrow F_{SC}(T,H) - F_{SC}(T,0) = \mu_0 V \frac{H_C^2}{2}. \tag{2.7}$$

Due to $T = cost$, $dF = dW = W$.

At $H = H_C$ the sample goes normal and due to the reversibility of the process no additional work is required:

$$F_{SC}(T,H_C) - F_{SC}(T,0) = \mu_0 V \frac{H_C^2}{2} = F_{NC}(T,0) \tag{2.8}$$

SC = superconductive conducting state; NC = normal conducting state.

From which:

$$F_{NC}(T,0) - F_{SC}(T,0) = \mu_0 V \frac{[H_C(T)]^2}{2}. \tag{2.9}$$

In 0 field the superconductive phase has a lower free energy (the term on the right side is positive) and is therefore thermodynamically stable (the stable state is that with the lowest free energy). By rising H to H_C the screening current effect raises the free energy in the superconductor until it becomes normally conductive. At H constant

$$S = -\frac{\partial F}{\partial T} \tag{2.10}$$

and for the electron contribution to the specific heat

$$C_e = T\frac{dS}{dT} \tag{2.11}$$

For $H = 0$ one obtains:

$$S_{NC} - S_{SC} = -\mu_0 V H_C \frac{\partial}{\partial T} H_C(T), \tag{2.12}$$

and for the difference of the two corresponding specific heats:

$$C_{e,NC} - C_{e,SC} = -\mu_0 V T \frac{\partial}{\partial T} \left\{ H_C \partial\partial T H_C(T) \right\}. \tag{2.13}$$

Both curves have zero slope at $T = 0$, which is not the case for conduction electrons, treated as a Fermi gas; their entropy S_{NC} and specific heat $C_{e,NC}$ rise linearly with temperature while the equations found suggest an exponential rise in the range $0 < T < T_{C0}$, as verified by experiment. The condensation effect in a superconductor is thus a gradual process like freezing of water: at T_{C0} the first superconducting charge carrier of the new fluid appears; in the interval $0 < T < T_{C0}$ normal conducting electrons are transformed into superconducting ones.

2.4 Skin effect in superconductors

The requirement for a finite current penetration depth and the field expulsion demonstrated by the MO effect were explained by the skin effect theory initiated by Becker, Heller and Sauter in 1933 and developed by the London brothers in 1935.

BHS suggested that in the absence of resistance an applied electric field would accelerate electrons steadily according to the formula:

$$\frac{\delta}{\delta t} m_e \vec{c} = e\vec{E}. \tag{2.14}$$

For n electrons per unit volume, the current density j is given by $\vec{j} = ne\vec{v}$, so we have:

$$\frac{\delta}{\delta t}(ne\vec{v}) = \frac{\delta}{\delta t}\vec{j}. \tag{2.15}$$

Eliminating v, the velocity between the equations 2.14 and 2.15, we obtain:

$$\vec{E} = \frac{m_e}{ne^2}\frac{\partial}{\partial t}\vec{j}, \tag{2.16}$$

it is convenient to write:

$$\Lambda = \sqrt{\frac{m_e c^2}{4\pi n e^2}}, \tag{2.17}$$

so that becomes the first London equation,

$$\vec{E} = \frac{4\pi\Lambda^2}{c^2}\frac{\partial}{\partial t}\vec{j}, \tag{2.18}$$

which is the equivalent of Ohm's law in a normal conductor. Taking the curl of both sides and replacing in the first Maxwell equation $\vec{\nabla}\vec{E} = -\frac{\vec{B}}{c}$, $B = H$, we obtain:

$$\frac{\partial}{\partial t}\vec{H} = -\frac{4\pi\Lambda^2}{c}\vec{\nabla}\left\{\frac{\partial}{\partial t}\vec{j}\right\} \tag{2.19}$$

The Londons's equations suggest that the time dependence can be dropped, to obtain

$$\vec{H} = -\frac{4\pi\Lambda^2}{c}\vec{\nabla}\vec{j}. \tag{2.20}$$

This is the second London equation, which describes the condition in the penetration layer. If 2.20 is combined with Maxwell's second equation, this yields

$$\vec{\nabla}^2 H = \frac{H}{\Lambda}. \tag{2.21}$$

The solution of 2.21 for the simple case of a plane interface between superconducting material and vacuum gives the expression:

$$H(x) = H(0) exp\left(-\frac{x}{\Lambda}\right), \tag{2.22}$$

where x is the distance into the superconductor. A similar equation holds for the current density in the penetration layer. Both field and current density fall off exponentially into the interior of superconductor and the penetration depth, Λ, is the distance at which both H and j drop to $1/e$ of their surface value.

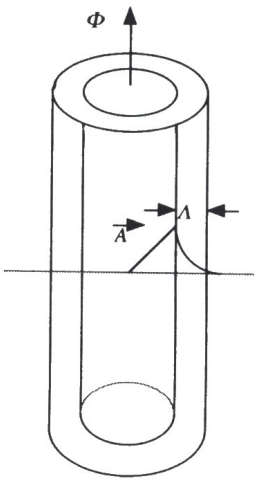

Figure 2.3: The penetration layer.

This solution is also in agreement with the experiment since no internal field is admitted. The penetration depth of the superconductive current is $\Lambda >> 10^{-7} m$.

2.5 Cooper pairs

In 1957, Bardeen, Cooper and Shrieffer constructed a theory of superconductivity based on the interaction of electrons with the lattice vibration or phonons of a solid.

Below T_C weak attractive interaction causes some of the conduction electrons to form Cooper pairs, a paired status with equal and opposite momentum at 0 super current. When a current is applied to the superconductor, all the pairs have the same momentum directed parallel to the electrical field. Due to this coherent motion the pairs do not collide with the lattice and there is no resistance.

When the first electron moves through the metal lattice, it attracts positive ions, but because of its inertia, the response of the lattice is not immediate. The shortest response time corresponds to the highest frequency, ω_d. The maximum lattice deformation lags behind the electron by a distance, d:

$$d \approx v_f \frac{2\pi}{\omega_d} \approx 100 \div 1000\, nm \tag{2.23}$$

Where v_f is the Fermi velocity which is on the order of $10^6\, m/s$. The second electron is attracted by the positive ion accumulation in the lattice deformation and the strongest effect is achieved when the two electrons follow adjacent tracks in the lattice and their distance is equal to d. This explains why a Cooper pair is a very extended object. As a consequence, Cooper pairs overlap each other, so that in the space occupied by a Cooper pair there is millions of others. This is very important for the BCS theory because the Cooper pairs must change their partners frequently in order to provide continuous binding. The binding energy is very small, between 10^{-4} and $10^{-3}\, eV$, so that the pairs can only exist at low temperatures where this energies not overcome by thermal agitation. Because of their space extension, Cooper pairs differ from other Bosons. They only exist at BCS ground state and there is no excited state. An excitation is equivalent to breaking them up to single electrons.

The BCS ground state is characterised by a macroscopic wave energy that is separated from the energy levels of the unpaired electrons by an energy gap of 2Δ. This gap is temperature dependent and at $T = 0$ it can be related to the critical temperature:

$$\Delta(0) = 1.76 \beta T_c \tag{2.24}$$

where β is the Bolzmann constant. Both Δ and T_C are proportional to the Debye frequency which in turn is inversely proportional to the square root of the atomic mass, M.

2.6 Flux Quantization

Extending the present knowledge to a thin superconductive cylindrical tube exposed to a coaxial magnetic induction B, and cooling to $T_c(B)$ and below, a magnetic flux Φ will be trapped inside the hole.

Two circumferential superconductive currents will flow within the penetration depth on the inner and outer tube surface excluding the magnetic induction from the bulk of the wall. When external induction is removed only the outer screening current will disappear, while the inner one will continue to flow and shield the trapped flux Φ. F. London postulated in 1950 that this flux must be quantized:

$$\Phi = m\Phi_0 \tag{2.25}$$

with the elementary fluxoid equal to

$$\Phi_0 = \frac{h}{q_s} = \frac{h}{2e} = 2 \cdot 10^{-15} Vs \tag{2.26}$$

where h is the plank constant.

This relation was confirmed by the BCS theory and in 1961 by experiments using thin lead and thin tubes.

2.7 Type II supercondouctors

So far we have considered Type I superconductors: their critical magnetic induction B_{C0} is low, 1.5-2 T, and by measuring the magnetic flux difference between a normal and conductive state one obtains the curves shown in Fig. 2.4.

Type II superconductors are characterized by two critical fields, called B_{C1} (1–10 mT) and $BC2$ (10–100 mT). They show complete field exclusion below the lower critical field; when the field is increased to the upper critical field the sample remains superconductive.

The surfaces s_1 and s_2 in Fig. 2.4 are equal, this means that the work required to bring the Type II superconductor sample into the field $Hc2$ is the same as the work to bring the Type I sample to its H_c.

This behaviour is explained by the breaking up of the sample into normal and superconductive zones. The flux is concentrated in tubular isles, each carrying an elementary fluxoid Φ_0. The magnetic field lines are surrounded by super current vortex. The Cooper pair density drops to zero at the centre of the vortex, so the core of each flux tube is normal conducting.

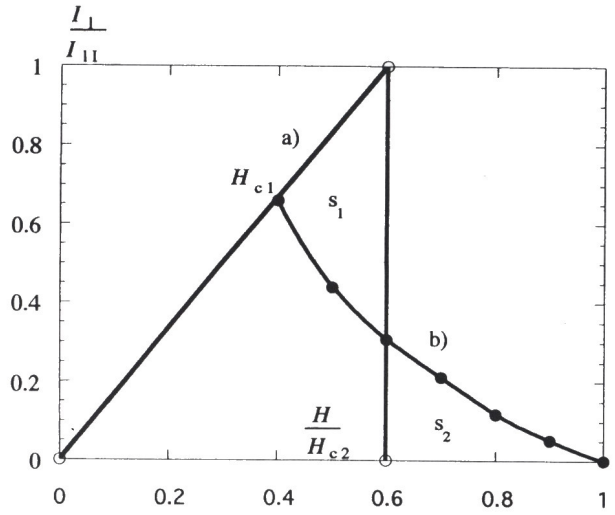

Figure 2.4: $I_1/I_{1I} = f(H/H_C)$ diagrams for (a) Type I and (b) Type II superconductors.

If we compute the mechanical work experienced by a needle sample of cross–section s in a collinear external field H with a gradient $-\frac{\partial H}{\partial x}$, the resulting force acting on a flux tube model of length l, cross section a, and a line current I, is:

$$f = f_t + f_s = l[\mu_0 sH - \Phi_0]\frac{\partial H}{\partial x} \tag{2.27}$$

and the work to bring a sample with one flux tube into the field H is:

$$W = W_s - \Delta W = l\left(s\mu_0\frac{H^2}{2} - \Phi_0 H\right). \tag{2.28}$$

Introducing ξ for the radius of the normal conducting hole one obtains from 2.28 and 2.9 that the energy loss due to one flux tube is compensated by the gain due to the fluxoid contribution:

$$\Delta W = \xi^2\pi l\frac{\mu_0 H_c^2}{2} = lH_{C1}\Phi_0. \tag{2.29}$$

For large enough ξ, H_{C1}, a quadratic function of ξ will exceed H_C and the superconductive state will be destroyed before a single fluxoid is formed: we have a Type II superconductor. At $H = HC1$ the fluxoid magnetic diameter is assumed to be 2Δ such that:

$$\Phi_0 = \mu_0\lambda^2\pi H_{Cl}, \tag{2.30}$$

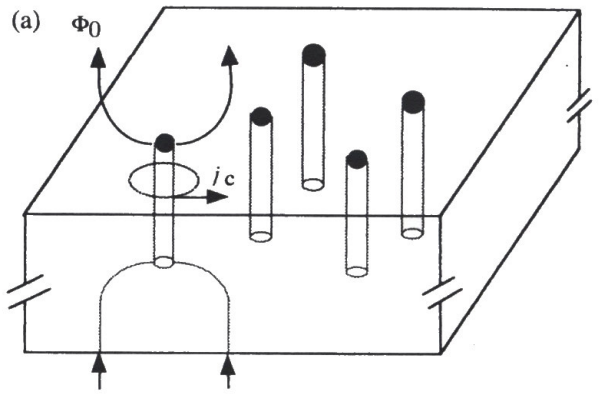

Figure 2.5: Elementary fluxoid *Phi* located in the normal zone of a soft Type II superconductor.

$$H_{C1}\frac{\xi}{\sqrt{2\Lambda}}H_C \tag{2.31}$$

Equation 2.31 states that for $\xi \leq \sqrt{2\Lambda}$ the superconductor is of Type I and for $\xi \geq \sqrt{2\Lambda}$ of Type II. The upper critical field can be calculated in a similar way by assuming that all the normal conducting cores of the flux-tube are in contact (at this point superconductivity breaks down):

$$\Phi_0 = \xi^2 \pi \mu_0 H_{C2} \tag{2.32}$$

$$H_{C2} = \frac{1}{\sqrt{2}}\frac{\Lambda}{\xi}H_c \tag{2.33}$$

$$H_{C1} \cdot H_{C2} = H_c^2. \tag{2.34}$$

In order to have Φ_0 through the specimen, the density of the Cooper electron pairs, concentrated within the small coherence length ξ, will decrease just near the flux–line axis. A. Abrikosov proposed this model in 1957.

But in a symmetric fluxoid mesh (as show in fig. 2.5) the superconductive vortices and their repulsive forces cancel out except in the outermost circumferential layer. Furthermore, if one tries to convey an increasing so called transport current I_1 through the conductor, the accompanying circular magnet field H_t would start pushing the flux-tubes inwards at $H_t > H_{C1}$, destroying the outer ones. A non-uniform fluxoid pattern is thus needed for

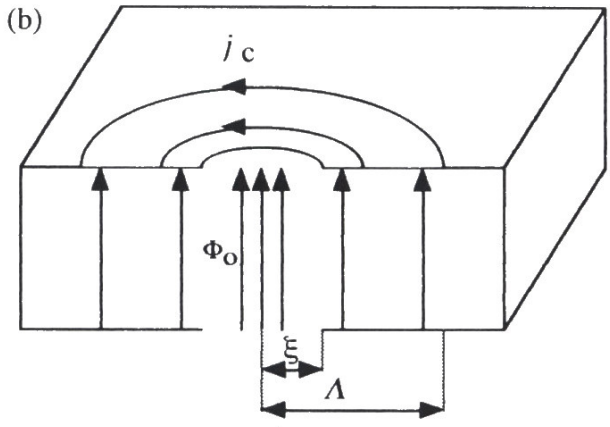

Figure 2.6: Penetration depth Δ and coherence length ξ in a Type II superconductor.

Table 2.2: Superconductors properties

SC	NbTi	Nb3Sn	Nb3Al	Nb3(AlGe)
$T_{C0}\,[K]$	9	18.2	19.1	19.3
$H_{C0}\,[T]$	14-15	24-30	36-41	43.5

a finite j_S; due to the spatial gradient $\frac{\partial H}{\partial s}$ the net repulsive force between fluxoids is then:

$$f_s = \vec{H}\mu_0 \frac{dH}{dS} = \mu_0 \left[\vec{H}x \cdot rot\vec{H}\right] = \vec{B}xj_S, \tag{2.35}$$

which is also the Lorenz force due to the macroscopic current density j_S, that causes fluxoids to move perpendicularly to the current and to the field. Fortunately in hard Type II superconductor artificial defects (pinning centres) of the elementary fluxoid size are built into the crystal lattice giving rise to a pinning force f_p , opposed to the Lorenz force and preventing movements of the fluxoids. A typical pinning force can be defined at j_{SC} and B:

$$\vec{f}_{PC} = \vec{B} \times \vec{j}_{SC}, \tag{2.36}$$

where by $j_{SC} = f(B)$ at $j = j_{SC}$ flux-tubes begin to move, a resistive component appears, and the superconductor goes normal. In Table 2.2 are shown T_{C0} and H_{C2} values for same hard Type II superconductors.

2.8 Magnetization of hard superconductors

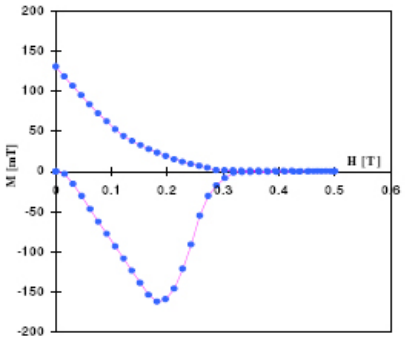

Figure 2.7: Nb hysteresis curve.

Hard superconductors exhibit a strong magnetic hysteresis. While an ideal Type II superconductor without any flux pinning should show a completely reversible response to an internal magnetic field, a hard superconductor is only reversible in the Meissner phase because then no magnetic field enters the bulk, so no pinning can happen.

Above H_{C1} magnetic flux enters the sample and is captured at pinning centers. When the field is reduced again these flux lines remain bound and the specimen keeps a frozen-in magnetization even for vanishing external field. The field polarity has to be inverted to achieve $M = 0$, but the initial state can only be recovered by warming up the speciem to destroy superconductivity and release all pinned flux quanta. A typical hysteresis curve is shown in Fig. 2.7 for Nb alloy.

2.9 Critical state model

One can now describe hard Type II superconductors by the model of Bean and Kim (1962, 1964), so called *Critical state model*. Two cases are distinguished:

1. The superconductor is placed in an external magnetic field H but carries no transport current I_t; equal and opposite screening currents (persistent current) of density $\pm j_C$ flow in the plane orthogonal to H_e.

2. The superconductor is exposed to H_e and carries a transport current I_t. Superimposed screening and transport currents $\pm I_C$ and I_t will flow

simultaneously, where their respective orientation will depend upon the location of the superconductor in H_e.

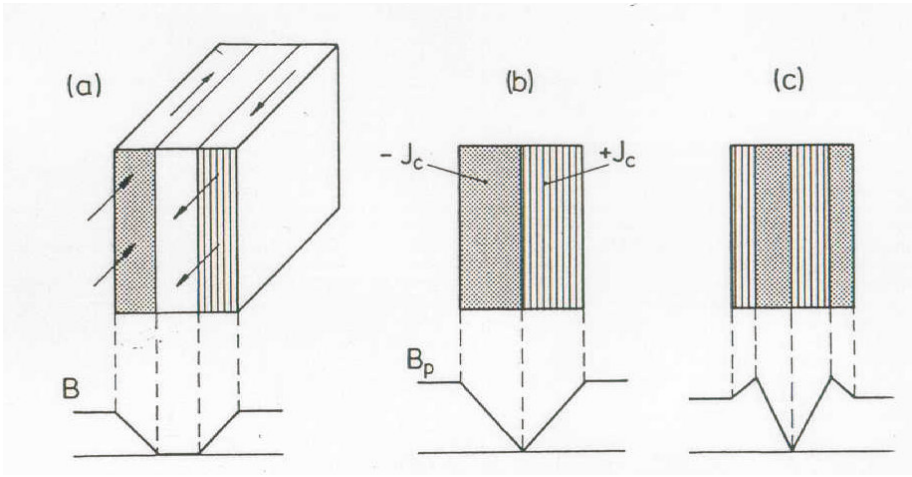

Figure 2.8: Current and field distributions in a slab of a hard superconductor according to the critical state model.

We have a cylinder of superconductor with a changing field parallel to its broad face. When raising the field H around a superconductor a bipolar current of critical density $\pm j_{SC}$ will flow in the penetration zone to cancel the applied field in the central region. In the region of current flow the magnetic field B is linear, as shown in Fig. 2.8 case a). As j_{SC} is inversely proportional to H or B as demonstrated by Anderson:

$$j_{SC} = \frac{j_0 B_0}{B + B_0} \tag{2.37}$$

when increasing the external field these super currents will soon occupy the entire cross-section and the magnetic field B will have fully penetrated the superconductor, see Fig 2.8 case b). The associated field is called the penetrating field H_P. Rising H beyond H_P leads to a non–vanishing field at the center, but eventually the current density will drop because it depends on magnetic field (at $H = H_{C2}$, $j_{SC} = 0$, and the superconductor will go normal).

When H is lowered again, a new bipolar current of opposite polarity is induced and the current–field pattern inside the slab assumes the complicated shape sketched in Fig. 2.8 case c). It is straightforward to derive a hysteresis curve from this model, (Fig. 2.9).

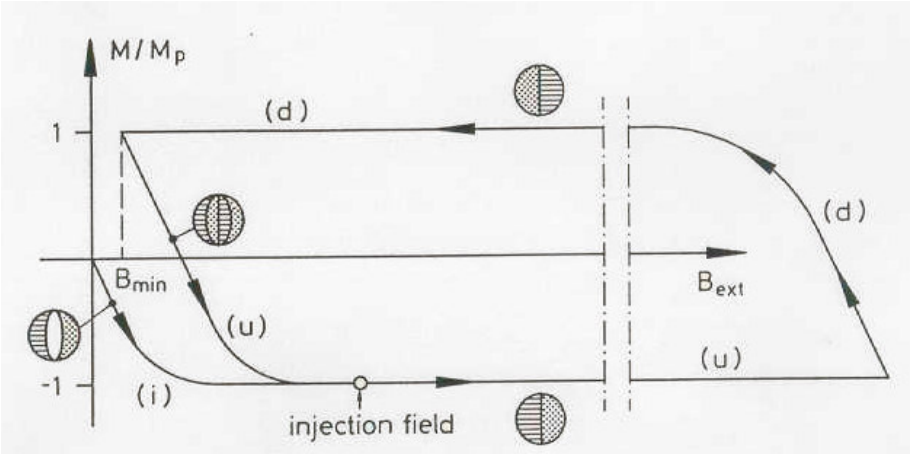

Figure 2.9: The normalized magnetization M/Mp as a function of the external field. (i): initial curve, (u): up–ramp branch, (d): down ramp–branch.

Chapter 3

Superconducting strands and their manufacture

3.1 Introduction

Following the discovery of high–field superconductivity in the 1950, superconducting wires for magnet construction were produced in industry and offered for sale within a remarkably short space of time. By 1961 small magnets were being made from 1/4 mm diameter wires of niobium zirconium, a ductile alloy. This was quickly followed by niobium tin, an intermetallic compound with excellent superconducting properties but so brittle that it could not be fabricated by conventional wire–drawing processes. It was initially produced for sale in the form of a vapour–deposited layer on a very thin stainless steel tape. Niobium titanium wires were first manufactured in 1965 and this ductile alloy has since become the standard "'work horse"' of superconducting magnet construction, mainly because it is relatively easy to fabricate and can be co–processed with copper.

In this chapter we describe the fabrication of the two common technological superconductors NbTi and Nb3Sn. In particular the Nb3Sn superconducting wires that we have tested are made with the Modified Jelly Roll process (MJR), the Powder–in–Tube process (PIT), and the Restacked Rod Process (RRP), which are described in the following.

3.2 Superconductors for use in magnets

An important issue for the development of new superconducting materials is to reach higher operating temperatures in order to reduce the cost of the cooling system. However, at present only low temperature superconductors

(LTS), operating at boiling helium temperature, are used to design and produce magnets, because the main demand on high current densities limits the choice of the material to be used. The new high temperature superconductors (HTS) still do not reach very high current densities and are difficult to produce in the form of long thin wires [4].

The same request excludes using type I superconductors, where in the Meissner state current can flow only in a small part of the strand cross–section (delimited by the λ length) near the boundaries. Furthermore, these materials show a very low critical field, which limits applications. Hard type II superconductors are the only materials usable to manufacture magnets.

Over the last thirtyy years, niobium titanium alloys have undergone extensive development. Niobium titanium alloys are ductile and can be co–processed with copper into a wide range of composite conductors. NbTi is currently the most commonly used material in magnet industry, but its properties are adequate only up to fields of 8–9 T [5]. MRI solenoids and superconducting accelerators, starting from the Tevatron, HERA, and more recently LHC have relied on NbTi. In addition, the Superconducting Super Collider (SSC), a U.S. project that was first approved and later cancelled, planned to use NbTi. Significant advances in performance as well as conductor cost reduction resulted from the SSC R&D.

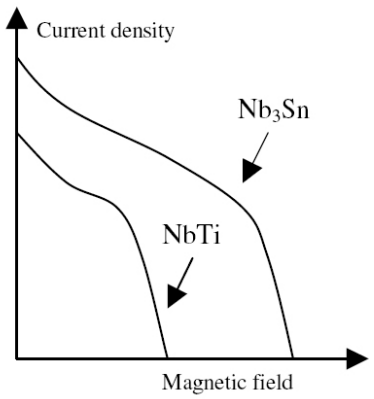

Figure 3.1: Critical current densities of $NbTi$ and Nb_3Sn at a constant temperature (4.2 K).

For optimum performance, the critical parameters J_c, B_c, and T_c, should be as large as possible. In general, it turns out that critical field and temperature are determined by the chemistry of the material, like the composition, whereas the critical current density is determined by the microstructure.

Therefore, the J_c of niobium titanium has increased as the processing

techniques improved, whereas the critical field and temperature have remained more or less constant.

Fig. 3.1 shows the available operating area for a superconducting magnet using $NbTi$ strands and Nb_3Sn strands. Nb_3Sn, which is an intermetallic compound with the A15 crystal structure, has an advantage over $NbTi$, both in terms of critical current density and critical field. In addition the critical temperature is appreciably higher for Nb_3Sn (18.3K) than for $NbTi$ (9.3K). Despite these substantial advantages Nb3Sn has been used so far only on a fairly modest scale in comparison with $NbTi$. The reason for this lies entirely in the mechanical properties of Nb_3Sn. Unlike $NbTi$, which is a ductile alloy, Nb_3Sn is a brittle intermetallic compound which critical current is extremely sensitive to tensile strains.

However, only A15 (Nb_3Sn and Nb_3Al) and HTS ($Bi-2223$, $Bi-2212$, and $YBCO$) materials could in principle be used above 10 T. As mentioned, HTS's are not competitive yet. On short–term magnet production, Nb_3Sn appears to be the right choice, while Nb_3Al is the most promising on the medium term, showing less strain sensitivity.

3.2.1 Filamentary composites

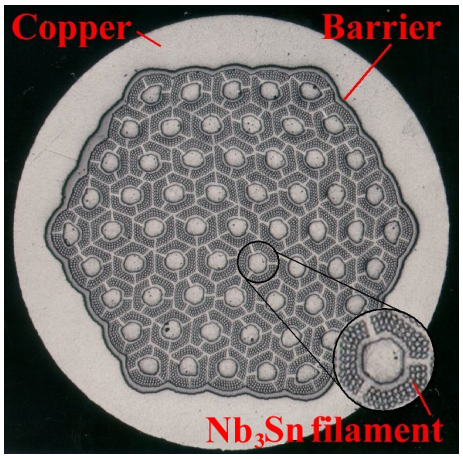

Figure 3.2: Nb_3Sn multifilamentary strand.

The conductor used in magnet industry is not pure superconducting material. Thin filaments of $NbTi$ or Nb_3Sn are embedded in a copper matrix to form a multifilamentary strand. The need of implementing copper in the strand design is due to limit instability phenomena [6]. The filaments have to be limited in size for two reasons, one of which is flux jumping [6].

The second reason to require small filaments is to limit persistent magnetization currents in the superconductor [7], which are the sources of severe field distortions at low excitation of an accelerator magnet. These bipolar currents generate all the multipoles allowed by the coil symmetry. A distinct hysteresis behavior is also observed. Actually the restriction on filament diameter is more constraining for magnetization than for flux jumping. For $NbTi$, filament diameters of 5–6 mm are needed for relative deviations from ideal dipoles or quadrupoles on the order of 10^{-4} [7].

The filaments in a strand are also twisted with a pitch of 15–25 mm (more tightly than needed for stability against flux jumping) to suppress inter filament eddy currents induced during a field sweep across the matrix. Fig. 3.2 shows a typical cross section for an Intermagnetics General Corp. (IGC) intermediate tin Nb_3Sn strand with 61 split–subelements before thermal reaction. The non–copper region containing the split–subelements is separated from the outer copper matrix by means of a tantalum barrier. Each subelement contains 106 Nb filaments

3.3 Niobium Titanium

Niobium and titanium are mutually soluble to form ductile alloys over a wide range of compositions. The critical properties vary with composition. Since optimum critical field and highest critical temperature do not occur at the same composition, commercial alloys are usually formulated for optimum critical field, in the range of Nb from 46.5 to 50 wt% Ti. Otherwise a compromise must be found depending on the technological application of the strand. A ternary element, most commonly tantalum, may also be added to produce a modest increase in B_{c2} of 0.3 T at 4.2 K and 1.3 T at 1.8 K.

Originally it was thought that the principal source of flux pinning in the material came from the dislocation cell structure in the wire. It has now become clear that most of the pinning is provided by finely divided deposits of Ti α–phase. This is a hexagonal close packed titanium rich phase, which is precipitated on the dislocation cell boundaries as a result of the heat treatments applied during the manufacturing process. The α–phase remains normally resistive at low temperature and has been shown to be a significant source of flux pinning sites.

Artificial pinning center (APC) techniques have been attempted in order to increase the field operating range and critical current. These techniques are based on the fine dispersion of second phase particles by mechanical processing. So far they have only allowed achieving higher critical currents at low fields.

The request for higher field magnets has led to $NbTi$ being used at temperatures lower than 4.2 K. This is the case of the Large Hadron Collider (LHC) at CERN. The magnets for this accelerator will work in superfluid helium (1.9K), where Bc2 is increased from its 4.2 K value of 11 T to 14 T. The use of superfluid helium brings many other benefits in terms of better cooling and stability.

The manufacturing technology has been developed by different firms. Currently, the production of high Jc wires with filaments below 10 mm embedded in a high purity OFHC (Oxygen Free High Conductivity) copper matrix is normal practice. A scheme is shown in Fig. 3.3.

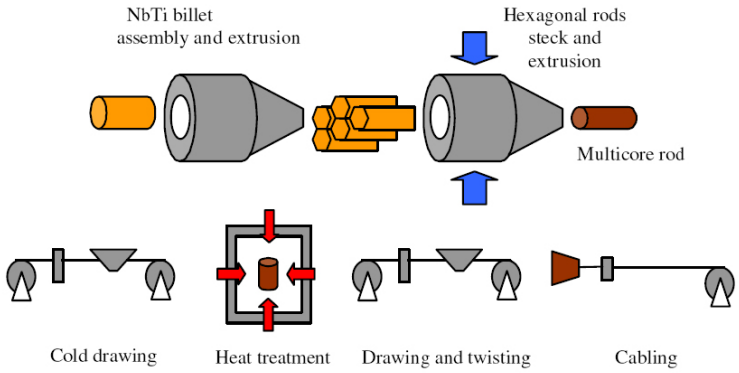

Figure 3.3: Production process of $NbTi$ strands and cables.

The first step of the process is to build a billet of high homogeneity $NbTi$ alloy by arc vacuum melting. The $NbTi$ is then fitted inside a copper extrusion can with a thin diffusion barrier of pure Nb interposed between the $NbTi$ and the copper. The purpose of this barrier is to prevent the formation of $CuTi_2$ intermetallics during intermediate heat treatments, since they are hard and brittle, and break the filaments at the last stages of drawing. The billet is evacuated, electron–beam welded, and extruded. After cold drawing to size, the rod is drawn through a hexagonal die and then cut into many lengths. These lengths are stacked into another copper can, which is again sealed, extruded and drawn down to final size. For accelerator magnets, which may have up to 104 filaments, a double stack process is often used in which the rods are again drawn into hexagonal sections and stacked in another can. Multiple heat treatments are applied throughout the process in a defined sequence of alternating cold work and heat treatment, which has been found to produce the best configuration of α Ti precipitates and hence the best flux pinning. After reaching final size, the wire is twisted.

Table 3.1: $NbTi$ properties for LHC.

	IGC $NbTi$
Wire diameter [mm]	1.29
Filament diameter [μm]	5
Cu to non–Cu ratio	1.8
I_c at 8 T and 4.2 K [A/mm^2]	1114

Typical properties of NbTi strand produced for LHC dipoles are listed in Table 3.1.

3.4 Niobium Tin

Nb_3Sn is an intermetallic compound having a well–defined stoichiometry and the A15 crystal structure. It shows higher critical temperature and field than $NbTi$, but is highly brittle, as previously mentioned, and its critical current is extremely strain sensitive. Originally, Nb_3Sn was produced in the form of tape by heating Nb tapes in a liquid Tin bath at temperatures above 930^{o}C. However tapes are not a useful shape for magnet design, and new processing techniques had to be developed. The basic elements Nb, Sn, and Cu are manufactured in the form of a round composite strand. At this stage, the strand is still ductile and can be used to produce cables.

The A15 compound is formed at the interface of Nb and the $Cu - Sn$ matrix by heat treating such composites at temperatures of about 700^{o}C. The Cu matrix is necessary to shorten the heat treatment time, since Cu works as a catalytic agent for the preferential growth of Nb_3Sn phase at the expense of other non superconducting $Nb - Sn$ phases. Prior to heat treating the strand at high temperature to form the Nb_3Sn compound, heat treatments at lower temperature are necessary to homogenize the $Cu - Sn$ matrix.

The dominant source of flux pinning in Nb_3Sn appears to be the grain boundaries [8]. In order to obtain high critical current densities it is therefore necessary to produce a fine–grained structure. This is in conflict with the long time necessary to obtain a consistent volume of superconductor. The optimum process is obtained by balancing these two issues and taking into account the material specific application.

The critical current density J_c, needs to be carefully defined. In $NbTi$ one normally quotes the critical current density in the superconductor, $J_{c,NbTi}$,

and the critical current density on the whole strand cross section, $Jcav$. These two current densities are related to each other as follows:

$$J_{cav} = \lambda J_{c,NbTi}, \tag{3.1}$$

where λ is the copper to superconductor ratio. For Nb_3Sn the distinction is complicated by the presence of the bronze between the filaments, generated from the diffusion of tin into the copper. Usually the critical current density is calculated in the non-copper part of the strand, which is comprehensive of both superconductor and bronze, while the overall average value, J_cav, is still calculated on the whole strand cross section.

Different manufacturing processes have been tested and developed in the last years by different companies. The most important ones are:

- Bronze process;
- Internal tin process (IT);
- Modified jelly roll process (MJR);
- Restacked Rod Process (RRP);
- Powder in tube process (PIT);

Heat treatments are determined and suggested by the manufacturing companies for each type of strand. In principle, this is done by trying various heat treatment schedules, testing the resulting properties of the strand, and choosing the thermal cycle that achieves the best strand performance.

3.4.1 The bronze process

The bronze process, although almost twenty years old, is still that used most frequently for large production of Nb3Sn where reproducibility and reliability are essential and cost of little significance [9].

The bronze process is very similar to the fabrication of $NbTi$ wires. A rod of pure ductile Nb or Nb containing a small amount of Ta or Ti is assembled in a bronze matrix, extruded, and drawn to the final size. The tin content in the bronze matrix being limited to less than 13.5wt% (limit for a ductile bronze alloy), a large bronze matrix is required to provide sufficient tin to the niobium rods. The initial billet is made of hundreds of Nb rods and it is drawn into a hexagonal shaped element of intermediate size. The hexagonal rods are cut and reassembled in a second billet, which is extruded, annealed and drawn to the final wire size. Nb_3Sn wires are stabilized against

flux jumping using OFHC copper. The copper has to be protected from the diffusion of the bronze-tin by a tantalum or niobium barrier. The niobium barrier is cheaper, but at low fields it is superconducting [9]. This can cause field distortions, which can become intolerable in applications like particle accelerator magnets. In these cases a Tantalum barrier is preferred. The stabilizing copper can be incorporated internally with up to 27% of the wire cross section or externally with a copper part of 30-60%.

The bronze process requires frequent annealing steps because bronze work hardens rapidly. If precautions are not taken, these multiple anneals result in prereaction between the Sn in the bronze and the Nb, with formation of Nb_3Sn during fabrication [9].

3.4.2 The internal tin process

The Internal Tin (IT) process was introduced to overcome the main limit of the bronze method, which is a limited tin content of 13.5wt% in the matrix. A higher concentration of tin produces higher critical current densities in the Nb_3Sn layer [10].

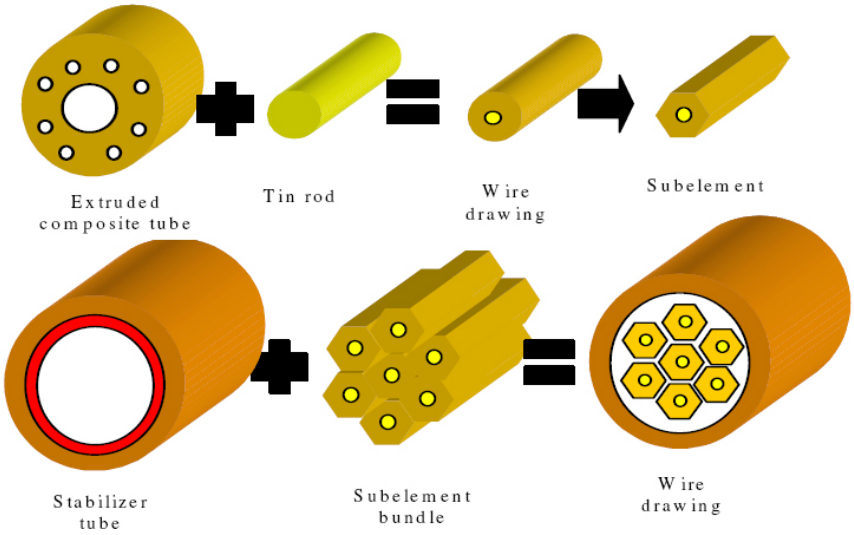

Figure 3.4: Internal Tin Process.

The idea was to distribute local tin sources surrounded by Nb rods and located in a copper tube. The composite Cu tube containing several Nb rods around a central hole is first hot extruded, then filled with Sn and drawn into hexagonal subelements, which are shortened and reassembled into a new billet characterized by a stabilizing copper outer ring protected by a tantalum

barrier. The billet is then drawn to the final wire size without intermediate annealing. Since this process does not involve intermediate anneals during wire fabrication, the billets are free from prereaction problems.

Factors like the amount of Nb, the amount of Sn, the filament size and the subelement number characterize the conductor properties [11].

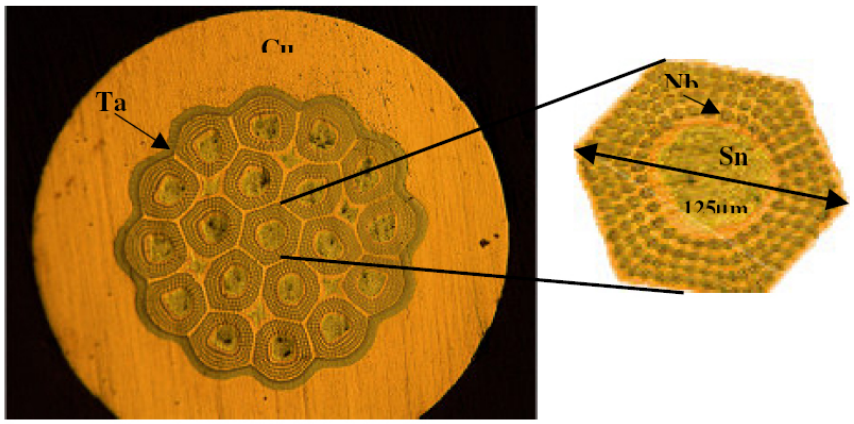

Figure 3.5: Internal Tin (IT) by Intermagnetic General Corporation (IGC).

This method suffers from "'bridging"' problems [9]. Since the Nb filaments around the Sn rod within a subelement are close together, they join or "'bridge"' during reaction when their volume increases after the conversion of Nb into the more voluminous Nb_3Sn. This leads to a so-called effective filament diameter much larger than the filament itself with flux jumps and large magnetization. This problem could be solved by spacing the filaments more widely apart. However, this would lower the overall J_c, thus invalidating one of the chief advantages of the process.

Fig. 3.5 shows an unreacted IT wire of 1 mm diameter by Intermagnetics General Corporation (IGC).

3.5 The modified jelly roll

The Modified Jelly Roll (MJR) is a variant of the internal tin method pursued by Teledyne Wah Chang company in the US. It consists of two parallel sheets of niobium and copper rolled around a solid tin rod. In this way the niobium part in the non-copper area is increased to 35%. The roll is inserted in a copper tube to form a billet. During drawing the niobium cross section is reduced by ≈750 times and shaped as a hexagonal rod.

A second billet is then assembled using the hexagonal rods, and drawn to the final wire size. No annealing is required during the process. Protecting barriers have to be inserted between the tin core and the niobium sheet, between the niobium and copper sheets, and before the external stabilizing copper. For this purpose tantalum, vanadium, and niobium are used. Fig. 3.6 illustrates the main steps of this process.

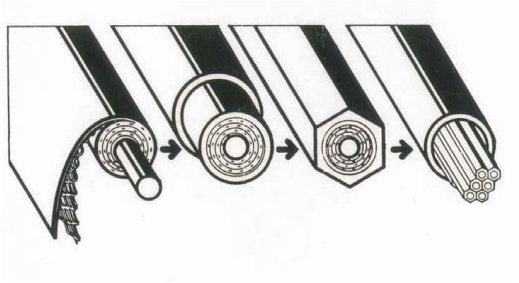

Figure 3.6: Modified jelly roll.

The same factors as in the IT method characterize the conductor properties **??**. Like the IT process, this technology also suffers from filament "'bridging"' [11].

3.5.1 The restacked rod process and the hot extruded rod process

Due to the high performance of Nb3Sn made by internal Tin process, it is an attractive material for many types of large magnet systems. However, each application has its own special requirements that require some customisation of the strand. Material made for High Energy Physic (HEP) accelerator applications now have 12 T, 4.2 K, J_c values of 3000 A/mm^2, but require further development to reduce low field flux jump instabilities. Strands for ITER central solenoid coils have modest critical current density requirements, but very low hysteresis losses are important.

OI–ST (Oxford Instruments–Superconducting Technology) is working on several approaches to reduce the effective filament diameter, including subdividing the sub–elements, and restacking a larger number of sub–elements in the final restack billet.

Most of the internal tin strand is now made using the Restacked Rod Process (RRP). This method uses Nb rod extrusion, and replaces the older MJR process route. Both the performance and yield of RRP strand are greater than for MJR process, and therefore RRP is more amenable to large–scale manufacturing.

One approach OI–ST has taken to scale–up the internal tin production is the development of the Hot Extruded Rod Process (HER).

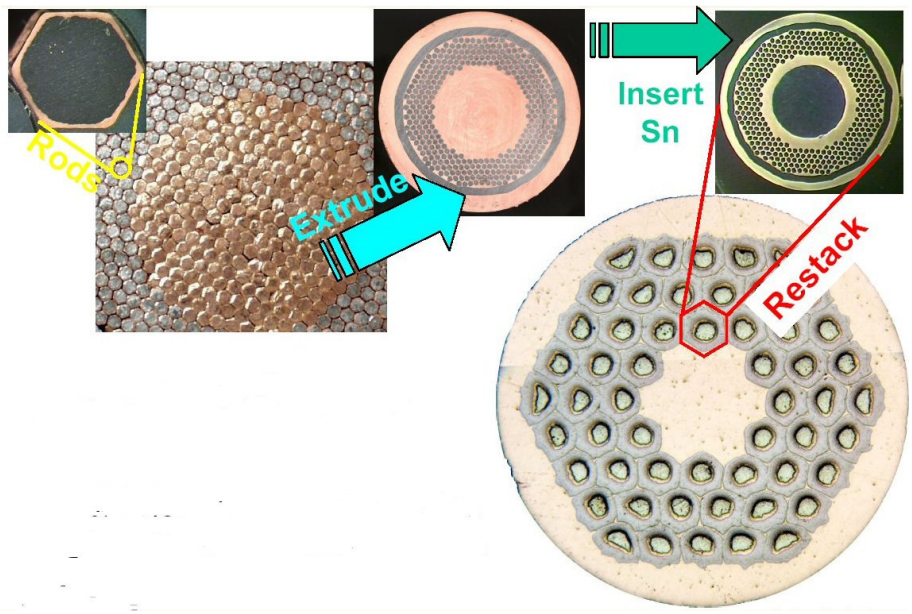

Figure 3.7: Restacked Rod Process (RRP), by Oxford Instruments Superconducting Technology.

The main steps of the HER process are: compacted salt is used as placeholders for Sn during extrusion of large strand billets; after the extrusion, the salt is removed and replaced with Sn rods.

The HER process, where the extrusion is hot, has successfully been used to fabricate a distributed barrier strand having 19–subelements. Although the hot extrusion step gives good and enables the fabrication of large internal tin billets, the requirement of putting the Sn rods in after extrusion limits the number of subelements in the restack to approximately 37 (i.e. the size of the salt holes that the Sn goes into has a practical lower limit). Strand made in this way has reached a J_c (12 T, 4.2 K) of 2500 A/mm^2.

OI–ST also have developed a new method for supplying Ti to dope the Nb_3Sn, by substituting some of the Nb filaments in the sub–element billet with readilyavailable Nb–47wt%Ti alloy.

OI–ST is also developing strand for ITER. Strand has been produced with a J_c (12 T, 4.2 K) ¿ 1100 A/mm^2, losses ¡ 1000 mJ/cm^3. This lower–loss material was made using Nb–47wt%Ti rods to supply the Ti dopant to the remaining pure Nb filaments, thus replacing $Sn-Ti$. Elimination of $Sn-Ti$ is desirable for scale–up, yield, and performance of ITER wire.

3.5.2 The powder in tube process

The Powder in Tube (PIT) process was first developed by the Netherlands Research Foundation and is presently adopted by the Shape Metal Innovation Company (SMI). The basic idea is to fill hollow Nb tubes with fine granulated Nb_2Sn powder and then place them into a Cu matrix. Compared to other methods, a large portion of the non–active bronze content can be replaced by superconductor elements or stabilizing Cu. The non–reacted part of the outer Nb tube acts as barrier between Cu and Nb_3Sn. The development of this technique has allowed producing long 36 and 192 filament strands. In laboratory, samples of 1332 filament strands were also obtained [12]. The next step for large scale PIT strand will be the realization of a 492 filaments strand with an effective filament diameter of about only 20 μm.

Factors like the number of sub–elements, the quality of the powders and the presence of a ternary element characterize the conductor properties [11].

3.6 Summary

The design and manufacturing processes of superconducting composite strands have been briefly explained in this chapter. Nb_3Sn shows higher critical temperature and field than $NbTi$, but is highly brittle, and its critical current is extremely strain sensitive.

Chapter 4

Overview of Superconducting Accelerator Magnets

4.1 Coil

The superconducting coil is the most critical component of a magnet and a sound design is the prerequisite for archieving a high field level and a good field quality throughout the whole current cycle. The presently favoured design has evolved over the past decades. The basic principles stem from the dipoles and quadrupoles of the Fermilab Tevatron (Cole et al. 1979). A number of improvements have been made since at LBL, BNL, DESY, Fermilab, KEK, Saclay, SSCL and CERN. The dipole coils are all based on a suitable approximation of the $cos\theta$ winding configuration. Since the conductor arrangement will be discussed in Chaps. **??** and **??** we concentrate in the following on important details of the design and some practical aspects of coil production.

4.2 Tooling

The demanding task of fabricating 6–m or even 15–m long magnets with cross–sectional accuracies in the order of a few hundredths of a millimetre was first solved at Fermilab with the introduction of *laminated tooling*. The basic idea is that the coil has to conformwith such tight tolerances at any cross section whereas in lonfituudinal direction the requirements are much relaxed. Attempts to produce solid mandrels and molds for coil winding and curing by standard machining techniques had to be given up because they turned out too costly and/or did not comply with the required precision. Precise laminations can be punched at moderate cost and then assembled to long

units of tooling. Laminated tooling has the additional advantage that the mandrels and molds used for short prototypes are identical in cross–section to those series magnets, so the field quality and the quench performance results obtained with prototypes are representative for full–size series magnets.

4.3 Collars

The coils are surrounded with clamps or "'collars"' providing the precise coil geometry and, most importantly, the parge pre–stress in the coil needed for good performance at high field. The collars have to meet the same stringent criteria as the tooling and are made from stamped laminations too. The material is usually stainless–steel but great care must be taken that the material does not become magnetic by welding, cold work (e.g. during the stamping procedure) or upon cool–down to liquid–helium temperature. Only a few steel types are suitable, for instance 316 LN, Nitronic 40 and DIN 1.4429. In addition to the steel type the chemical composition has to be specified. So–called δ–ferrites may be present in stainless steels which are normally converted to austenite by annealing but may re–appear after cold working or welding. For the HERA dipole collars an alluminium–alloy with high yeld strength was chosen ($Al\,Mg5.5\,Mn$ with $\sigma_{\theta 2} = 270\,MPa$) which is totally non–magnetic (Kaiser 1986).

In the Tevatron dipoles the collars are sufficiently stiff to sustain the huge magnetic forces. For the SSC magnets with their larger field this principle would imply rather bulky collar sizes. Here the design has been based on a slinm collar that is elastically deformed by the pre–compressed coil but forced into the design shape by the very sturdy iron yoke. The magnetic forces are largely taken by the yoke. In this type of design the interface between collar and yoke is very critical and particular attention has to be paid to the different thermal shrinking of coil, stainless–steel collar and soft–iron yoke. Owing to the smaller thermal expansion coefficient of soft–iron a certain loss of pre–stress upon cooldown has to be accepted.

The approach at Brookheaven for the RHIC magnets has been different (Thompson et al. 1991). Non–magnetic clamps are avoided but rather the iron yoke itself is used to compress the coil. A precise glass–phenolic form piece serves as a spacer between coil and yoke and also as an excellent electrical insulator. The spacer is produced by injection–molding and the resin is mineral–loaded to reduce shrinkage upon cooldown. The disadvantage of unfavourable differential shrinkage and loss of pre–stress during cooldown remains but creates no problem for the moderate field levels in RHIC.

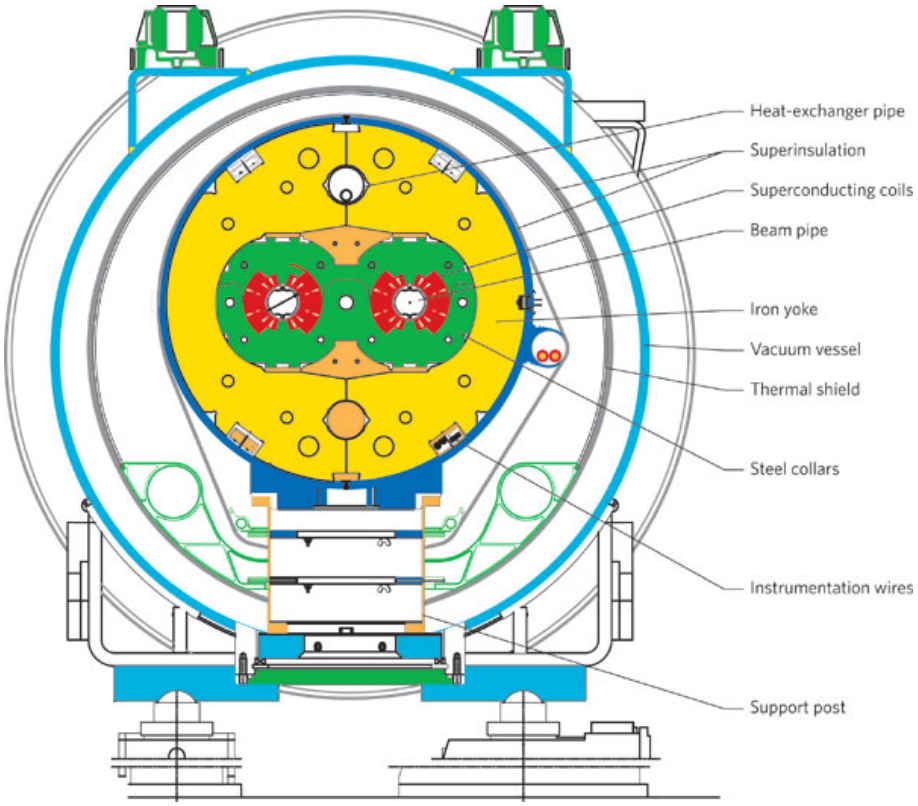

Figure 4.1: Cross–section of the two–in–one design for the main LHC magnets.

4.4 Iron Yoke

The main purpose of teh iron yoke is to screen the fringe field outside teh magnet to an acceptable value of 10 mT or less. Besides the effect on field quality discussed in Chaps. **??** and **??**, some further points have to be taken into consideration before a decision on the type of yoke can be made:

- quench protection system of a long string of magnets,
- heat load on the cryogenic system,
- cooldown and warmup times of the accelerator,
- pre–stress in the coils.

with these points in mind, we summarize the relative virtues and drawbacks of the "'warm–iron"' and the "'cold–iron"' yoke designs.

"'Warm–iron"' yoke

Magnets with this type of yoke have two advantages: the "'cold"' mass is quite small and the field distortions from iron saturation are almost negligible.

The disadvantages are: the iron contributionto the central field is only in the order of 10%, the coil must be well centered in the yoke to avoid eccentricity forces and field distortions (normal or skew quadrupoles in dipole magnets), so many support planes are needed (typically one per metre length) leading to a large heat load on the liquid–helium system; a passive quench protection system by parallel diodes is not easily possible, it would require a costly parallel helium transfer line.

"'Cold-.iron"' yoke

The advantages of a magnet with the iron yoke inside the cryostat and very close to the coil are: the yoke contributes 35–40 % to the central field, so a substantial savings in superconductor is possible; the coil is automatically well centered, no eccentricity forces arise; the yoke is a stiff body and only few support planes are needed (two for a 6–m–long magnet) which reduces the heat load considerably; a passive quench protection system with "'cold"' diodes that bypass the magnet coils is easily implemented.

The disadvantages are: the "'cold"' mass is large; the close proximity between the coil and yokes causes strong iron saturation with a non–linear current–field relationship and field distortions; soft–iron shrinks much less upon cooldown than the coil, so a very high room–temperature pre–stress is needed which might be a danger for the superconductor insulation.

Twin–aperture yoke

For proton–proton colliders two magnet rings are needed. The SSC design was based on separate magnets and cryostats while for the LHC the idea of the twin–aperture magnet was adopted, for financial reasons and to save space. Two collared coils of opposite field orientation are put into a common iron yoke and cryostat (Fig. 4.1). Most of th emagnetic flux returns through the neighbouring coil so the yoke can be made slim at the sides in spite of the high design field of 8.4 T. A clear disadvantage of the "'two–in–one"' principle is the loss of left–right symmmetry for either coil. The dipoles suffer from normal quadrupole components which may be as large as 2% at high excitation. Special measures are taken to reduce these effects, for instance by using ferromagnetic inserts in the non–magnetic collars.

Chapter 5

An Analytical Model for Nb_3Sn Magnets

5.1 Hypotheses

A good model stems from the best compromise between accuracy and simplicity, the trade–off being based on the information that is searched for. We started from defining the kind of results we aimed at attaining. Many recent papers, among which [13] and [14], have improved our comprehension of the parameter trends in Nb_3Sn magnets. We proceeded along the same lines, analysing the possible ways to improve magnets' performance, and the limits to their improvement.

The analysis needed to take into account the field, the forces induced, the stress in the coil and the displacements, and finally the field quality. To evaluate parametrically magnets behavior, a simple but rather general geometry was chosen for the analytical model.

The analysis was subdivided into 2 main submodels: a magnetic model, that included the field and the Lorentz Force, and a mechanical model. The magnetic field produces the lorentz forces, responsible for the stress components, displacements and field quality.

5.1.1 Magnetic Model

Dipole and quadrupole coils for large particle accelerators are much longer ($> 8\,m$) along the axis than wide ($< 0.1\,m$), and therefore the conductors run parallel to the beam over the longest part of the magnet (Fig. 5.1(a)). Axial field components remain, also due to the short coil ends (Fig. 5.1(b)). The magnetic and mechanical design of the coil ends have been analysed in [15].

As to our parametric analysis, their effect can appropriately be neglected: recent design techniques, spreading the coil head with epoxy–fiberglass spacers (Fig.5.20), lower the local field, average the sextupole field contribution of the head to zero and move the highest field point to the straight section, where the conductors are firmly confined (a more detailed analysis can be found in [16]). The second feature generating axial components on the field is the deviation of the beam from a straight line, but its amplitude is only about $10\,mm$ for a $9\,m$ dipole. Based on these considerations, we modeled the magnetic field as two–dimensional, thus applying the theory of analytic functions and building a model for magnet–performance that can be given an analytical expression.

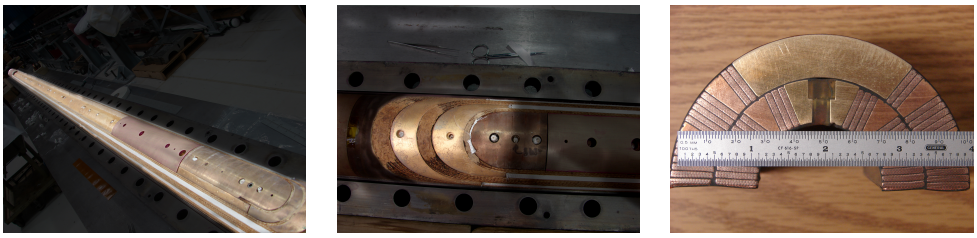

(a) A dipole coil. (b) A coil Head. (c) A dipole cross–section.

Figure 5.1: A typical dipole coil.

Accelerator magnets are usually composed of numerous circular sectors (Fig. 5.1(c)), and the analytical expression of the field they produce is hardly manageable. We therefore chose to analyse the coil sector that eliminates the first undesired multipole term: a 60^o sector for dipoles and a 30^o sector for quadrupoles.

5.1.2 Mechanical Model

Based on the same considerations listed in section 5.1.1, we performed a two–dimensional mechanical analysis of the magnet: both dipoles and quadrupoles are much longer along the axis than wide (a 100:1 ratio), and the peak field does not occur on the coil heads. It has already been said how coils are pre–compressed when placed into their grooves, and firmly confined; this accounts for a two–dimensional plane–strain model. The mechanical cross–section geometry is the same employed in the magnetic model. The symmetries of the problem allow to limit the analysis to one quarter of the dipole cross–section and to one eighth of the quadrupole cross–section.

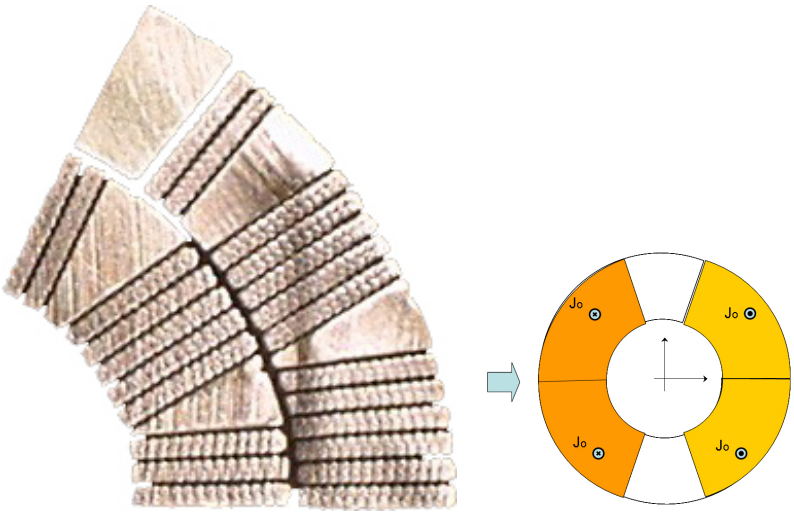

Figure 5.2: Coil Sector.

The following boundary conditions were imposed: $\sigma_r(r_i, \theta) = 0$, $\sigma_\theta(r, \phi_l) = 0$. Boundary conditions on the displacements were $u(r = r_i + w, \theta) = 0$, $v(r, 0) = 0$ (Fig. 5.3).

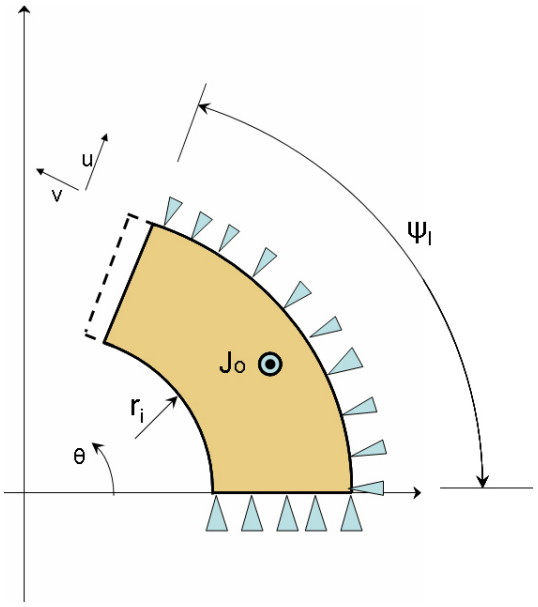

Figure 5.3: Boundary conditions.

5.2 Nb_3Sn Material Properties

We defined simple models for material properties that respond to our requirement of analytical simplicity. Once the critical surface had been modeled, we addressed its correlation with the strain in the superconductor.

5.2.1 Critical Surface

The critical surface of Nb_3Sn, unlike $NbTi$, is not linear over our domain of interest. The Kramer law [17] (and the related fit from Summers [18]) is the most commonly used for its modeling. For Dipoles it serves well the purpose, and it will briefly presented here. The empirical relation proposed for the critical current density in the non–copper section is:

$$J_{sc}(B,T) = CB^{-1/2}\left(1-t^2\right)^2 b^{-1/2}(1-b)^2 \tag{5.1}$$

where

$$t = \frac{T}{T_{c0}} \tag{5.2}$$

and

$$b = \frac{B}{B_{c2}(T)}, \tag{5.3}$$

C being a coefficient independent of temperature and field. The temperature is the He boiling temperature of $4.2\,K$. There are only three input parameters, C, B_{c2} an T_{c0}. For the best commercially available Nb_3Sn cable, the best fit is obtained when

$$\begin{aligned} C &= 22000 \cdot 10^6\, A/m^2 \\ B_{c2} &= 28.7\,T \\ T_{c0} &= 18.3\,K. \end{aligned}$$

producing $3000\,A/mm^2$ at $12\,T$ and $4.2\,K$ in the non–copper. The critical surface is then expressed by:

$$J_{sc}(B) = \frac{C}{B}\sqrt{B_{c2}}\left(1-\frac{B}{B_{c2}}\right)^2\left[1-\left(\frac{4.2}{18.3}\right)^2\right]^2. \tag{5.4}$$

While this is a convenient model for dipoles, whose performance is easily evaluated calculating the value of the field, the field gradient for quadrupoles is determined through more articulated expressions, and the algebraic form

suggested by [18] does not allow an explicit solution for the critical gradient. We chose then to use the hyperbolic fit proposed in [19]:

$$J_{sc}(B) = c\left(\frac{b}{B} - 1\right) \; B < b \tag{5.5}$$

with the constants $c = 3.4 \cdot 10^9 \, A/m^2$ and $b = 22.3 \, T$ at $4.2 \, K$. These values between $11 \, T$ and $17 \, T$ agree within 5% with the Kramer law using the typical parameters for a good Nb_3Sn superconductor.

The current density across the magnet varies substantially from its value across the superconductor: a practical cable is made of an insulated conductor, composed of wires, made of Nb_3Sn filaments in a copper matrix. This fact is commonly addressed by defining an engineering current density, i.e. the current density flowing in the insulated conductor:

$$J_e = k_{w_c} k_{c_i} \frac{J_{sc}}{1 + \nu_{Cu-sc}} = k J_{sc}$$

where k_{w_c} is the ratio between the area of the strands in the conductor and the area of the bare conductor, and k_{c_i} between the area of the bare conductor and of the insulated conductor; ν_{Cu-sc} is the volume ratio between copper and superconductor in the strands. Typical values are 0.85 0.9 for both k_{w_c} and k_{c_i}, and 1 to 2 for ν_{Cu-sc}, thus producing for k values in a range between 0.25 and 0.35. The value used in the analysis was 0.3.

5.2.2 Equivalent Strain and Strain Sensitivity

The effect of strain on the critical current has been measured for specific load cases and the accuracy of the data doesn't compare with that of field–sensitivity measurements. In order to include the effect of strain in the model, we first needed an equivalent stress/strain. Once a scalar representing the strain tensor is defined, the dependence of the critical current on the strain tensor can be modeled, based on the experiments performed, for instance, in [1].

Equivalent Strain

In order to determine a rule that assigns to each tensor a scalar that represents it, we need data exploring all the dimensions of the tensor. In our case, being the problem essentially 2D, we would need at least two load cases that produce a linearly independent strain tensor. Unfortunately, experiments on the sensitivity of Nb_3Sn cables to strain have all been conducted in uniaxial stress–state. We shall then suggest a simple experiment that would provide

the necessary load case variety. Before going any further, we should consider that the strain tensor should reach closer to the physics of the phaenomenon than the stress tensor, considered that it is lattice deformations that affect the superconductor's properties (2).

As anticipated above we need two different load conditions that produce two linearly independent strain tensors. Transport properties measurements in [1] were based on the principle of applying transverse pressure on a sample and then measuring the quench current. We can think of two different boundary conditions for the cable, which will produce differences in the current density performance: plane stress with free sides, an plane stress with constraint sides (Fig. 5.4).

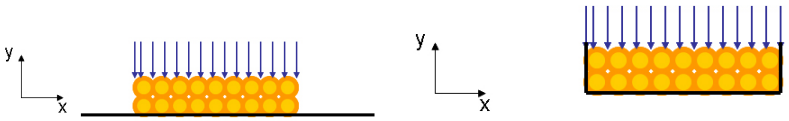

(a) Case A: Free Sides. (b) Case B: Constraint sides.

Figure 5.4: Sample Cross-Section.

The first load case, represented in Fig. 5.4(a), has $\sigma_{yy} = -p$ and $\sigma_{xx} = \sigma_{zz} = 0$. It can therefore be represented by the matrix

$$\begin{pmatrix} 0 & 0 & 0 \\ 0 & -p & 0 \\ 0 & 0 & 0 \end{pmatrix}.$$

The strain is given by:

$$\begin{pmatrix} \nu\frac{p}{E} & 0 & 0 \\ 0 & -\frac{p}{E} & 0 \\ 0 & 0 & \nu\frac{p}{E} \end{pmatrix}.$$

The second load case, represented in Fig. 5.4(b) has $\sigma_{yy} = -p$, $\sigma_{xx} = -\nu p$ and $\sigma_{zz} = 0$. To generalize the load case, we suppose to give a preload on the x direction equal to ϵ_{xx0}. The strain tensor can be represented by:

$$\begin{pmatrix} \epsilon_{xx0} & 0 & 0 \\ 0 & (\nu^2-1)\frac{p}{E} - \nu\epsilon_{xx0} & 0 \\ 0 & 0 & \nu(1+\nu)\frac{p}{E} - \nu\epsilon_{xx0} \end{pmatrix}.$$

The following step consists in defining a list of candidate equivalent strains; the physics of the phaenomenon suggest that we pick strain–related

scalars to describe the stress tensor: this to take into account the fact that the loss of superconductive properties is connected to the deformations of the crystal lattice. For each candidate equivalent strain, a prediction of the performance of the first load case with respect to the second can be made. This prediction can then be matched to the experiment outcome to determine which model best describes the real phaenomenon. Our candidates' list can be reduced to three by choosing the ones that seem to represent the best trade–off between simplicity and accuracy in representing the *strain tensor*:

The Maximum Absolute Eigenvalue is $\frac{p}{E}$ in case A and $max\left[(1-\nu^2)\,\frac{p}{E}+\nu\epsilon_{xx0},\,\nu\,(1+\nu)\,\frac{p}{E}-\nu\epsilon_{xx0},\,\epsilon_{xx0}\right]$ in case B from Fig. 5.4.

$$\begin{aligned}\epsilon_{eqA} &= \tfrac{p}{E}\\ \epsilon_{eqB} &= max\left[(1-\nu^2)\,\tfrac{p}{E}+\nu\epsilon_{xx0},\,\nu\,(1+\nu)\,\tfrac{p}{E}-\nu\epsilon_{xx0},\,\epsilon_{xx0}\right]\end{aligned}$$

The Maximum Angular Deformation , i.e. the maximum diameter of the Mohr's circles of strain, gives:

$$\begin{aligned}\epsilon_{eqA} &= \tfrac{p}{E}\,(1+\nu)\\ \epsilon_{eqB} &= max\left[(1+\nu)\,\tfrac{p}{E},\,\nu\,(1+\nu)\,\tfrac{p}{E}-(1+\nu)\,\epsilon_{xx0}\right]\end{aligned}\quad .$$

The Maximum Angular Deformation on the Cross Sectional Plane that is to say, an equivalent strain proportional to the modulus of the difference between the principal stresses on the cross–sectional plane, gives:

$$\begin{aligned}\epsilon_{eqA} &= (1+\nu)\,\tfrac{p}{E}\\ \epsilon_{eqB} &= (1-\nu^2)\,\tfrac{p}{E}+(1+\nu)\,\epsilon_{xx0}\end{aligned}\quad .$$

The results vary as a function of the Poisson Modulus. In Fig. 5.5(a), 5.5(b) and 5.5(c) the equivalent strains are reported, respectively for *Maximum Eigenvalue*, *Maximum Angular Deformation* and and *Maximum angular deformation on cross section*, as functions of the Poisson modulus, for a pressure of $100\,MPa$, and a Young's Modulus of $40\,GPa$. For load case B, two different cases are reported: one with null pre-stress, and one with $\epsilon_{xx0} = -0.001$ (Fig. 5.5). We can plot the equivalent strains as functions of the pressure on the cable for $\nu = 0.3$ (Fig. 5.6).

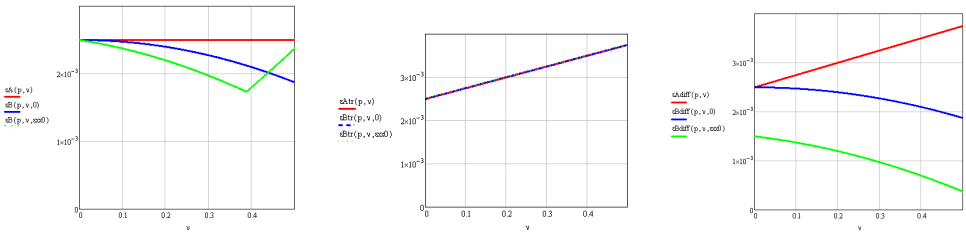

(a) ϵ_{eq}: Maximum Eigenvalue. (b) ϵ_{eq}: Maximum Angular Deformation. (c) ϵ_{eq}: Maximum Angular Deformation on Cross–section.

Figure 5.5: Equivalent Strain vs Poisson's ratio.

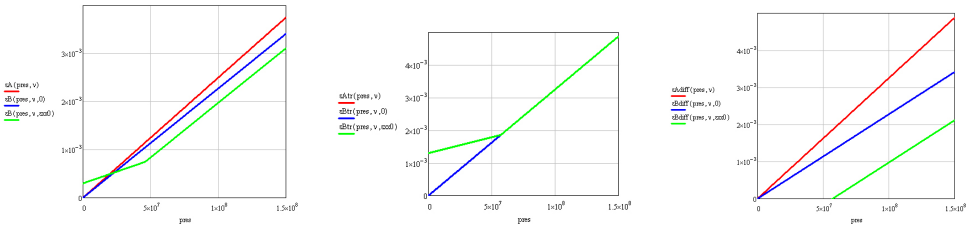

(a) ϵ_{eq}: Maximum Eigenvalue. (b) ϵ_{eq}: Maximum Angular Deformation. (c) ϵ_{eq}: Maximum Angular Deformation on Cross–section.

Figure 5.6: Equivalent Strain vs Transverse pressure on Sample, $\nu = 0.3$.

Sensitivity of Nb_3Sn cables to transverse pressure

Fig. 5.7 shows a transverse pressure test at field from [1]: without entering into details as to the reversibility of the transport properties, the behaviour seems to be sufficiently well described by a bi–linear function.

We chose to represent the cable sensitivity with a bi–linear function that at $150\,MPa$ of transverse pressure in uniaxial load performs at 88% of what it does at null pressure, and that is completely deteriorated at $210\,MPa$. Using this sample uniaxial performance, we can predict the performance of the constraint cable according to each of the three candidate equivalent stresses: the *maximum eigenvalue* model, the *maximum angular deformation* model and the *maximum angular deformation on the cross–section* model.

The results obtained by the experiment can be compared to each of the three equivalent strain models (Fig. 5.8), to find the match. We shall also make some considerations on the effect of the specific equivalent stress on

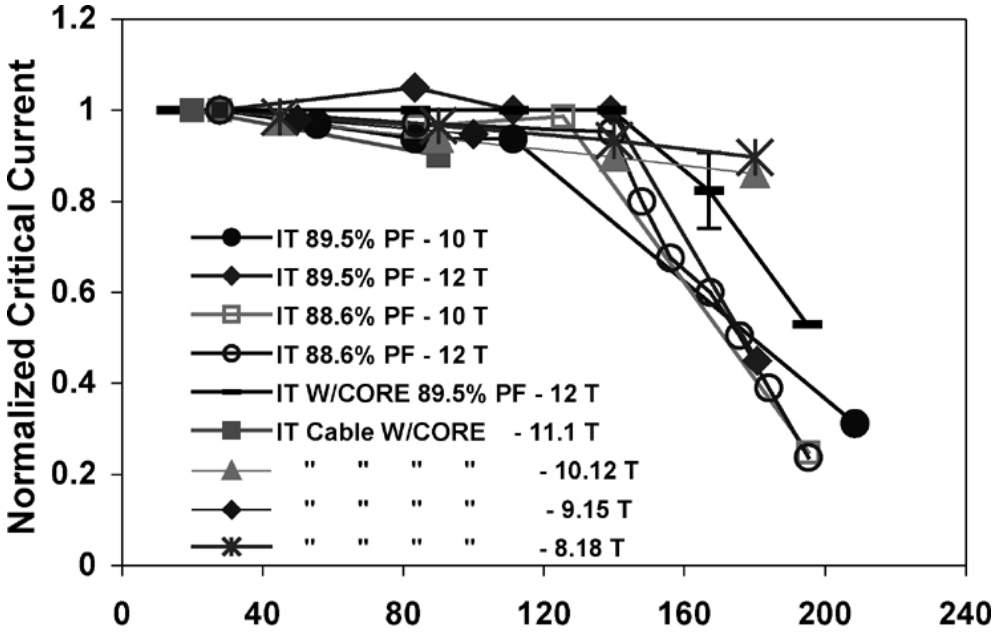

Figure 5.7: Normalized current vs. transverse pressure for typical cable tests [1].

the performance estimates in section 6.3.

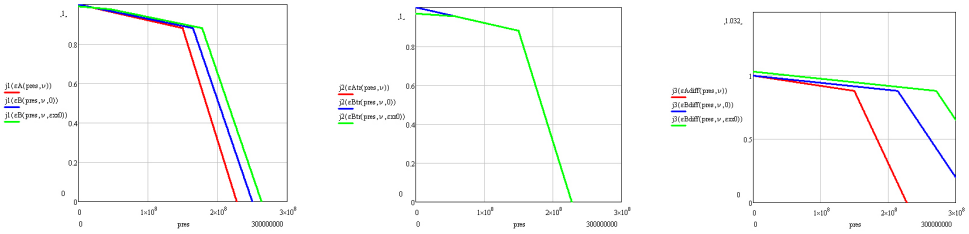

(a) ϵ_{eq}: Maximum Eigenvalue.

(b) ϵ_{eq}: Maximum Angular Deformation.

(c) ϵ_{eq}: Maximum Angular Deformation on Cross–section.

Figure 5.8: Previews of experimental data.

5.3 Magnetic Field Model

Following the considerations made in section 5.1.1, we considered the magnetic field essentially as two–dimensional, with the advantages of applying the theory of analytic functions and building a model for magnet–performance that can be given an analytical expression, without the need to run finite element analyses.

5.3.1 2D Complete Field Expression

As shown by [16], the field $\vec{B}$ can be expressed as the curl of the vector potential $\vec{A}$:

$$\vec{B} = \vec{\nabla} \times \vec{A}.$$

For our two–dimensional problem the vector potential has only a z component. In cylindrical coordinates, where the magnetic axis is chosen as the z direction, the r and θ components of the magnetic field vector can be computed as:

$$B_\theta(r,\theta) = -\frac{\partial A_z}{\partial r} \tag{5.6}$$

$$B_r(r,\theta) = \frac{1}{r}\frac{\partial A_z}{\partial \theta}. \tag{5.7}$$

The vector potential on a point P generated by a line current I parallel to the z–direction (Fig. 5.9 – just like the cables in the coil) is expressed by ([20]):

$$A_z(r,\theta) = \frac{\mu_0 I}{2\pi}\sum_{n=1}^{\infty}\frac{1}{n}\left(\frac{r}{a}\right)^n \cos\left[n\left(\theta-\phi\right)\right] \tag{5.8}$$

when $r < a$; at a distance $r > a$ the vector potential can be obtained from:

$$A_z(r,\theta) = -\frac{\mu_0 I}{2\pi} ln\left(\frac{r}{a}\right) + \frac{\mu_0 I}{2\pi}\sum_{n=1}^{\infty}\frac{1}{n}\left(\frac{a}{r}\right)^n \cos\left[n\left(\theta-\phi\right)\right]. \tag{5.9}$$

We observe that, referring to Fig. 5.9, in any coil that is symmetric with respect to the x–axis and anti–symmetric with respect to the y–axis, for any current $+I$ at an angle ϕ, there exist three more currents: $+I$ at $-\phi$, $-I$ at $\pi-\phi$ and $\pi+\phi$ (Fig. 5.2(b)). The vector potential of these four currents, using Eqs. 5.8 and 5.9, is

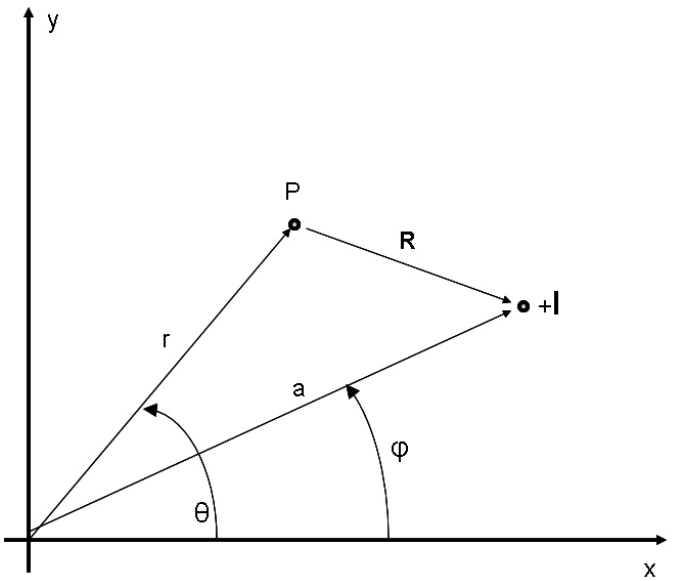

Figure 5.9: Vector potential of a line current

$$A_z(r,\theta) = \frac{2\mu_0 I}{\pi} \sum_{n=1,3,5,\ldots} \frac{1}{n} \left(\frac{r}{a}\right)^n \cos(n\theta)\cos(n\phi) \tag{5.10}$$

for $r < a$, and

$$A_z(r,\theta) = \frac{2\mu_0 I}{\pi} \sum_{n=1,3,5,\ldots} \frac{1}{n} \left(\frac{a}{r}\right)^n \cos(n\theta)\cos(n\phi) \tag{5.11}$$

for $r > a$. This configuration is peculiar to all ideal dipoles and real dipoles with perfect symmetry. We can conclude that a coil with dipole symmetry exhibits only *cosine* terms (no *sine* terms), and only *odd* values of n appear.

Quadrupoles can be treated similarly. For any ideal quadrupole and real quadrupole with perfect quadrupole symmetry we find that, for any current $+I$ at an angle ϕ, there exist seven more currents: $+I$ at $-\phi$, $\pi - \phi$ and $\pi + \phi$; $-I$ at $\frac{\pi}{2} + \phi$, $\frac{\pi}{2} - \phi$, $-\frac{\pi}{2} + \phi$ and $-\frac{\pi}{2} - \phi$. Therefore we find:

$$A_z(r,\theta) = \frac{4\mu_0 I}{\pi} \sum_{n=2,6,10,\ldots} \frac{1}{n} \left(\frac{r}{a}\right)^n \cos(n\theta)\cos(n\phi) \tag{5.12}$$

for $r < a$, and

$$A_z(r,\theta) = \frac{4\mu_0 I}{\pi} \sum_{n=2,6,10,\ldots} \frac{1}{n} \left(\frac{a}{r}\right)^n \cos(n\theta)\cos(n\phi) \tag{5.13}$$

for $r > a$. When calculating the contribution of one current element to the vector potential, one has to substitute I with $J\,da\,a\,d\phi$. We find then for dipoles:

$$A_z(r,\theta) = \frac{2\mu_0 J}{\pi} \sum_{n=1,3,5,\ldots} \frac{1}{n}\left[\int_r^{r_i+w} \left(\frac{r}{a}\right)^n a\,da + \right. \\ \left. + \int_{r_i}^{r} \left(\frac{a}{r}\right)^n a\,da \right] \int_0^{\phi_l} \cos(n\theta)\cos(n\phi)\,d\phi \quad (5.14)$$

and for quadrupoles:

$$A_z(r,\theta) = \frac{4\mu_0 J}{\pi} \sum_{n=2,6,10,\ldots} \frac{1}{n}\left[\int_r^{r_i+w} \left(\frac{r}{a}\right)^n a\,da + \right. \\ \left. + \int_{r_i}^{r} \left(\frac{a}{r}\right)^n a\,da \right] \int_0^{\phi_l} \cos(n\theta)\cos(n\phi)\,d\phi. \quad (5.15)$$

These two expressions can be integrated analytically, respectively for dipoles and quadrupoles:

$$A_z(r,\theta) = \frac{2\mu_0 J}{\pi} \sum_{n=1,3,5,\ldots} \left[\frac{r^n}{n^2(n-2)} \left[r^{2-n} - (r_i+w)^{2-n} \right] + \right. \\ \left. + \frac{r^{-n}}{(n+2)\,n^2} \left(r^{n+2} - r_i^{n+2} \right) \right] sinn\phi_l cosn\theta \quad (5.16)$$

and

$$A_z(r,\theta) = \frac{4\mu_0 J}{\pi} \left\{ \frac{1}{4} r^2 ln\left(\frac{r_i+w}{r}\right) cos2\theta sin2\phi_l + \right. \\ + \sum_{n=6,10,14,\ldots} \left[\frac{r^n}{n^2(n-2)} \left[r^{2-n} - (r_i+w)^{2-n} \right] sinn\phi_l cosn\theta \right] + \\ \left. + \sum_{n=2,6,10,\ldots} \left[\frac{r^{-n}}{n^2(n+2)} \left[r^{2+n} - r_i^{2+n} \right] sinn\phi_l cosn\theta \right] \right\}. \quad (5.17)$$

In this series (whose convergence is demonstrated, among the others, by [16]) the amplitude of the terms, which we shall call "'multipoles"', goes to 0 as $\frac{1}{n^3}$. An example of the amplitude of each multipole along the radius of the bore is shown in Fig. 5.10 for a general dipole geometry.

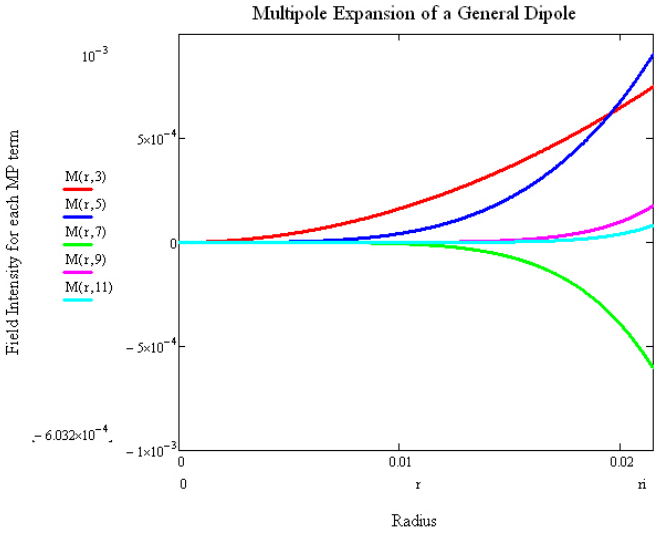

Figure 5.10: Multipole Expansion of a general dipole layer

5.3.2 Multipole Fields and Approximated 2D Field Expression

To better understand the physical meaning of the multipole terms, we shall consider how to create an ideal dipole or quadrupole. As seen in Eq. 5.8, a single line current produces multipole fields of every order n. To obtain a perfect multipole, we should consider an arrangement of current conductors, running parallel to the z axis, which are placed on a cylinder of radius a. A pure multipole field, containig just the single order $n = m$, is obtained inside the cylinder if the current distribution as a function of the azimuthal angle ϕ is given by

$$I(\phi) = I_0 cos(m\phi). \tag{5.18}$$

This is easily found when computing the vector potential resulting from the current distribution 5.18:

$$A_z(r,\theta) = \frac{\mu_0 J}{2\pi} \sum_{n=1}^{\infty} \frac{1}{n} \left(\frac{r}{a}\right)^n \int_0^{2\pi} \cos(m\phi) \cos[n(\theta - \phi)]\, d\phi. \tag{5.19}$$

Using the orthogonality of the trigonometric functions, we can see that the integral vanishes unless $n = m$, so that only a single term in the sum remains:

$$A_z(r,\theta) = \frac{\mu_0 I_0}{2}\frac{1}{m}\left(\frac{r}{a}\right)^m \cos(m\theta) \tag{5.20}$$

$$B_\theta(r,\theta) = -\frac{\mu_0 I_0}{2a}\left(\frac{r}{a}\right)^{m-1} \cos(m\theta) \tag{5.21}$$

$$B_r(r,\theta) = -\frac{\mu_0 I_0}{2a}\left(\frac{r}{a}\right)^{m-1} \sin(m\theta). \tag{5.22}$$

For $m = 1, 2, 3$ we obtain dipole, quadrupole and sextupole fields, respectively. In cartesian coordinates, the dipole has a constant y component and a null x component, while the quadrupole varies linearly with x and y. The fields 5.21 and 5.22 are the so–called *normal multipole* fields. If we rotate the current distribution 5.18 by an angle of $\pi/(2m)$, we obtain a $sin(m\phi)$ distribution leading to *skew multipole fields*. As noted in 5.3.1, the hypothesis of perfect symmetry eliminates all skew multipoles. In real magnets, they arise from an angular misalignment of the normal quadrupoles; in our model they were neglected.

Distributions as that suggested in 5.18 are difficult to obtain in real magnets, and the ideal dipoles and quadrupoles are approximated with coil sectors. While we shall consider this later on, it should be anticipated that state–of–the–art magnet design allows undesired multipole terms to be 10^4 times smaller than the desired multipole. On account of this, and with the objective of building an analytical model, we neglected all terms with $n \geq 3$ for dipoles and $n \geq 6$ for quadrupoles. Consequently, we expressed the vector potential as:

$$A_z(r,\theta) = -\frac{2\mu_0 J}{\pi}\left[r\left[r - (r_i + w)\right] + \frac{1}{3r}\left(r^3 - r_i^3\right)\right] sin\phi_l cos\theta \tag{5.23}$$

for dipoles and

$$A_z(r,\theta) = \frac{4\mu_0 J}{\pi}\left[\frac{r^2}{4} ln\left(\frac{r_i + w}{r}\right) cos2\theta sin2\phi_l + \right. \\ \left. + \frac{r^{-2}}{16}\left[r^4 - r_i^4\right] sin2\phi_l cos2\theta\right] \tag{5.24}$$

for quadrupoles. Magnetic field components can be computed using 5.6 and 5.7.

5.3.3 Quality of Approximation

In this section we shall examine the accuracy of the model based on the aforementioned approximations. The field distribution is used for two main purposes throughout this work: to evaluate the performance of the magnet, and to evaluate the stress across the coil. On account of this, the model has been run with the aforementioned approximations first, and then using a field approximation that includes the first seven multipole terms. In Fig. 5.11 a comparison between the results is displayed for dipoles. The maximum field and the maximum stress are plotted as functions of the width of the coil for a common dipole geometry.

Results show that the *maximum field* estimates differ by less than 0.3%, while the *maximum stress* estimates differ by less than 2%, suggesting that the approximation is legitimate.

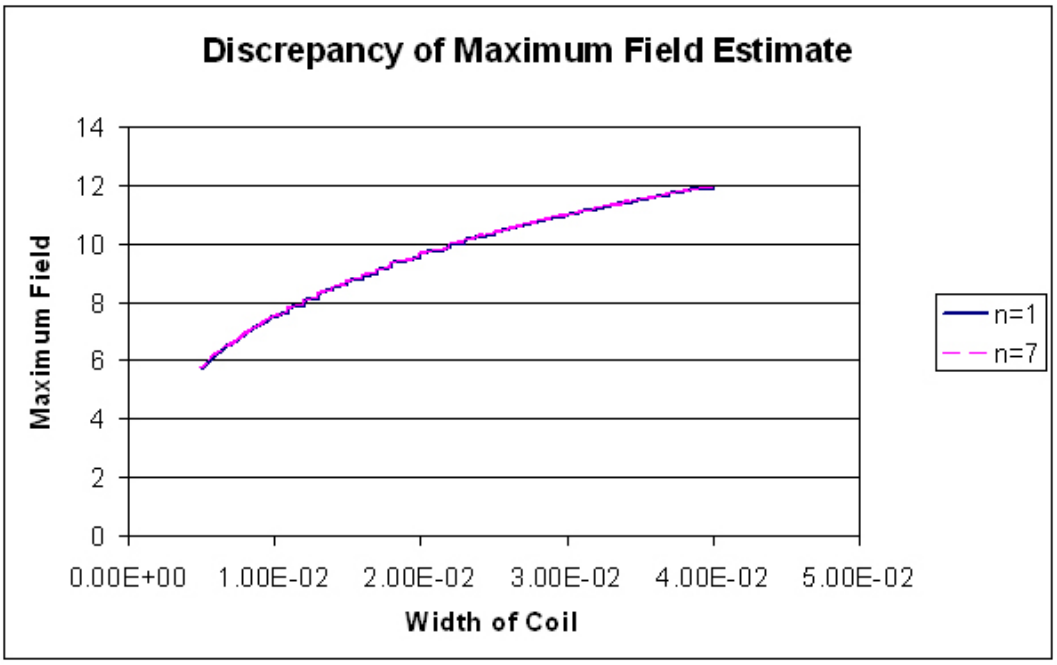

(a) Discrepancy on Maximum Field

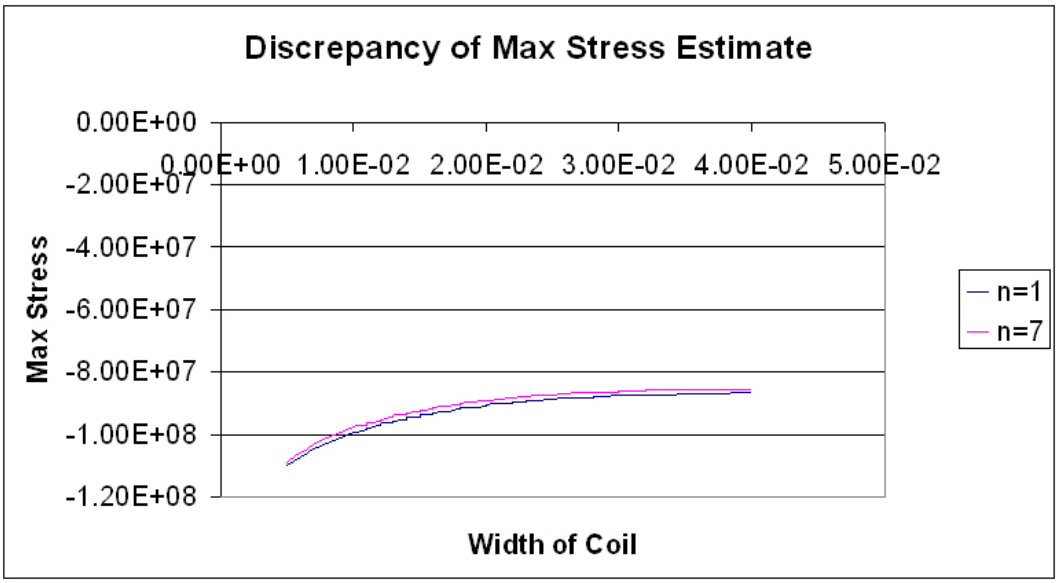

(b) Discrepancy on Maximum Stress

Figure 5.11: Accuracy of the Field Approximation

5.4 Stress, Strain and Displacements

5.4.1 Stress

The hypotheses underlying the mechanical model are those listed in section 5.1.2. Using the notations displayed in Fig. 5.12, we can write the equilibrium equations:

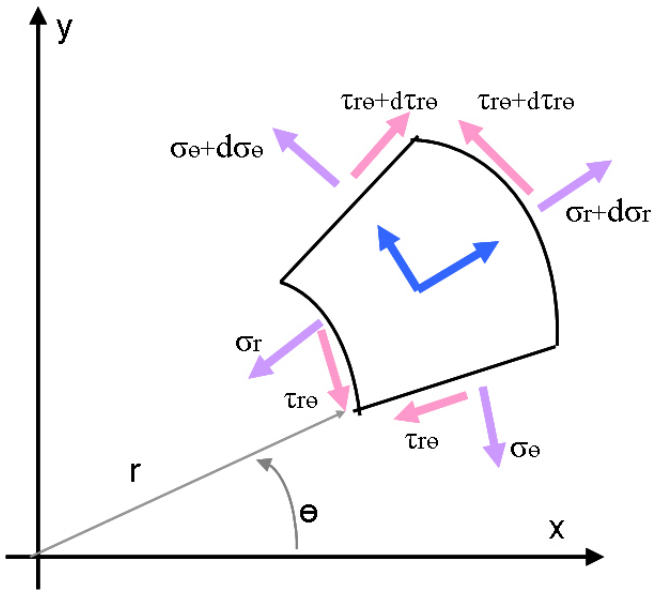

Figure 5.12: Equilibrium of a 2D element in cylindrical coordinates.

$$\frac{1}{r}\frac{\partial \sigma_\theta}{\partial \theta} + \frac{\partial \tau_{r\theta}}{\partial r} + 2\frac{\tau_{r\theta}}{r} + f_\theta = 0$$
$$\frac{\partial \sigma_r}{\partial r} + \frac{\sigma_r - \sigma_\theta}{r} + \frac{1}{r}\frac{\partial \tau_{r\theta}}{\partial \theta} + f_r = 0$$

For an outward current density $\vec{J_0}$, we have:

$$f_r = -B_\theta(r,\theta)\, J_0 = \frac{\partial\left(J_0 A_z(r,\theta)\right)}{\partial r}$$

$$f_\theta = B_r(r,\theta)\, J_0 = \frac{1}{r}\frac{\partial\left(A_z(r,\theta)\, J_0\right)}{\partial \theta}$$

This is a system of partial differential equations. Assuming that the effect of shear stress $\tau_{r\theta}$ is negligible, it can be transformed into two linear differential equations, and therefore allow an analytical solution:

$$\frac{1}{r}\frac{\partial \sigma_\theta}{\partial \theta} + \frac{1}{r}\frac{\partial \left(A_z\left(r,\theta\right) J_0\right)}{\partial \theta} = 0$$
$$\frac{\partial \left(\sigma_r r\right)}{\partial r} - \sigma_\theta + \frac{\partial \left(J_0 A_z\left(r,\theta\right)\right)}{\partial r} r = 0$$

therefore

$$\sigma_\theta\left(r,\theta\right) = -A_z\left(r,\theta\right) J_0 + C_\theta$$
$$\sigma_r\left(r,\theta\right) = \frac{1}{r}\int_{r_i}^{r} \sigma_\theta \, dr - \frac{1}{r}\int_{r_i}^{r} \frac{\partial \left(J_0 A_z\right)}{\partial r} r \, dr + C_r$$

Substituting the boundary conditions:

$$\sigma_\theta\left(r,\phi_l\right) = 0$$
$$\sigma_r\left(r_i,\theta\right) = 0$$

we find:

$$C_\theta = A_z\left(r,\theta_l\right) J_0$$
$$C_r = 0$$

Having neglected the shear stress, the final expressions for the azimuthal and radial stresses are:

$$\sigma_\theta\left(r,\theta\right) = -J_0\left(A_z\left(r,\theta\right) - A_z\left(r,\phi_l\right)\right) \tag{5.25}$$

$$\sigma_r\left(r,\theta\right) = \frac{J_0}{r}\int_{r_i}^{r}\left[A_z\left(\overline{r},\phi_l\right) - A_z\left(\overline{r},\theta\right) - \frac{\partial\left(A_z\right)}{\partial \overline{r}}\overline{r}\right] d\overline{r} \tag{5.26}$$

5.4.2 Maximum Equivalent Stress

Symmetries of the problem allow limiting the analysis to one quarter of the dipole coil cross–section (Fig. 5.13(a)), and one eighth of the quadrupole. To plot the maximum principal stress (remembering that we chose to neglect the shear stress), we start evaluating the maximum azimuthal and radial stresses, and then proceed by chosing the highest of the two. From the equilibrium in the azimuthal direction,

$$\frac{\partial \sigma_\theta}{\partial \theta} = -r f_\theta = -r J_0 B_r.$$

The analytical expression of B_r can be derived from the vector potential, expressed in section 5.3:

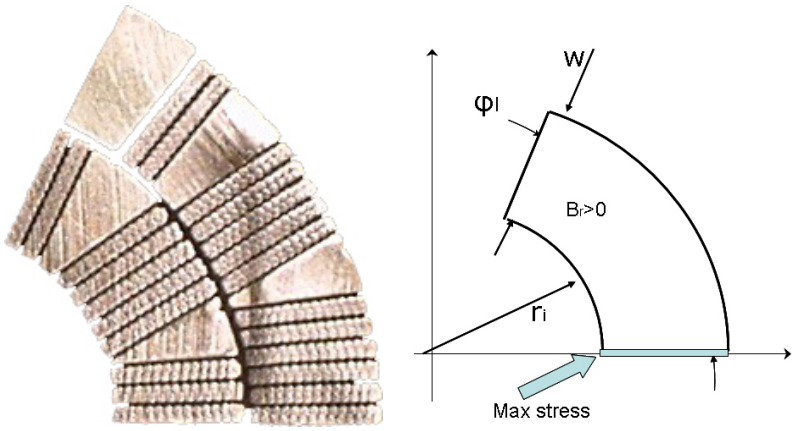

(a) One quarter of the dipole represents the whole section.

(b) Notations.

Figure 5.13: A dipole sector.

$$B_r = C \cdot \left(r^3 - \frac{3}{2}\left(r_i + w\right) r^2 + \frac{r_i^3}{2} \right)$$

where r is the radial coordinate, r_i the inner radius, and w the thickness of the coil (Fig. 5.13(b)). Since $C > 0$, the sign of $\frac{\partial \sigma_\theta}{\partial \theta}$ is equal to the sign of the polynomial reported above. By substituting r_i first, and $r_i + w$ next, in the expression above, we learn that the polynomial is less than 0 at both the inner and outer boundary of the sector. We also notice that

$$\frac{\partial \left(r^3 - \frac{3}{2}\left(r_i + w\right) r^2 + \frac{r_i^3}{2} \right)}{\partial r} = 3r\left(r - r_i - w\right).$$

Since the first derivative doesn't change sign through the coil thickness, the sign of the radial component of the field must be constant across the coil. Therefore $\frac{\partial \sigma_\theta}{\partial \theta} > 0$, and since $\sigma_{\phi_l} = 0$, the maximum absolute value of the azimuthal stress must lie along the mid–section of the coil (Fig. 5.14(a)). Thus, knowing that the maximum equivalent stress is at $\theta = 0$, the point of maximum stress can be found by searching the roots of $\frac{\partial (A_z(r,0))}{\partial r}$, that is to say, by finding the solutions of

$$-4r^3 + 3(r_i + w) \cdot r^2 + r_i^3 = 0.$$

The solutions can be found analytically, and lead to three points, only one of which lies between r_i and w (Fig. 5.14(b)). In order to find the maximum radial stress, we also note from the FEM solutions that the maximum radial

stress lies in the mid–section, and therefore using the same technique we find its maximum (Fig. 5.14(c) and 5.14(d)). The same considerations apply to quadrupoles (Fig. 5.15).

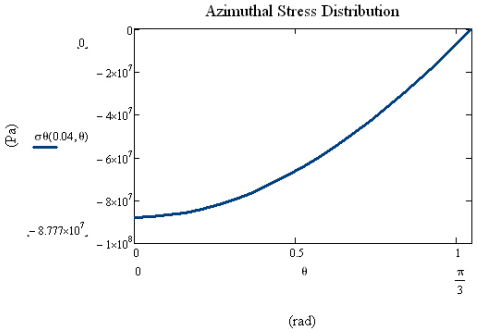

(a) Azimuthal stress at constant radius.

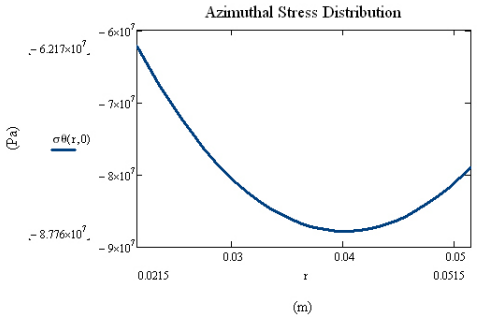

(b) Azimuthal stress along mid–plane.

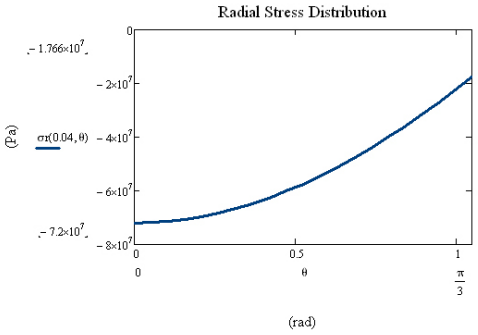

(c) Radial stress at constant radius.

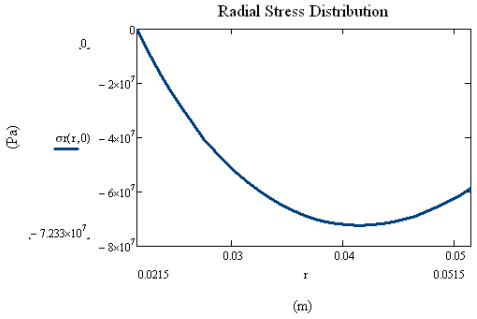

(d) Radial stress along mid–plane.

Figure 5.14: Stress distribution for a typical dipole.

5.4.3 Quality of Approximation

Neglecting the shear stress allowed building an analytical mechanical model for the coil. A comparison between the maximum principal stress given by the mechanical model and that produced by a linear finite element model that includes the shear stress was performed. The two models have been used to solve a 90 mm bore quadrupole geometry with a 40 mm coil thickness, showing a discrepancy of less than 5%. A comparison between the results for such quadrupole is shown in Fig. 5.16. Similar conclusions were drawn by [13].

It should be noted that the quality of the approximation depends on the coordinate system chosen: a cylindrical coordinate system, approximating

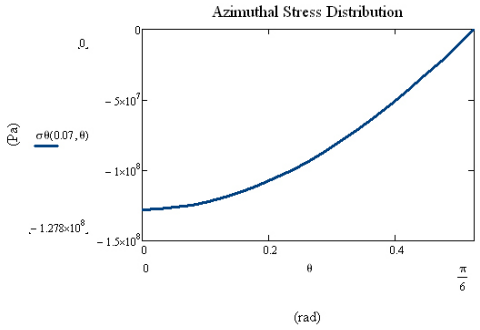

(a) Azimuthal stress at constant radius.

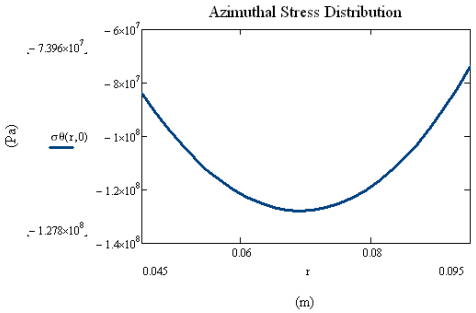

(b) Azimuthal stress along mid–plane.

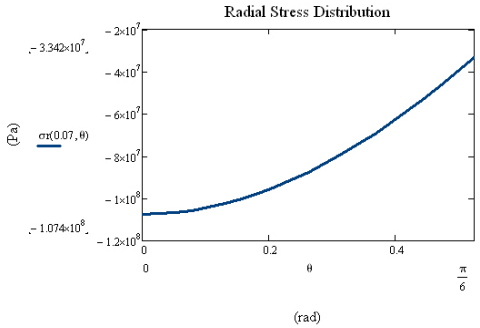

(c) Radial stress at constant radius.

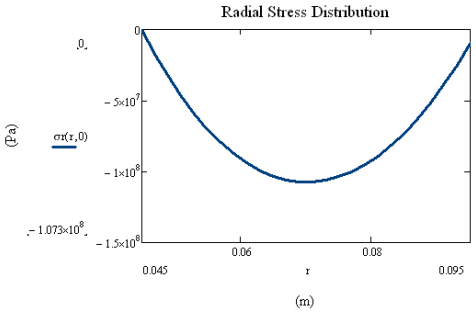

(d) Radial stress along mid–plane.

Figure 5.15: Stress distribution for a typical quadrupole.

the principal coordinate system, is a good choice.

The previous analysis shows that the analytical approach is a good approximation of the stress distribution in a linear isotropic material. Real superconducting magnets are neither linear nor isotropic. The issue of anisotropy is easily addressed: neglecting the shear leads to a solution which is independent from the elastic properties (being the cylindrical coordinate system the principal coordinate system for the material). Plasticity, on the other hand, is addressed in section 7, where an elastoplastic FEM model is analysed, showing that stresses are fairly approximated by the linear model (unlike displacements).

5.4.4 Displacements

The strain components, for a linear isotropic material, are a linear combination of the stress components. As anticipated in section 5.1.2, we used a plane strain model:

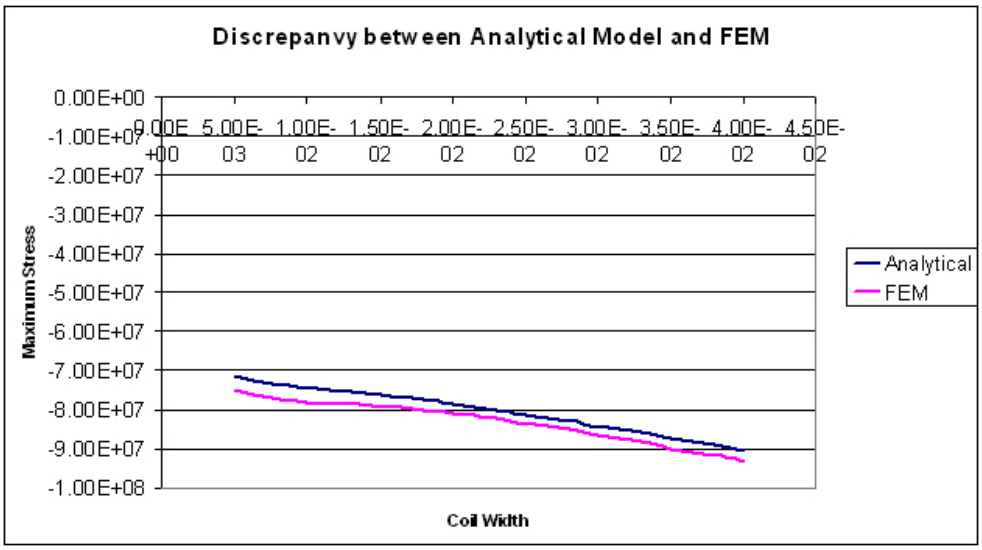

Figure 5.16: Discrepancy between the Analytical and the Finite Element model.

$$\begin{bmatrix} \epsilon_{rr} \\ \epsilon_{\theta\theta} \\ \epsilon_{r\theta} \end{bmatrix} = \begin{bmatrix} \frac{1-\nu^2}{E} & -\frac{\nu(1+\nu)}{E} & 0 \\ -\frac{\nu(1+\nu)}{E} & \frac{1-\nu^2}{E} & 0 \\ 0 & 0 & \frac{1}{G} \end{bmatrix} \cdot \begin{bmatrix} \sigma_{rr} \\ \sigma_{\theta\theta} \\ \tau_{r\theta} \end{bmatrix} \tag{5.27}$$

Having determined the strain components, we integrated them to get the displacements. This had many uses: it gave us indications about the losses in field quality due to geometry variations, and it was necessary to determine the minimum preload needed. Knowing that:

$$\epsilon_r = \frac{\partial u}{\partial r}$$
$$\epsilon_\theta = \frac{1}{r}\frac{\partial v}{\partial \theta} + \frac{u}{r}$$

with the boundary conditions of Fig. 6.29(a):

$$u(r = r_i + w, \theta) = 0$$
$$v(r, 0) = 0$$

we can write

$$u(r,\theta) = \int_{r_i}^{r} \epsilon_r(\overline{r},\theta)\, d\overline{r} - \int_{r_i}^{r_i+w} \epsilon(\overline{r},\theta)\, d\overline{r}$$

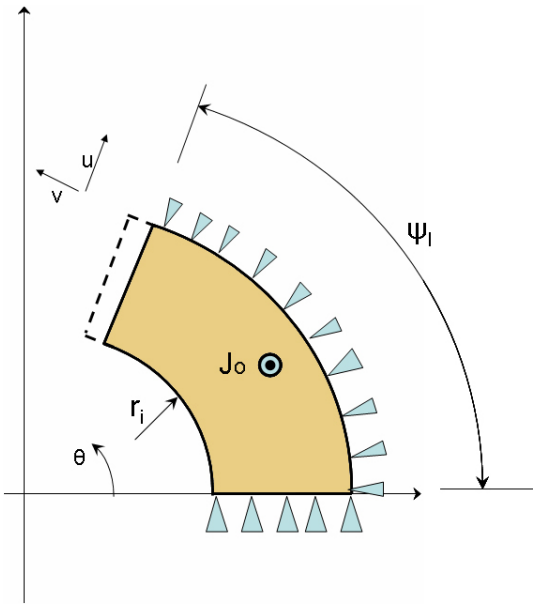

Figure 5.17: Boundary conditions.

$$v(r,\theta) = \int_0^{\theta} \epsilon_{\theta}(r,\overline{\theta}) r \, d\overline{\theta} - \int_0^{\theta} u(r,\overline{\theta}) \, d\overline{\theta}.$$

The minimum preloaded needed in order for the azimuthal extension of the coil not to change under Lorentz forces is the load the produces a coil compression in the azimuthal direction equal to

$$\Delta_{min} = max_r \left[v(r,\varphi_l) \right] \tag{5.28}$$

for a given current density J_0 (Fig. 5.18).

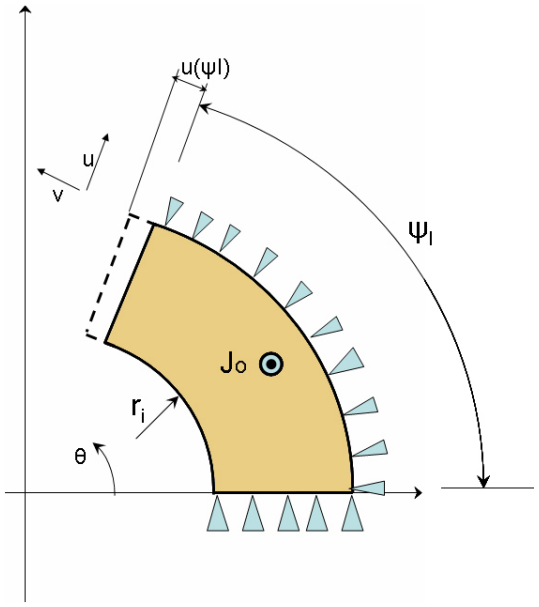

Figure 5.18: Determining the minimum preload.

5.5 Field Intensity

As anticipated in Section 5.1, magnet requirements belong to two main categories: field intensity and field quality. We will address the former in this section, and the latter in the following.

The value of maximum field intensity (or gradient intensity for quadrupoles) in a magnet is essentially limited by the quench of the superconducting cable. Recalling chapter 2, a quench takes place when either the field or the temperature in the superconductor exceeds the critical values at a given current density. Temperature rises above its critical value when the magnet quenches due to its mechanical movement (a model was proposed by [21]). We focused on the field, assuming that the temperature stays constant through the magnet.

There is, nevertheless, another effect that affects magnet performance: the critical current density depends on strain ([1]). As stated in section 5.2.2, similarly to what was done by [13], the maximum absolute principal stress was compared with the reference value of the maximum tolerated compressive stress of $150\,MPa$. The effect of transverse pressure is then analysed in deeper detail in 6.3.

5.5.1 Dipoles: Maximum Field

The maximum field intensity is reached when the current density is equal to the critical current density in at least one point of the coil. With the assumption that the current density is constant in the cross section, the coil quenches at the peak field, which in our dipole field approximation is located along its inner surface. The maximum field can be expressed as:

$$B_{max} = \sqrt{B_\theta^2\left(r_i, \frac{\phi_l}{2}\right) + B_r^2\left(r_i, \frac{\phi_l}{2}\right)} = J\,\widehat{B}_{max}$$

The maximum field intensity and the maximum current density can both be found solving the system with Eq. 5.1:

$$\begin{cases} B_{max} = J\,\widehat{B}_{max} \\ J_c = kCB^{-1/2}\,(1-t^2)^2\,b^{-1/2}(1-b)^2 \end{cases}$$

We find:

$$J_c = \frac{\frac{2\widehat{B}_{max}}{B_{c2}} - 2\sqrt{\frac{1}{\Omega}}}{2A} \tag{5.29}$$

where:

$$\Omega = \frac{kC}{\widehat{B}_{max}}\sqrt{B_{c2}}\left[1-\left(\frac{4.2}{18.3}\right)^2\right]^2$$

and:

$$A = \frac{\widehat{B}^2_{max}}{B^2_{c2}} - \frac{1}{\Omega}.$$

5.5.2 Quadrupoles: Maximum Gradient

The estimate of the maximum gradient in quadrupoles is carried out with the method proposed by [19]. Both the field gradient $G\,[T/m]$ at the centre of the quadrupole and the peak field $B_{max}\,[T]$, i.e. the largest value (in module) of the magnetic field in the coil, are proportional to the current density J:

$$G = J\gamma(r_i, w)$$

$$B_{max} = J\beta(r_i, w).$$

We compute $\gamma\,[Tm/A]$ trough an integration of the Biot–Savart law:

$$\gamma = \gamma_0 ln\left(1+\frac{w}{r_i}\right),$$

where:

$$\gamma_0 = \frac{4}{5}10^{-6}\sin\left(\frac{\pi}{3}\right).$$

For $\beta\,[Tm^2/A]$ we use the form

$$\beta = r_i\lambda\gamma,$$

where $\lambda\,[\text{adimensional}]$ is the ratio between the peak field and the gradient times the aperture. The dependence of λ on w/r_i can be approximated by:

$$\lambda = a_{-1}\frac{r_i}{w} + 1 + a_1\frac{w}{r_i}$$

where a_{-1}, and a_1 are constants related to the 30^o lay-out. Substituting the expression of the critical surface (Eq. 5.5) in the maximum field expression, we can find the maximum allowed current density for a given geometrical

configuration and material. Multiplying the critical current density by γ we get the critical gradient:

$$G_c = \gamma \cdot \frac{kc}{2} \left(\sqrt{\frac{4b}{\beta kc} + 1} - 1 \right).$$

Substituting the layout parameters of Eq. 5.5 one obtains an explicit equation for the Nb_3Sn case.

5.6 Field Quality Evaluation

As anticipated in section 5.3.2, a perfect multipole of order n can be obtained by a current distribution across the coil with a $\cos(m\varphi)$ dependence. As this distribution can hardly be obtained with a superconducting cable of constant cross section, it is usually approximated with sufficient accuracy by means of current shells (Fig. 5.19).

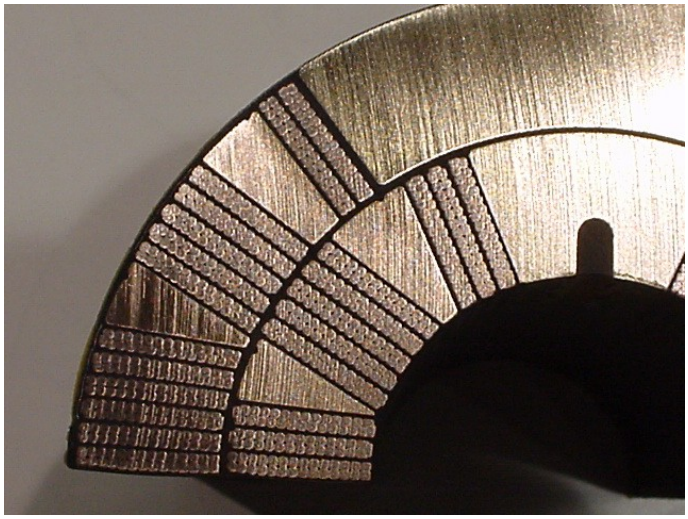

Figure 5.19: Approximating a $\cos(\varphi)$ distribution with current shells.

We have already shown (section 5.3.1) that the vector potential, and therefore the field, allow a multipole expansion. As an example, we can derive from the vector potential in Eq. 5.23 and 5.24 the azimuthal component as follows:

$$B_\theta(r,\theta) = -\frac{\partial A_z}{\partial r} = -\frac{2\mu_0 J}{\pi} \cdot \sum_{n=1,3,5,\ldots} \left[\frac{r^{n-1}}{n\,(n-2)} \left[r_i^{2-n} - (r_i + w)^{2-n} \right] sin(n\phi_l) cos(n\theta) \right] \quad (5.30)$$

for dipoles and:

$$B_\theta(r,\theta) = -\frac{\partial A_z}{\partial r} = \frac{4\mu_0 J}{\pi} \left\{ \frac{r}{2} ln \left(\frac{r_i + w}{r} \right) cos2\theta sin2\phi_l + \right. \\ \left. + \sum_{n=6,10,14,\ldots} \left[\frac{r^{n-1}}{n\,(n-2)} \left[r_i^{2-n} - (r_i + w)^{2-n} \right] sin(n\phi_l) cos(n\theta) \right] \right\} \quad (5.31)$$

for quadrupoles. When the configuration is not simplified by its symmetries, the general multipole expansion can be expressed as:

$$B_\theta(r,\theta) = B_{ref} \sum_{n=1}^{\infty} \left(\frac{r}{r_0}\right)^{n-1} [b_n \cos n\theta + a_n \sin n\theta]$$
$$B_r(r,\theta) = B_{ref} \sum_{n=1}^{\infty} \left(\frac{r}{r_0}\right)^{n-1} [-a_n \cos n\theta + b_n \sin n\theta]$$

where r_0 is a reference radius, commonly $r_0 = \frac{r_i}{2}$. The a_n are called the *skew* coefficients, the b_n are called the *normal* coefficients. B_{ref} is a reference field, for instance the magnitude of the main field at the reference radius, so that $b_1 = 1$ for dipoles and $b_2 = 1$ for quadrupoles. For perfect dipoles and quadrupoles, all other terms of the expansion are null; in real magnets, the quality requirements ask that they remain very small, typically $|a_n|, |b_n| < 1 \cdot 10^{-4}$. These values are obtained through an accurate design and usually two diferent layers of coil, spaced by wadges, as shown in 5.19.

While these geometries are designed based on the principles that were analysed in section 6.4, and by means of some iterations on a finite element program, it is not our aim to perform a detailed magnet design. Having chosen to analyse a simple coil sector (section 5.1.1), we assumed that the quality requirements are met when the multipole coefficients' variation is smaller than 10^{-4}. In our analysis, this variation was related to two distinct phenomena: the modifications of the shape of the magnet, and the alteration of the current density distribution, both of these due to Lorentz forces.

5.6.1 Shape Variations

Field quality requirements are obtained through an accurate design of the coil's cross section geometry. Once this changes, the field itself changes. The effect of each coil area on the multipole coefficients is analysed in section 6.4; our aim was to provide a simple and efficient estimate of the loss of field quality. As a first step, we considered a coil than has not been preloaded in the azimuthal direction, and thus experiences a change in its limiting angle ϕ_l. Although in principle the deformed shaped isn't a circular sector, it can be fairly approximated as one (as it appears from the finite element analysis performed on the coil in Fig. 5.20(a)).

Therefore, we will approximate the field produced by the deformed coil (whose current density remains for now constant) as the field produced by a coil having a bore radius:

$$\widetilde{r_i} = r_i + u\left(r_i, \frac{\phi_l}{2}\right)$$

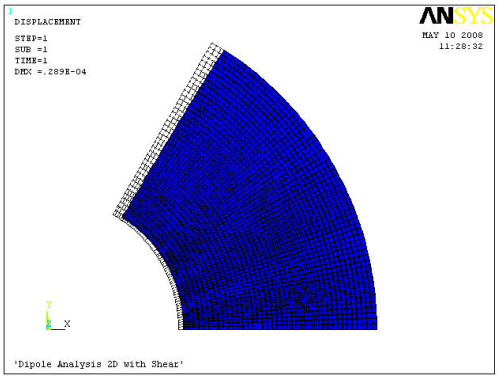

(a) A deformed coil sector.

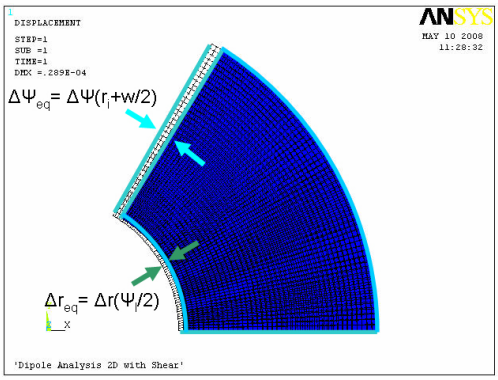

(b) Variations in geometry.

Figure 5.20: Approximations of a deformed coil

and a limiting angle:

$$\widetilde{\phi_l} = \phi_l + \frac{v\left(r_i + \frac{w}{2}, \phi_l\right)}{r_i + \frac{w}{2}}.$$

At this point, we proceed evaluating the multipole coefficients for the two configurations: the difference between the two geometries, as anticipated above, will be compared to 10^{-4}. Dealing with dipoles first, and then quadrupoles, we can use for instance the azimuthal field expression and extract its multipole coefficients:

$$B_\theta(r,\theta) = -\frac{2\mu_0 J}{\pi} \sum_{n=1,3,5,\ldots} \left[\frac{r^{n-1}}{n\,(n-2)} \left[r_i^{2-n} - (r_i + w)^{2-n} \right] \sin n\phi_l \cos n\theta \right] = \\ = B_{ref} \sum_{n=1,3,5,\ldots} \left(\frac{r}{r_0} \right)^{n-1} b_n \cos n\theta \quad (5.32)$$

(as shown in section 5.3.1, no skew multipoles appear in the presence of the symmetries in our model. Moreover, dipoles only show odd values of n and quadrupoles only have values of n that are odd multiples of 2: 2, 6, 10,...). Since the cosine terms of different order are orthogonal, this equation must be true for each value of n. From $n = 1$:

$$B_{ref} = -w \cdot \sin \phi_l \quad (5.33)$$

and then, for $n \neq 1$:

$$b_n = \frac{\left[(r_i + w)^{2-n} - r_i^{2-n} \right]}{n\,(n-2)} \frac{\left(\frac{r_i}{2} \right)^{n-1}}{B_{ref}} \sin\left(n\phi_l\right). \quad (5.34)$$

For quadrupoles we find:

$$B_{ref} = -\frac{r_i}{4} \ln\left(\frac{r_i + w}{r_i} \right) \sin 2\phi_l \quad (5.35)$$

and:

$$b_n = \frac{\left[(r_i + w)^{2-n} - r_i^{2-n} \right]}{n\,(n-2)} \frac{\left(\frac{r_i}{2} \right)^{n-1}}{B_{ref}} \sin\left(n\phi_l\right). \quad (5.36)$$

5.6.2 Variation of the current density distribution

Neglecting redistributions of the current density, J will be proportional to the conductor density. Therefore, the local ratio of the deformed element area divided by the original element area is:

$$\frac{\partial A}{\partial A_0} = 1 + \epsilon_r + \epsilon_\theta \quad (5.37)$$

we can write:

$$J(r,\theta) = \frac{J_0}{1 + \epsilon_r + \epsilon_\theta} \quad (5.38)$$

Unfortunately, there is no analytical expression for the associated field distribution. The problem needs to be solved by discretization: we will divide the sector into l elements along the radius, and m elements along each arc. Then, we will consider for each element a constant current density that is equal to the current density at the centre of the element (Fig. 5.21). In this case we have for dipoles:

$$B_{ref} = -\sum_{i=1}^{l}\sum_{j=1}^{m}\left[\frac{2\mu_0 J\left(r_i + \frac{w}{l}\left(i-\frac{1}{2}\right), \frac{\phi_l}{m}\left(j-\frac{1}{2}\right)\right)}{\pi}\cdot \right. \\ \left. \cdot \frac{w}{l}\left[\sin\left(\frac{\phi_l}{m}j\right) - \sin\left(\frac{\phi_l}{m}(j-1)\right)\right]\right] \tag{5.39}$$

and:

$$b_n = -\frac{1}{B_{ref}}\left(\frac{r_i}{2}\right)^{n-1}\sum_{i=1}^{l}\sum_{j=1}^{m}\left[\frac{2\mu_0 J\left(r_i + \frac{w}{l}\left(i-\frac{1}{2}\right), \frac{\phi_l}{m}\left(j-\frac{1}{2}\right)\right)}{\pi}\frac{1}{n(n-2)}\cdot \right. \\ \left. \cdot\left[\left[r_i + \frac{w}{l}(i-1)\right]^{2-n} - \left(r_i + \frac{w}{l}i\right)^{2-n}\right]\cdot\left[\sin\left(\frac{n\phi_l}{m}j\right) - \sin\left(\frac{n\phi_l}{m}(j-1)\right)\right]\right]. \tag{5.40}$$

For quadrupoles we find:

$$B_{ref} = -\sum_{i=1}^{l}\sum_{j=1}^{m}\left[\frac{4\mu_0 J\left(r_i + \frac{w}{l}\left(i-\frac{1}{2}\right), \frac{\phi_l}{m}\left(j-\frac{1}{2}\right)\right)}{\pi}\frac{r_i}{4}\ln\left(\frac{r_i + \frac{w}{l}i}{r_i + \frac{w}{l}(i-1)}\right)\right. \\ \left.\left[\sin\left(\frac{2\phi_l}{m}j\right) - \sin\left(\frac{2\phi_l}{m}(j-1)\right)\right]\right] \tag{5.41}$$

and:

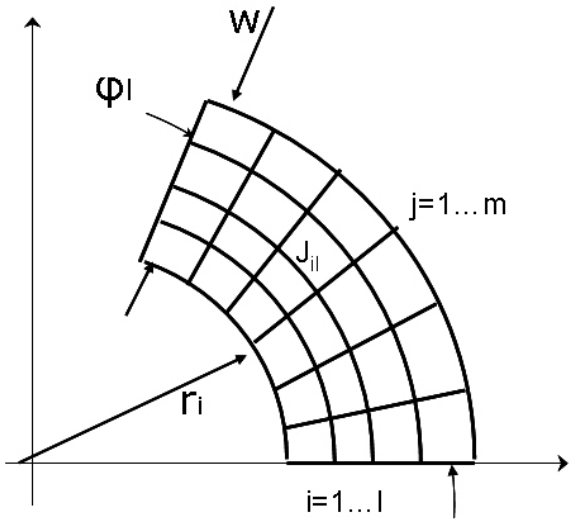

Figure 5.21: Discretization of the coil cross–section.

$$b_n = -\frac{1}{B_{ref}} \left(\frac{r_i}{2}\right)^{n-1} \sum_{i=1}^{l} \sum_{j=1}^{m} \left[\frac{4\mu_0 J \left(r_i + \frac{w}{l}\left(i - \frac{1}{2}\right), \frac{\phi_l}{m}\left(j - \frac{1}{2}\right)\right)}{\pi} \frac{1}{n(n-2)} \right.$$
$$\left. \left[\left[r_i + \frac{w}{l}(i-1) \right]^{2-n} - \left(r_i + \frac{w}{l} i \right)^{2-n} \right] \cdot \left[\sin\left(\frac{n\phi_l}{m} j\right) - \sin\left(\frac{n\phi_l}{m}(j-1)\right) \right] \right]. \tag{5.42}$$

Chapter 6

Results

Several Nb_3Sn pilot magnets, with fields as high as 16 T, have been built and tested, paving the way for future attempts at fields approaching 20 T. By means of the analytical model developed in the previous chapter, we shall address in this chapter how far the engineering of high field magnets can be pushed, investigating its limits. We shall address the relations between field, gradient, coil size, bore diameter, conductor properties, stress and field quality.

6.1 Field intensity in dipoles

6.1.1 Coil geometry

The computations were iterated for different inner radii and different coil widths, evaluating the critical field for dipoles, the critical gradient for quadrupoles, and the maximum stress obtained by each configuration. Beginning with dipoles, apertures of $r_i = 0\,mm$, $r_i = 10\,mm$, $r_i = 21.5\,mm$ and $r_i = 30\,mm$ were analysed, with coil widths between $5\,mm$ and $300\,mm$.

The critical field B_c at short–sample is plotted in Fig. 6.1 for all four different coil widths. As already noted in [14] for $\cos\theta$ dipoles, the maximum field is independent of the bore diameter: the critical field is determined solely by the coil width. We note also that at $4.2\,K$ a $10\,mm$ width is sufficient to generate almost a $10\,T$ field, while $45\,mm$ are needed for a $15\,T$ field, and $200\,mm$ for a $20\,T$ field.

Such increase in the amount of conductor is highlighted in Fig. 6.2, where the coil width is replaced by the coil area, a better indicator of the total cost. We note that increasing the critical field from $15\,T$ to $20\,T$ requires 20 times more conductor, casting doubts on its feasibility on a large scale.

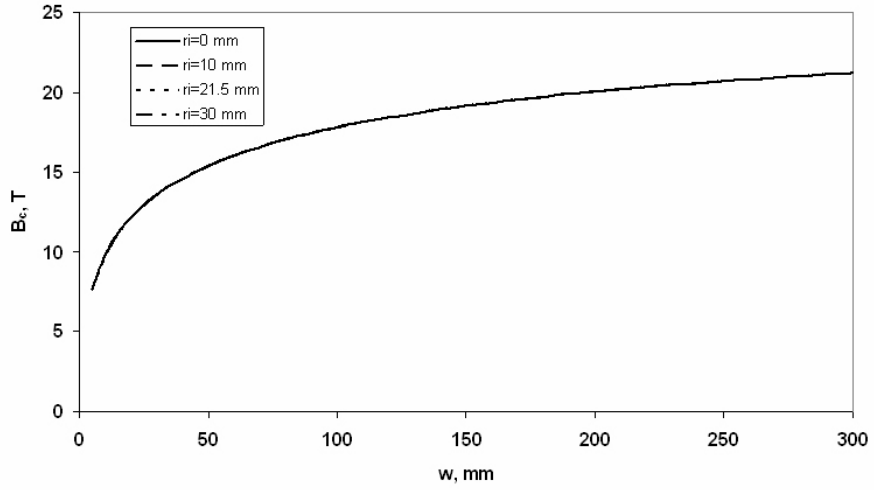

Figure 6.1: Critical field of Nb_3Sn dipole magnets at short sample vs Coil width.

We aim now at analyzing how stresses depend on the coil aperture, on the width and on the field intensity. Conventionally, it is the azimuthal stress that is taken as a reference for the stress in the coil. In analogy to what was done in [14], we can plot the maximum azimuthal Lorentz stress as a function of the critical field (Fig. 6.3) and of the coil width (Fig. 6.4). The trends are similar to those plotted in [14] for coils with $\cos\theta$ current density distribution: the zero bore solution is a monotonic increasing function both of the field and of the width; it is also the minimum for any bore diameter at that field. For bore diameters greater than zero and up to some field value, the maximum stress decreases as the critical field increases. This can be explained as follows: as we noted above (Fig. 6.2), for small widths the coil is much more efficient than for larger widths, and increasing the thickness doesn't produce a corresponding increase in the field and therefore in the Lorentz force.

We should note that for small widths the azimuthal stress σ_θ prevails over the radial stress σ_r, as the former results from an integral along the angle, while the latter requires an integration through the thickness of the coil. Thus, as field and coil thickness increase, the radial stress tends to prevail over the azimuthal stress. In Figs. 6.5 and 6.6 both the azimuthal and the radial stresses are shown as a function of B_c. We note that for null apertures, the radial stress is always larger than the azimuthal, with a difference of approximately 30%. For apertures greater than 0, the crossing point of the azimuthal stress with the radial stress gets larger both in stress

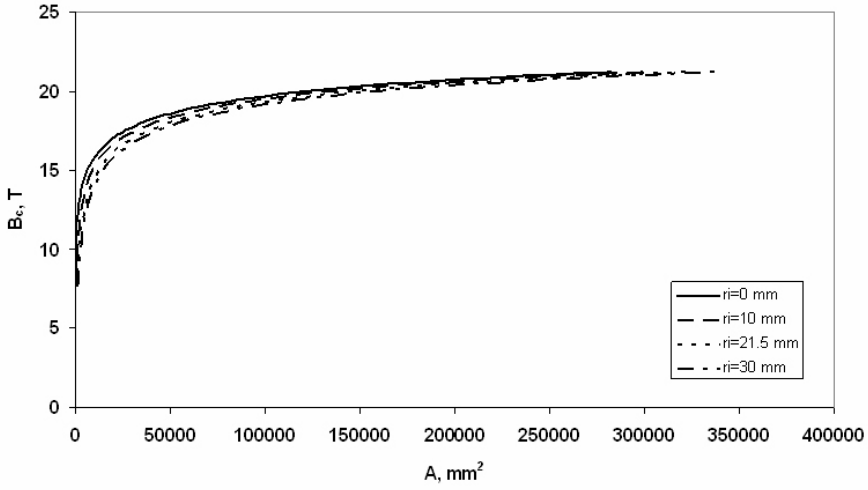

Figure 6.2: Critical field of Nb_3Sn dipole magnets at short sample vs Coil area.

and B_c values for larger apertures.

Two main consequences can be drawn from these plots. First, should we persevere using the highest principal stress as the equivalent stress for magnets, the plots should be updated with the radial stresses for all the cases in which the azimuthal stress is not the greatest. Secondly, we should devise an experiment to acquire more information over the most appropriate equivalent stress, since we are no longer looking at uniaxial stress tensors. Returning to the former issue, we can update the plots substituting the highest of the stresses in place of the azimuthal stress (Fig. 6.7 and 6.8).

The following conclusions can be drawn:

- The radial stress is negligible for small coil widths, and exceeds the azimuthal stresses at high fields and large thicknesses.
- The $0\,mm$ solution is still a minimum for all the magnets with the same critical field.
- Improvements in magnet performance with increasing coil thickness become negligible when the coil area is already high.
- A $20\,T$ dipole with a $43\,mm$ bore requires a coil that is $200\,mm$ thick. Radial stress reaches $170\,MPa$ and azimuthal stress $133\,MPa$.
- An $18\,T$ dipole with a $43\,mm$ bore requires a coil that is $105\,mm$ thick. Radial stress reaches $153\,MPa$ and azimuthal stress $126\,MPa$.

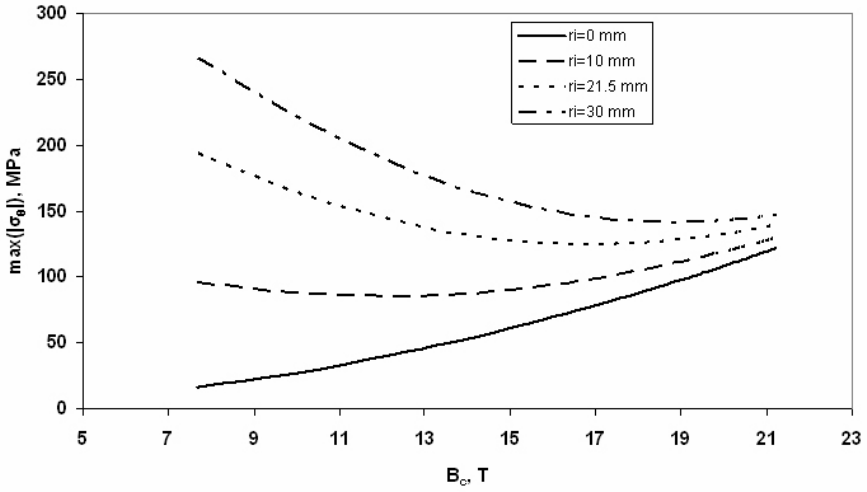

Figure 6.3: Maximum azimuthal Lorentz stress vs Critical Field.

- A $10\,mm$ thick coil is sufficient to generate a $9.8\,T$ field. The coil area with a $43\,mm$ bore increases by a factor of 30 as the field increases from $10\,T$ to $18\,T$.
- As noted in [14], at very high fields the effect of the bore diameter on the overall amount of conductor, the peak stress, and the stored energy is minor.

6.1.2 Stress containment

Uniaxial experiments [1] showed that transport properties deteriorate when the stress exceeds $150\,MPa$. Some rough observations can be carried out neglecting multiaxiality (addressed in 6.3) and comparing the experimental stress with the highest principal stress in the coil. Then, we note that the $150\,MPa$ limit is reached by the $43\,mm$ bore coil at a field of approximately $17.5\,T$. Supposing we do not allow any permanent degradation on the coil (taking place when $\sigma > 150\,MPa$), the following observation can be made: while coil performance is proportional to the current density j, the stresses are proportional to j^2. Consequently, a decrease in the current density should limit the maximum stress more than it reduces the maximum field. For each equivalent stress which is higher than $150\,MPa$, we could then limit the current density to the value $j' = j_c\sqrt{\frac{\sigma_{max}}{150}}$ (Figs. 6.9 and 6.10).

We notice that a smaller increase in the magnet performance can be obtained while still keeping the maximum principal stress below the $150\,MPa$

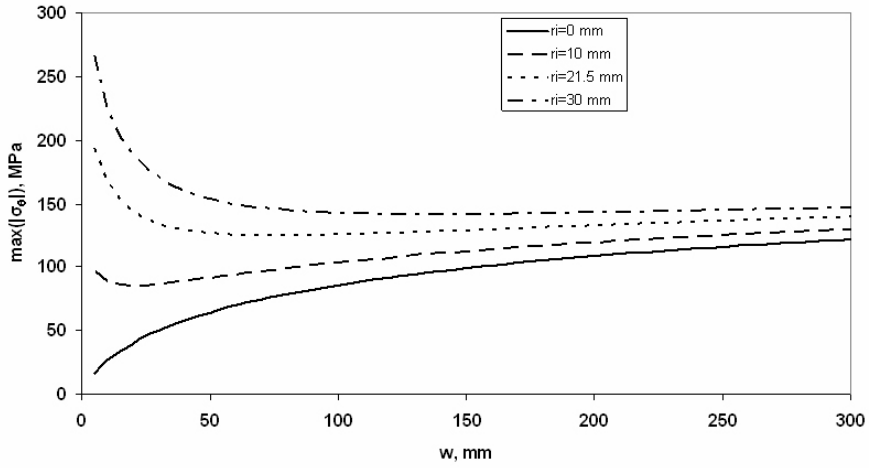

Figure 6.4: Maximum azimuthal Lorentz stress vs Coil thickness.

limit, at the cost of a larger increase in the amount of superconducting cable. On the whole, increasing the amount of the conductor becomes a very costly way to pursue higher fields when the field is already high (Fig. 6.1 and Fig. 6.2). There is, however, another area where improvement can be achieved. We note that the azimuthal stress and the radial stress have similar distributions (Fig. 6.11), and therefore an equivalent stress related to the difference between the principal stresses could result significantly lower, paving the way for graded coils, shown in [14] to reduce the amount of conductor needed while increasing the maximum stress.

6.1.3 Conductor properties

A considerable amount of efforts is currently being spent to improve Nb_3Sn cable transport properties, as a better conductor can be much more effective than a larger amount of conductor at very high fields (Fig. 6.2). It holds some interest then to study how a better conductor can affect the magnet performance. Considering a dipole coil with a $43\,mm$ bore diameter and a $30\,mm$ thick coil, we studied the effect of scaling up the Nb_3Sn critical surface on the j axis, while leaving the B axis unmodified. To represent the cable performance, we used its critical engineering current density at $12\,T$: Fig. 6.12 shows the critical field dependence on the cable performance, while Fig. 6.13 shows the maximum principal stress.

From Fig. 6.12 we note that at high fields the gain in magnet performance becomes smaller, recalling the dependence on the coil width. In this case,

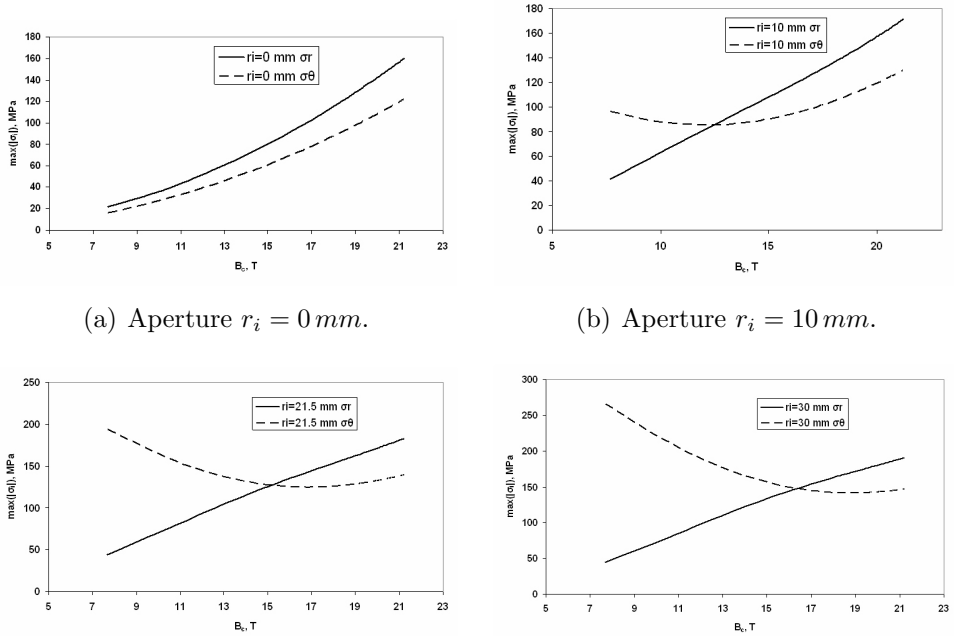

(a) Aperture $r_i = 0\,mm$.

(b) Aperture $r_i = 10\,mm$.

(c) Aperture $r_i = 21.5\,mm$.

(d) Aperture $r_i = 30\,mm$.

Figure 6.5: Radial and azimuthal stress for different geometries vs field.

the asymptotic behavior is due to the fact that, as the coil field gets closer to the critical field of the superconductor itself, the quench happens at higher fields, where the critical surface is barely affected by the improvement in the cable performance.

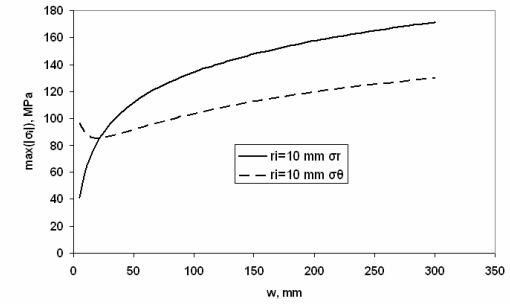

(a) Aperture $r_i = 10\,mm$.

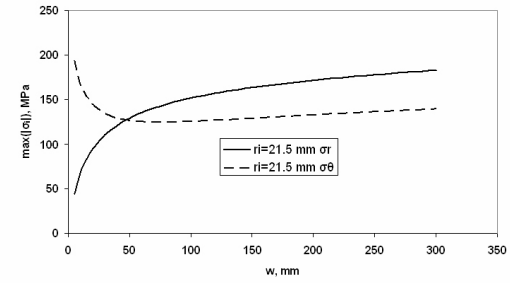

(b) Aperture $r_i = 21.5\,mm$.

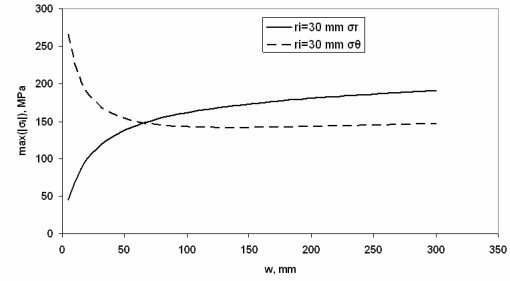

(c) Aperture $r_i = 30\,mm$.

Figure 6.6: Radial and azimuthal stresses for different geometries vs coil width.

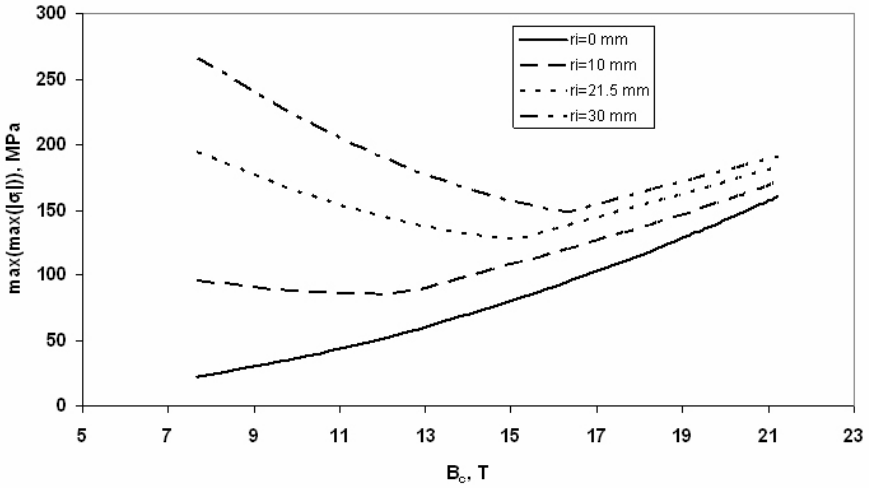

Figure 6.7: Maximum Lorentz stress vs Critical Field.

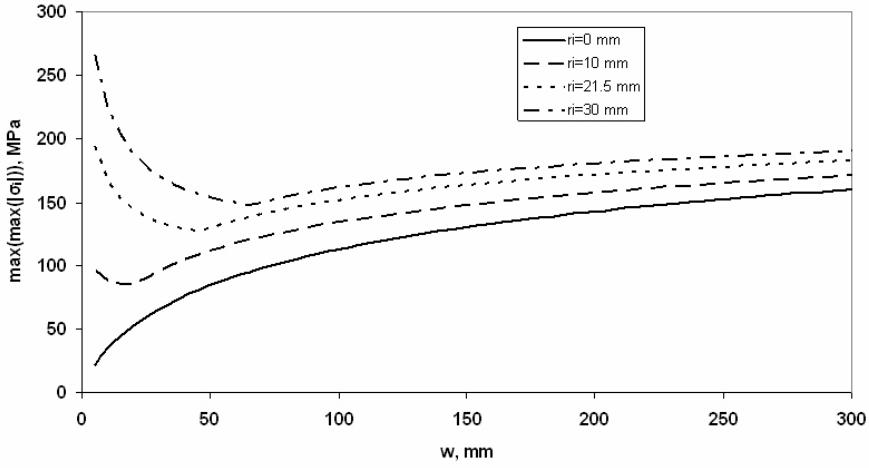

Figure 6.8: Maximum Lorentz stress vs Coil thickness.

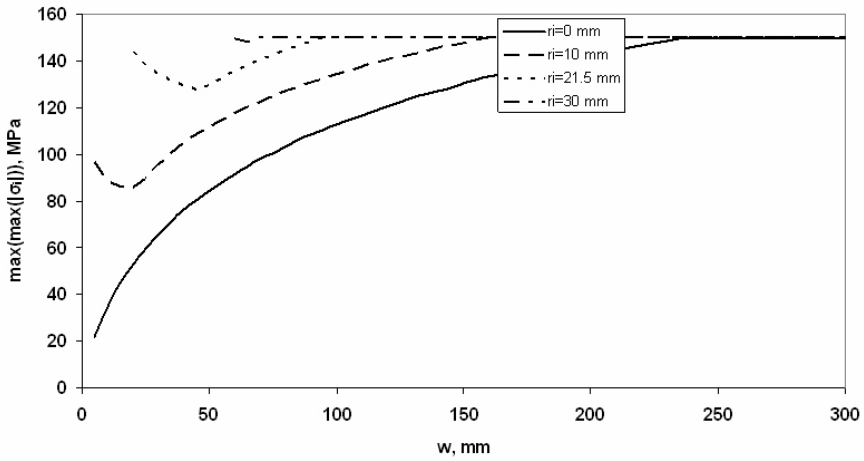

Figure 6.9: Keeping the stress below the 150 MPa limit.

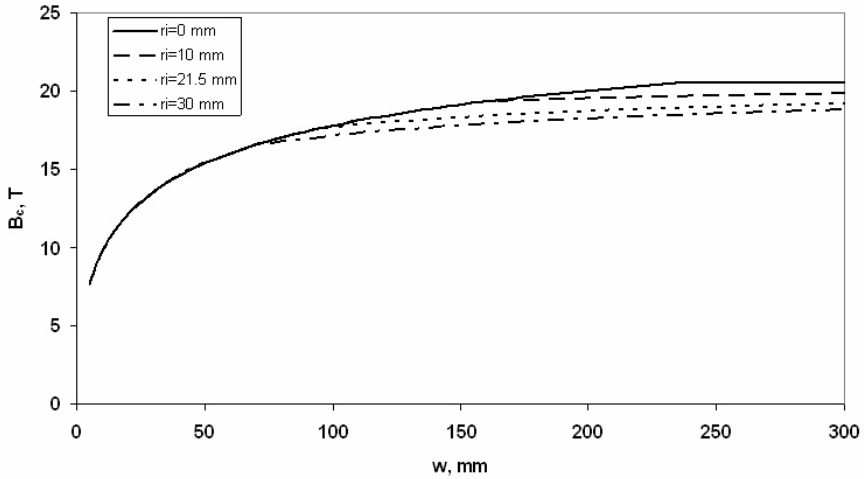

Figure 6.10: Effects on the maximum field.

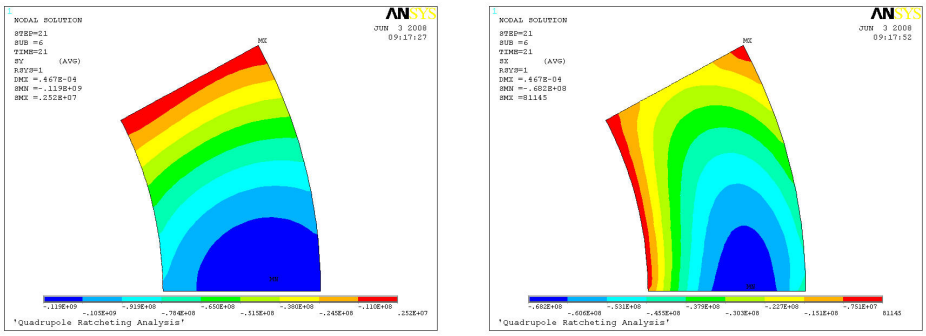

(a) Azimuthal stress. (b) Radial stress.

Figure 6.11: Radial and azimuthal stress distribution.

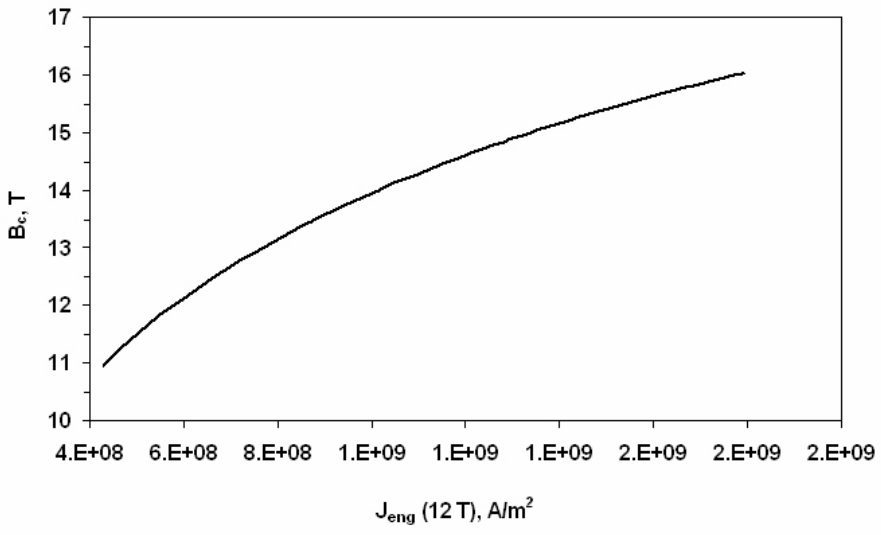

Figure 6.12: Critical field dependence on cable performance.

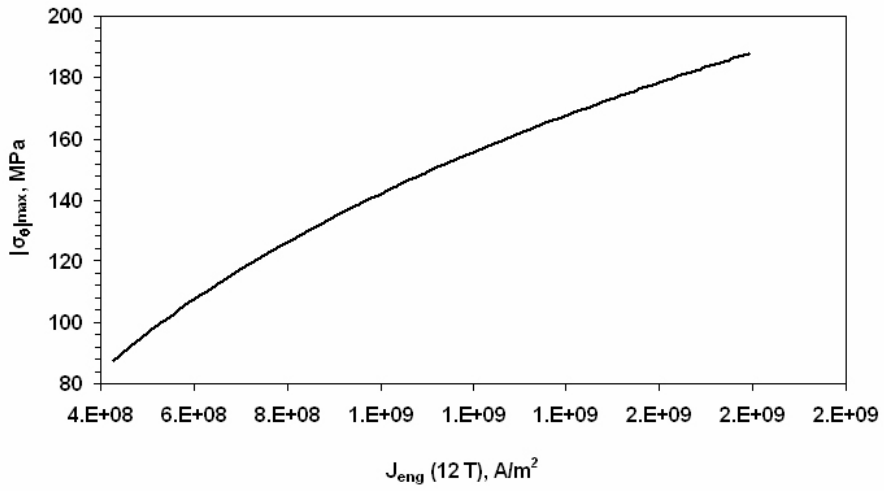

Figure 6.13: Maximum principal stress dependence on cable performance.

6.2 Quadrupoles

6.2.1 Coil geometry

Quadrupole apertures were chosen between $r_i = 10\,mm$ and $r_i = 60\,mm$, with coil widths w between $5\,mm$ and the value $w = 2r_i$. The critical gradient G_c at short–sample is plotted in Fig. 6.14 for all four different coil widths. As the critical gradient takes place when the field in the coil reaches its critical value, larger bores tend to have smaller gradients; in [19] it is noted though that larger bores reach a higher value of the product $G_c r_i$, suggesting that quadrupoles with very small apertures do not exploit well the potential of superconducting material. As observed in [19], the critical gradient at some points decreases with w, due to the asymptotic behaviors $G = j\gamma \approx j\log(w)$ and $B_{max} = j\beta \approx jw\log(w)$. When adding cable, so increasing w, we mainly increase the peak field, and we only marginally increase the gradient, thus reducing the critical gradient.

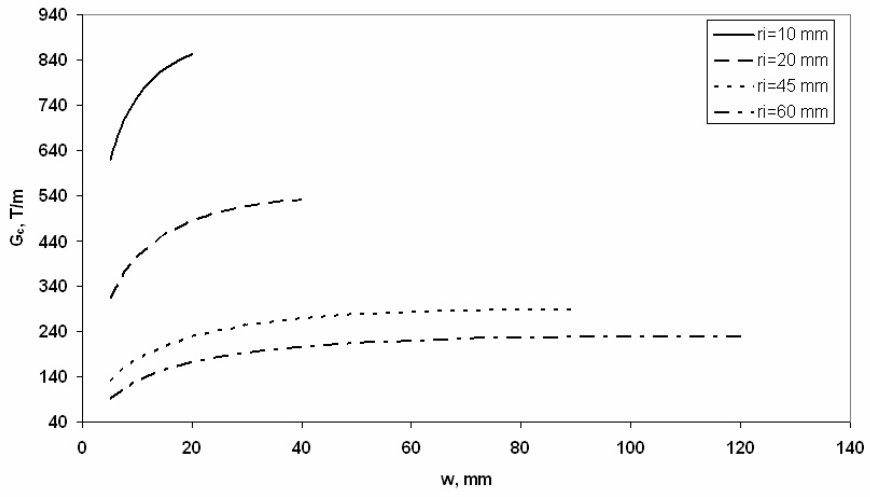

Figure 6.14: Critical gradient of Nb_3Sn quadrupole magnets at short sample vs Coil width.

Still, smaller bores are a dominant choice to obtain higher gradients, as highlighted by Fig. 6.15.

We aim now at analyzing how stresses depend on the coil aperture, on the width and on the field intensity. Just like dipoles, it is conventionally the azimuthal stress that is taken as a reference for the stress in the coil ([13]). Along the same lines, we can plot the maximum azimuthal Lorentz stress as a function of the critical gradient (Fig. 6.16) and of the coil width (Fig.

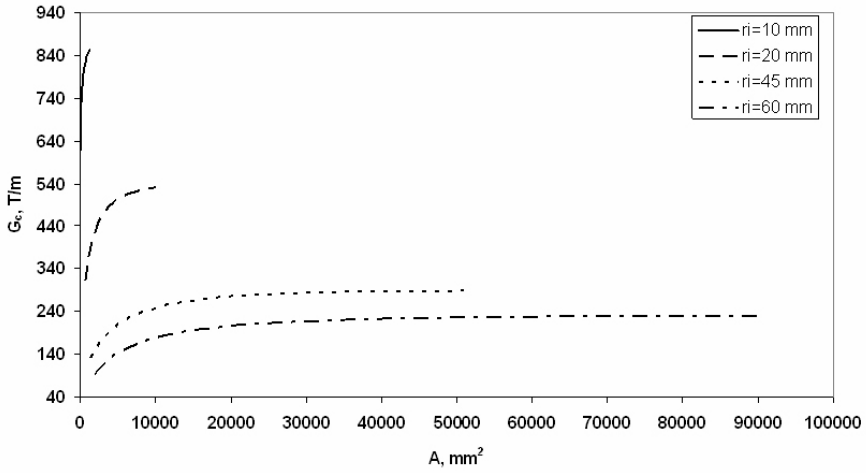

Figure 6.15: Critical gradient of Nb_3Sn quadrupole magnets at short sample vs Coil area.

6.17). The trends are similar to those plotted in [13]. The stress increases for larger apertures, and in the 60 mm case can exceed 150 MPa. The stress increases monotonically with the gradient and the width for small radii, while it shows a more convoluted behavior for larger radii. Fig. 6.16 shows that for large radii and fields the stress tends to increase while the gradient decreases. This is directly connected to the observations made above: as the field grows asymptotically more than the gradient, so do the Lorentz forces, reaching the condition where the gradient decreases while the maximum azimuthal stress increases, accounting for the "'U–turn"' in Fig. 6.16.

We should note that, similarly to dipoles, for small widths the azimuthal stress σ_θ prevails over the radial stress σ_r, as the former results from an integral along the angle, while the latter requires an integration through the thickness of the coil. Thus, as field and coil thickness increase, the radial stress tends to prevail over the azimuthal stress. In Fig. 6.18 and 6.19 both the azimuthal and the radial stresses are shown.

Two main consequences are similar to those drawn for dipoles. First, should we persevere using the highest principal stress as the equivalent stress for magnets, the plots should be updated with the radial stresses for all the cases in which the azimuthal stress is not the greatest. Secondly, we should devise an experiment to acquire more information over the most appropriate equivalent stress. Returning to the former issue, we can update the plots substituting the highest of the stresses to the azimuthal stress (Fig. 6.20 and 6.21).

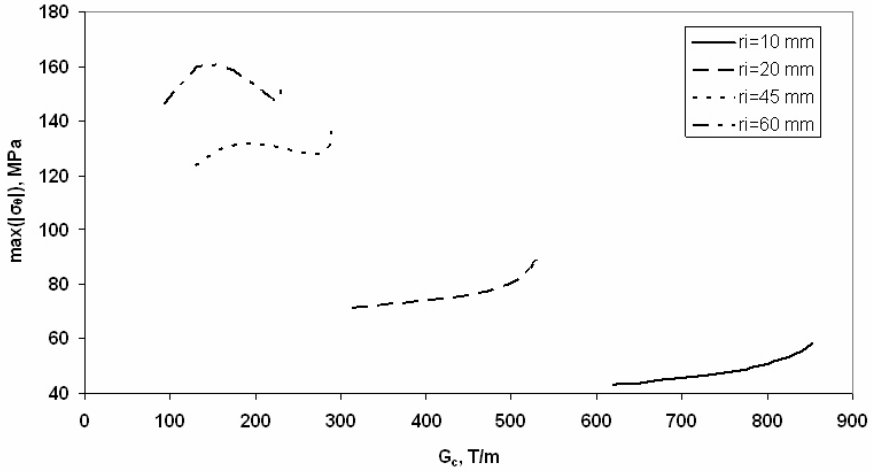

Figure 6.16: Maximum azimuthal Lorentz stress vs Gradient.

The following conclusions can be drawn:

- The radial stress is negligible for small coil widths, and exceeds the azimuthal stresses at high fields and large thicknesses.
- The $150\,MPa$ limit is only exceeded for very large apertures ($r_i > 45\,mm$), and stress increases again as the bore becomes larger.
- As noted in [13], at large apertures the peak stress does not increase monotonically with G_c: a maximum is found for a given G_c, after having reached that point the stress decreases as G_c increases (since w increases faster than G_c).
- Fig. **??** suggests that the maximum radial stress $|\sigma_r|_{MAX}$ has a strong dependence on the coil thickness, and a very weak dependence on the bore radius r_i and the critical gradient G_c. All the radial stresses tend to describe a single curve.
- Fig. 6.20 suggests that, for optimum performance, a quadrupole should be designed in order to have $|\sigma_\theta|_{MAX} = |\sigma_r|_{MAX}$. We note indeed that increasing the width as long as $|\sigma_\theta|_{MAX} > |\sigma_r|_{MAX}$ has a the effect of increasing the critical gradient while not doing so on the maximum stress. Once the radial stress exceeds the azimuthal stress, the maximum stress increases much more than the azimuthal, making it less profitable to enlarge the thickness of the coil.

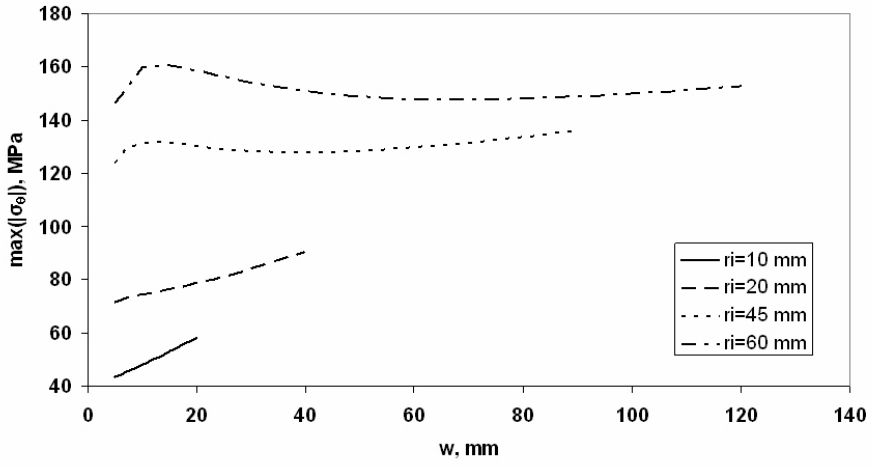

Figure 6.17: Maximum azimuthal Lorentz stress vs Coil thickness.

- Should the equibiaxial stress be considered a favourable condition by our model of equivalent stress, it would be an extra argument for designing at the intersection of the two maximum stress moduli: the radial and the azimuthal stress distribution are quite similar (Fig. 6.11).

6.2.2 Conductor properties

Similarly to what was done for dipoles, we can plot the dependence of the critical gradient and the maximum stress on the cable properties. The four geometries analysed were: $r_i = 10\,mm$ $w = 10\,mm$, $r_i = 20\,mm$ $w = 20\,mm$, $r_i = 45\,mm$ $w = 40\,mm$, $r_i = 60\,mm$ $w = 60\,mm$. To represent the cable performance, we used its critical engineering current density at $12\,T$. Fig. 6.22 shows the critical field dependence on the cable performance, while Fig. 6.23 shows the maximum stress.

From Fig. 6.22 we note that by doubling the cable performance at $12\,T$ from $400/mm^2$ to $800/mm^2$ the increase in critical gradient is only about 20%, suggesting that quadrupoles are less affected by the increase in cable performance than dipoles.

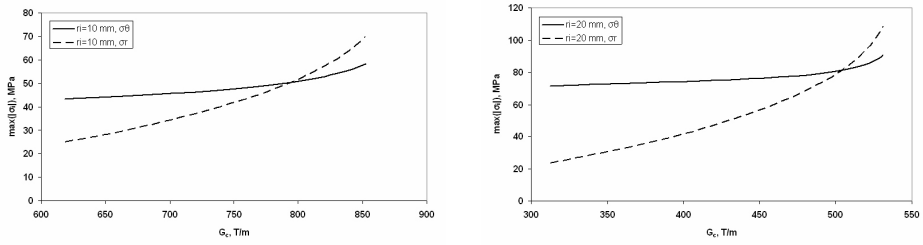

(a) Aperture $r_i = 10\,mm$.

(b) Aperture $r_i = 20\,mm$.

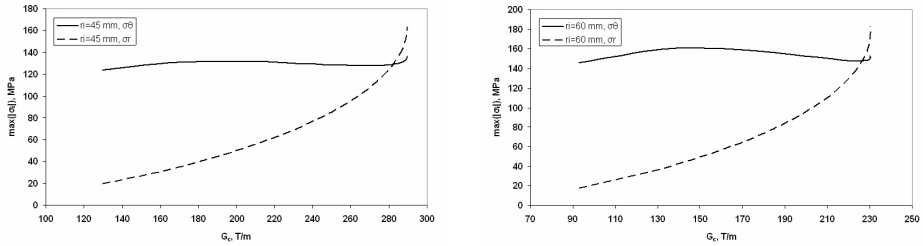

(c) Aperture $r_i = 45\,mm$.

(d) Aperture $r_i = 60\,mm$.

Figure 6.18: Radial and azimuthal stresses for different geometries vs Critical Gradient.

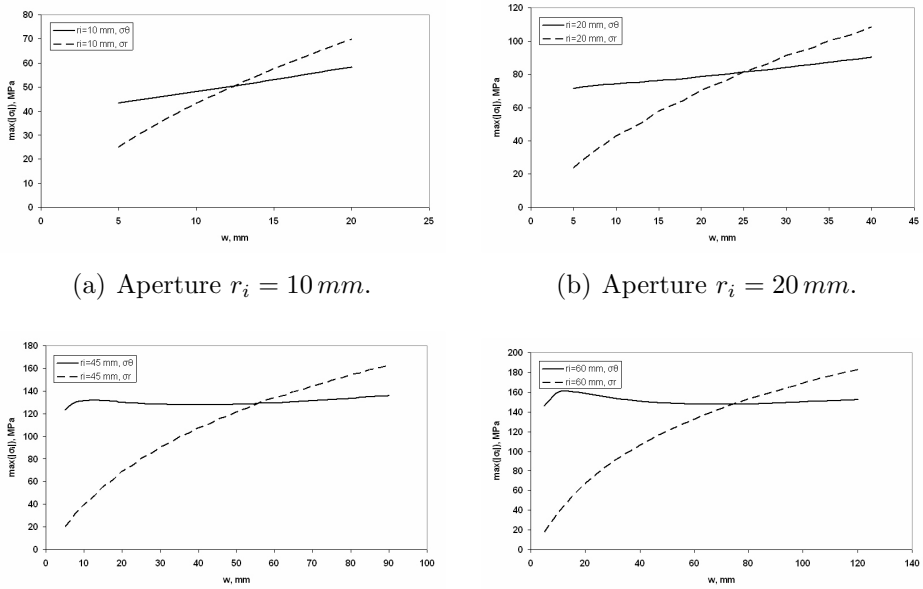

(a) Aperture $r_i = 10\,mm$. (b) Aperture $r_i = 20\,mm$.

(c) Aperture $r_i = 45\,mm$. (d) Aperture $r_i = 60\,mm$.

Figure 6.19: Radial and azimuthal stresses for different geometries vs Coil width.

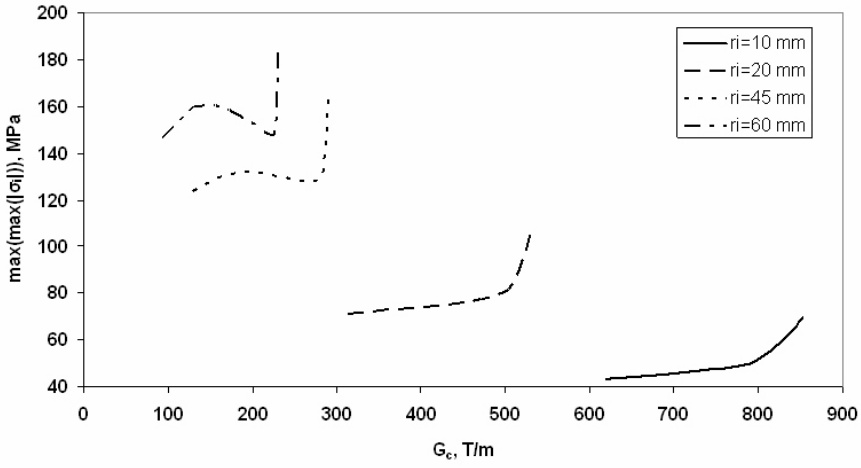

Figure 6.20: Maximum Lorentz stress vs Critical Gradient.

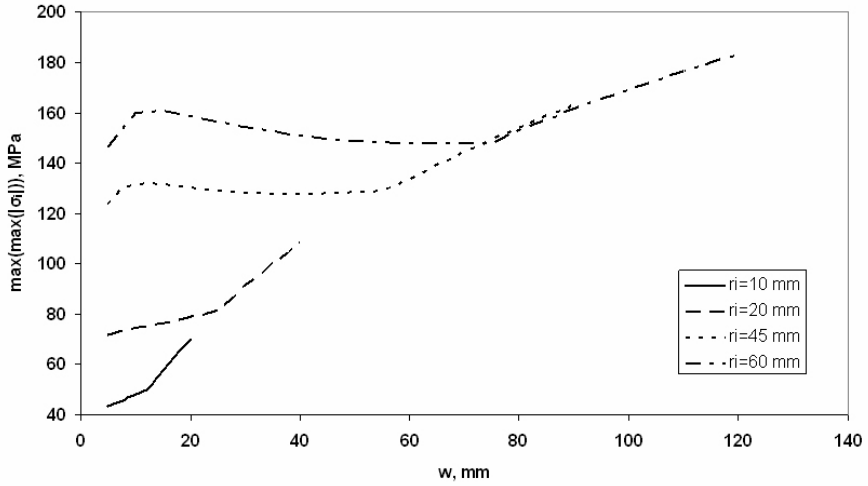

Figure 6.21: Maximum Lorentz stress vs Coil thickness.

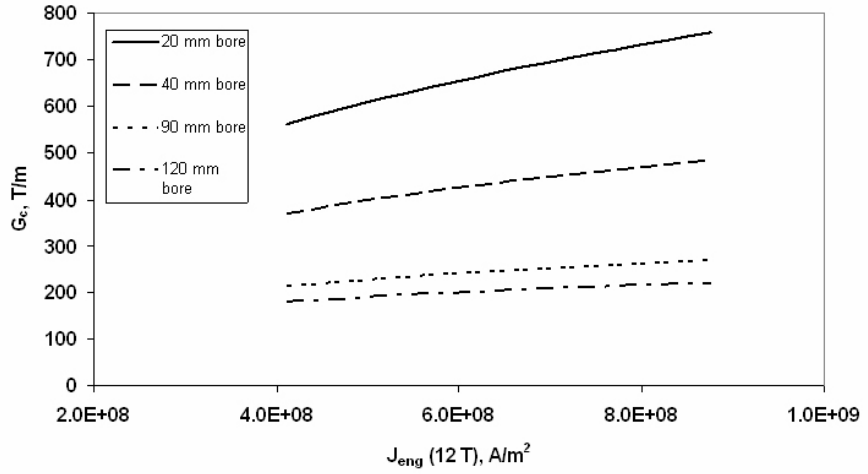

Figure 6.22: Critical gradient dependence on cable performance.

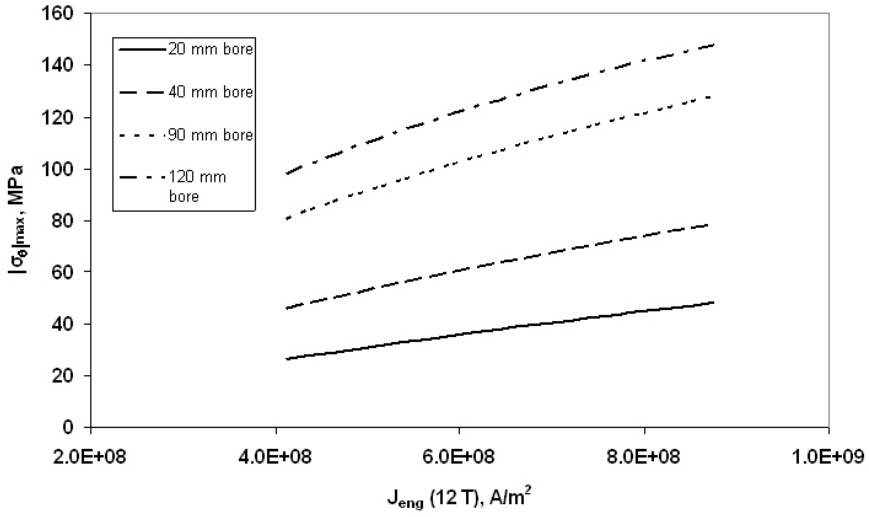

Figure 6.23: Maximum stress dependence on cable performance.

6.3 Criticality

So far the stress effect was included in the form of a mere value that must not be exceeded in the coil in order for it to perform as expected. We shall now address the interaction between magnetic field and stress in determining the quench of the coil, and the effect of multiaxiality of the stress tensor pointed out in 6.2. In order to analyse a quadrupole geometry with a strong multiaxiality, referring to Fig. 6.19(c), we considered a coil sector with $r_i = 45\,mm$ and $w = 70\,mm$. We represented the radial and the azimuthal stress distribution respectively in Figs. 6.24(a) and 6.24(b).

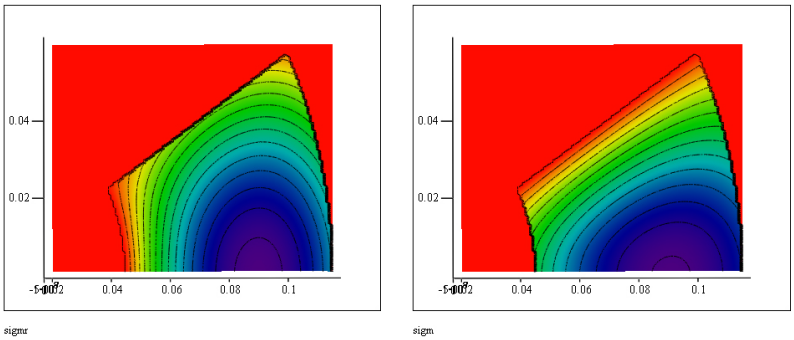

(a) Radial stress. (b) Azimuthal stress.

Figure 6.24: Stress distribution across a quadrupole coil sector.

We note that the high levels of multiaxiality (the area in which both figures are dark green, blue or violet) are located on a semi-ellipse on the bottom right part of the coil. The azimuthal stress modulus reaches high values also along the inner radius in the bottom end, where the radial stress is null or low. Similarly, the azimuthal stress modulus is null or low along the upper end of the sector, therefore excluding multiaxiality in such area. Keeping in mind these considerations, we shall proceed to consider the field modulus distribution (Fig. 6.25(a)). We note that the highest field area (red) is located along the inner radius and the left end of the upper limit of the coil, where we just noted that multiaxiality can be excluded. Based on such observations, we can state that the multiaxiality of the stress tensor can be neglected in magnet performance analysis.

We shall conclude that, when analysing the effects of the stress on the coil performance, the interaction between aximuthal and radial stress can appropriately be neglected. There is still an open question as to which of the two should be considered. In a conservative analysis, we can suppose that the

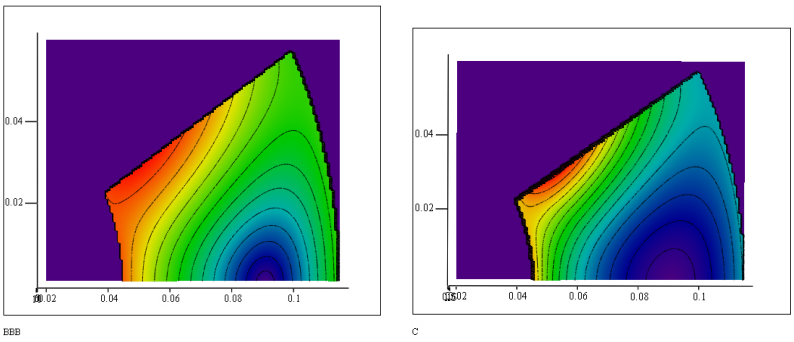

(a) Magnetic field modulus across the coil.

(b) Criticality.

Figure 6.25: Field and Criticality factor.

maximum field acts all along the left and top sides of the coil, and then consider a coil element that is subject to the maximum field and the maximum stress modulus (either radial or azimuthal but in either case a uniaxial stress tensor). The data obtained in [1] are therefore appropriate for the analysis of quadrupole magnet performance. Moving forward, we might be interested in which of the two stresses is that limiting the magnet performance. In order to do this, we can define for each coil element its critical current density, taking into account both external field and applied stress as explained in 5.2. We can define a *criticality factor* as the ratio between the current density and the local critical current density, and therefore locate the position where the quench is supposed to take place, and the dominant stress on that position. It should be noted though, that the location of the first quench can depend upon the coil geometry. For the specific geometry considered in this section, the *criticality factor* has been plotted on Fig. 6.25(b), suggesting that it is the radial stress that should be taken into consideration. We also note that the radial stress is considerably lower than the maximum radial stress, thus giving some margin on the stress when designing high field magnets with respect to the data collected in [1]

6.4 Field Quality

6.4.1 Geometry–dependence of multipole coefficients

The multipole expansion was introduced in section 5.3 It was also stated that having normalized the main coefficient to unity ($b_1 = 1$ in a dipole, $b_2 = 1$ in a quadrupole), all the remaining coefficients are usually required to be $< 10^{-4}$. Each degree of freedom in the design allows canceling one of the remaining multipoles. Although the number of multipole terms is naturally infinite, only a finite number of degrees of freedom is required in the design, and that is because the multipole series converges to 0 as $\frac{1}{n^3}$ (Fig. 5.10). The degrees of freedom are obtained by controlling the azimuthal extension of the coil, inserting wedges and adding a layer. Fig. 6.27(a) for dipoles and Fig. 6.27(b) for quadrupoles represent the multipole terms as a function of a single sector winding of azimuthal extension ϕ_l (shown in Fig. 6.26(a)). All the aforementioned concepts can be spotted in the two figures:

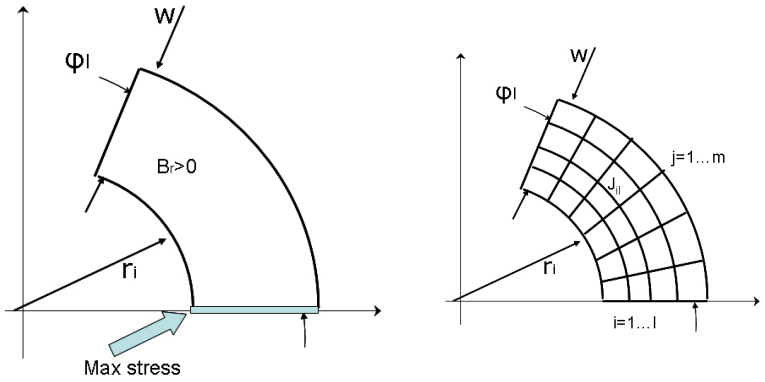

Figure 6.26: Notations.

- The dipole b_3 multipole is null when $\phi_l = \pi/3$, and the quadrupole b_6 coefficient is null if $\phi_l = \pi/3$.
- A single sector cannot cancel all the higher order multipoles when it is designed to cancel the first remaining multipole.
- Higher order multipoles converge to 0.

We also notice from Fig. 6.27(a) that b_3 decreases with the azimuthal extension: this kind of behavior suggests that the contribution to b_3 of the

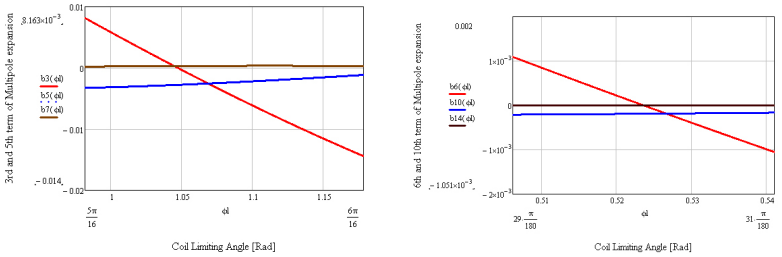

(a) Dipole terms. (b) Quadrupole terms.

Figure 6.27: Multipole terms vs Coil azimuthal extension.

portion of the coil "'close"' to $\pi/3$ is negative. In this frame of mind, we can divide a coil sector in elements (Fig. 6.26(b)), and plot the contribution of each element of the coil to the multipole coefficients b_3 and b_5. The plot will then indicate where to add coil, or where to replace the conductor with a wedge, in order to increase or decrease the amplitude of the coefficient. For example, should there be an indication that a coil design has $b_3 > 0$, the suggestion would be either to add some conductor at $\theta = \pi/3$, or to put a wedge at $\theta = 0$. Fig. 6.28 represents the contributions at three increasing radii, as a function of the azimuthal position of the coil element.

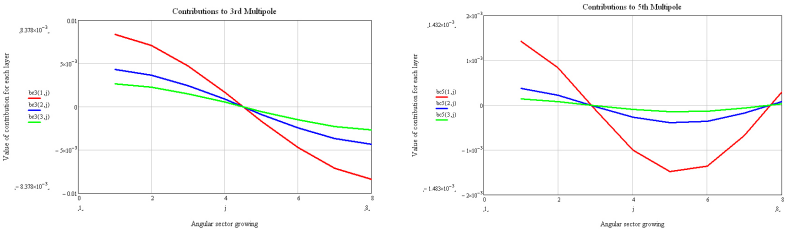

(a) b_3 dipole coefficient. (b) b_5 dipole coefficient.

Figure 6.28: Contribution of each coil element to the amplitude of the multipole coefficients.

The aforementioned design procedure does not guarantee that the quality requirements will be met by the real magnet. We will consider two different phenomena, caused by the Lorentz force, that produce a variation in the multipoles values: *variation of the coil shape* and *redistribution of the current density.*

6.4.2 Variation of the coil shape

When we analyse a coil sector with an azimuthal contraint along the mid–plane and a radial constraint along the outer radius, withouth preload (Fig. 6.29(a)) and subject to Lorentz force, we can observe a decrease in its azimuthal extension and an increase in its inner radius (Fig. 6.29(b)).

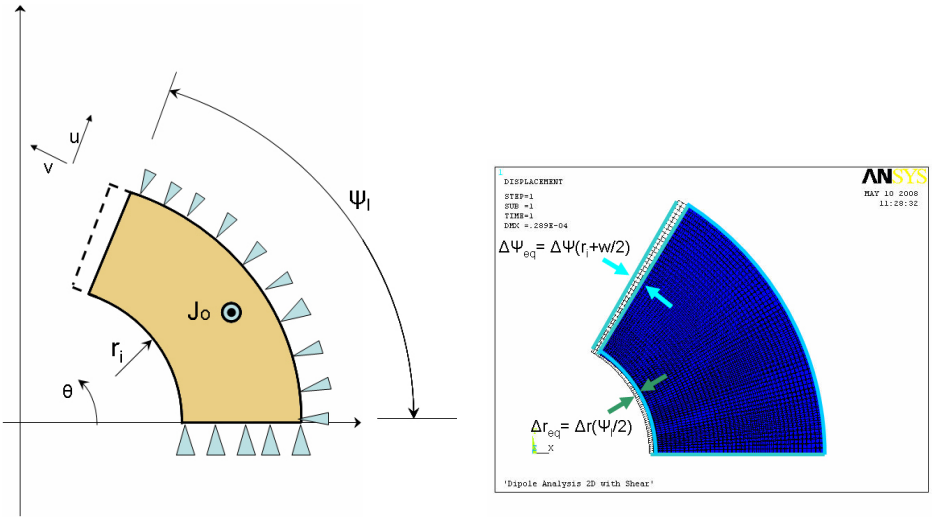

(a) Coil mechanical model. (b) Variations in geometry.

Figure 6.29: Approximations in the coil sector.

We are interested in the multipole terms variation that comes along with the modified coil shape. Such variation depends on the coil stiffness. Although Nb_3Sn has a plastic behaviour, it will be shown (7) that an appropriate amount of *spring back* allows the coil to behave linearly. Under such hypothesis, we analysed the dependence of the multipole terms' variation on the coil's Young modulus. Results are shown in Figs. 6.30 and 6.31 for a dipole ($r_i = 21.5\,mm$, $w = 20\,mm$) and a quadrupole ($r_i = 45\,mm$, $w = 40\,mm$) respectively.

Figs. 6.32(a) and 6.32(b) show, respectively for dipoles and quadrupoles, the radial displacement of the inner radius (u) and the azimuthal displacement at the upper end of the coil, in mm.

The following observations can be drawn:

- The trends are consistent with the observations made above: the Lorentz forces produce a decrease in the azimuthal extension of the coil (Fig. 6.32(a)), and therefore the negative contribution to the b_3 multipole

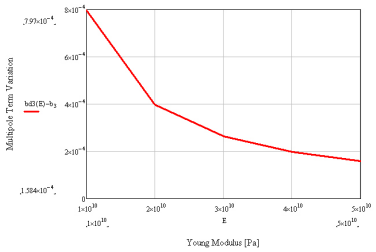

(a) b_3 dipole coefficient.

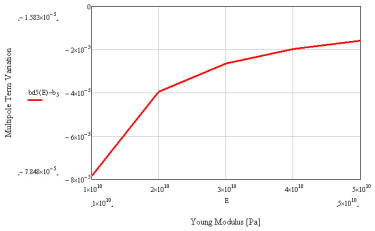

(b) b_5 dipole coefficient.

Figure 6.30: Variation of the multipole coefficients vs Young modulus.

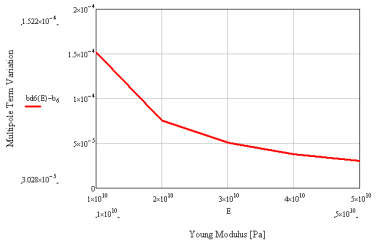

(a) b_6 quadrupole coefficient.

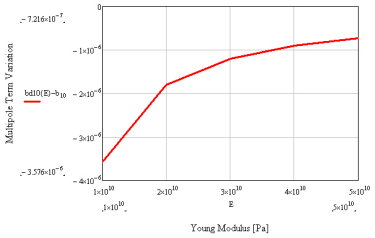

(b) b_{10} quadrupole coefficient.

Figure 6.31: Variation of the multipole coefficients vs Young modulus.

coefficient is eliminated. As a consequence, the b_3 multipole variation is positive. The same observations apply to all the other coefficients.

- In the dipole, when $E = 39\,GPa$, we learn that $\Delta b_3 \approx 2 \cdot 10^{-4}$, exceeding the 10^{-4} limit (Fig. 6.30(a)). An azimuthal preload is therefore necessary in order to prevent the coil from changing its azimuthal extension.
- In the dipole, for the same value of E, $\Delta b_5 << 10^{-4}$, confirming that higher order multipole terms are inherently smaller(Fig. 6.30(b)).
- In quadrupoles, the multipole terms are smaller, as both b_6 and b_{10} are smaller than the 10^{-4} conventional limit.

6.4.3 Redistribution of the current density

The inner surface of the deformed coil is not a cylindric portion (even though it resembles one very closely). Neglecting this, the shape variation responsible for the change in the multipole terms is the decrease of the azimuthal

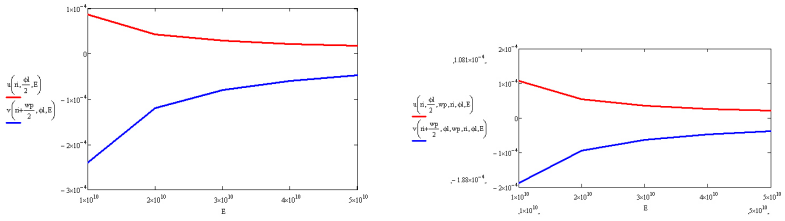

(a) Dipole coil. (b) Quadrupole coil.

Figure 6.32: Coil displacements in mm.

extension of the coil sector. This effect can be eliminated by preloading the coil; the minimum displacement of the upper end of the sector is given by the maximum displacement of the same upper end while the magnet is subject to the Lorentz force. In such condition, the multipole terms are still affected by the redistribution of the current density, that takes place as a consequence of the internal strain of the material. The same dipole and quadrupole configurations mentioned above have been analysed, and results are shown in Figs. 6.33 and 6.34 for the dipole and the quadrupole respectively.

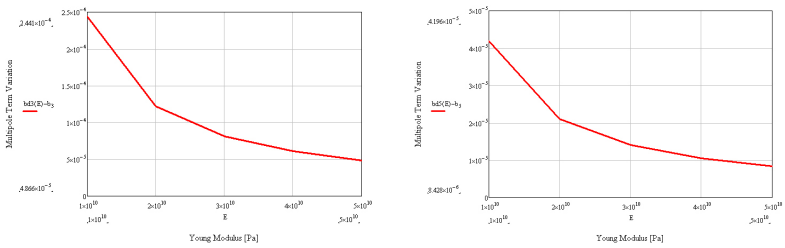

(a) b_3 dipole coefficient. (b) b_5 dipole coefficient.

Figure 6.33: Variation of the multipole coefficients vs Young modulus.

The following observations can be made:

- The current density redistribution has the effect of increasing the value of b_3 (Fig. 6.33(a)); this can be explained considering that the Lorentz force tends to "'pack up"' more conductor arount the mid plane, therefore amplifying its contribution to the multipole coefficient. The same observations apply to the other cases.
- The effects of current density redistribution are generally between 20%

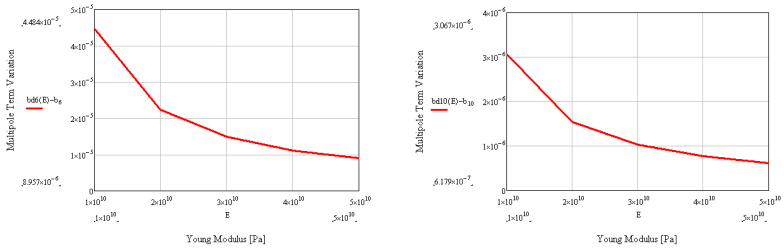

(a) b_6 quadrupole coefficient. (b) b_{10} quadrupole coefficient.

Figure 6.34: Variation of the multipole coefficients vs Young modulus.

and 50% of those due to shape variation, and below 10^{-4}. A considerable improvement can then be obtained by means of a preload.

- The redistribution of the current density and the change of the azimuthal extension both increase the value of the b_3 coefficient.
- The redistribution of the current density increases the value of the b_5 coefficient, while the change of the azimuthal extension decreases it. Therefore, a coil that is not preloaded has a better value of b_5.
- The same observations apply to quadrupoles.

Finally, we can plot the contribution to the variation of b_3 of each coil part (Fig. 6.35). The contribution of different coil parts, as a function of the azimuthal position, for three different radii is represented.

6.4.4 Conclusions

- The magnet can be designed in its ideal configuration based on the contribution of each coil element to the multipole terms.
- The Lorentz force produces in dipoles without preload a variation of b_3, which is greater than the 10^{-4} limit; the variation is reduced below the limit with a sufficient preload (Fig. 6.36).
- Higher order multipole terms are not subject to variation of their value exceeding 10^{-4} when operating in linear conditions at the critical field.
- The effect of redistribution of the current density is generally smaller than the change of coil shape, and its magnitude is acceptable.

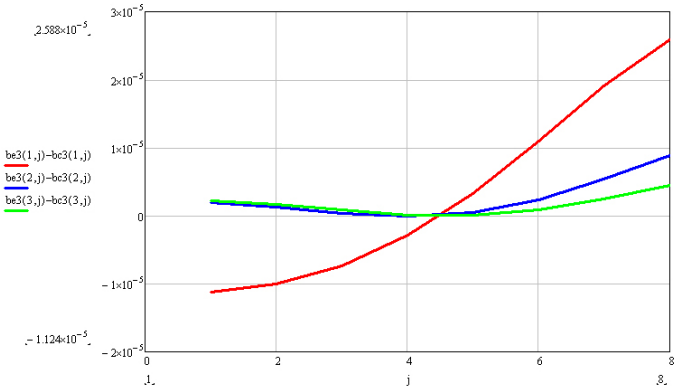

Figure 6.35: Contribution to Δb_3 of coil elements as a function of the azimuthal position, at 3 increasing radii. The x axis is numbered proportionally to the angle of the element.

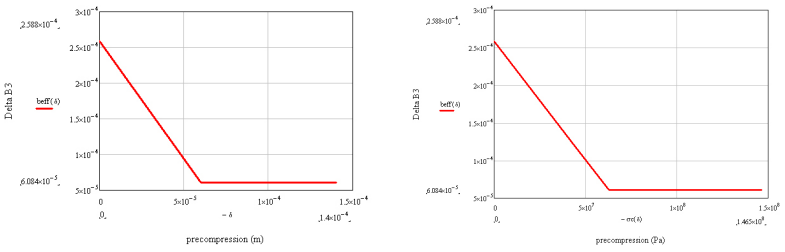

(a) (b)

Figure 6.36: Δb_3 vs Precompression.

Chapter 7

Ratcheting

7.1 Introduction

In past years, a significant effort has been devoted by the scientific community towards developing finite element models to predict the behaviour of high field Nb_3Sn superconuducting magnets. One of the main objectives was the study of the quenching processes in the magnets. The transition from the superconducting state to the normal resistive state occurs either because the superconductor reaches its short sample limit, or because of transient disturbances like flux jumping or mechanical motions, which locally heat the cable abouve the quench temperature [22], [23]. Mechanical disturbances are driven by large Lorentz forces acting on the winding during excitation. Under such forces, a superconducting cable may move with respect to the surrounding structure, at the same time producing cracks in the epoxy impregnation. Both events result in a release of energy that may trigger a quench [24].

Another phenomenon typical to superconducting magnets is training, i.e. the progressive improvement of quench current after repeated quenching. This process can be explained by assuming that, after a quench induced by a mechanical motion, the coil is partially locked by friction in a new and more secure stress condition. On subsequent current ramps, this condition allows the coil to withstand higher levels of Lorentz forces. Following subsequent training ramps, as the current reaches higher levels and then goes back to zero, the rods supporting axially the coils show increasing residual strain. This second phenomenon is called *ratcheting*. In [21], the ratcheting was related to the friction between the components, which, after a quench, locks the coil in a new position, and prevents it from returning to its original location.

In [21], a 3D finite element model was implemented with the goal of

contributing to the interpretation of magnet performances. The subscale quadrupole magnet SQ02 (Fig. 7.1) was modeled through a 3D finite element model including friction, cycling the Lorentz force. With a linear material model, the released mechanical energy was correlated to the level of deformation, and to the increase of temperature (by means of a bidimensional adiabatic finite element model). Using a best fit of sperimental data for the friction factor, the study reproduced the training curve of the SQ02 magnet.

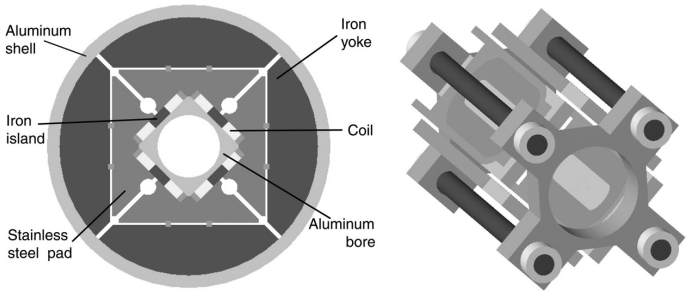

Figure 7.1: The subscale quadrupole magnet SQ02.

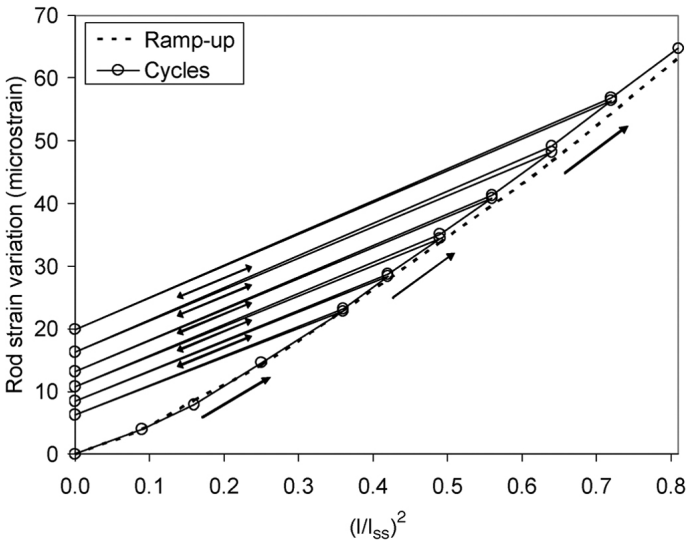

Figure 7.2: Rod Strain during training.

The study achieves a good estimate of the training curve, but modeling the coil as a linear isotropic material does not take into account the contribution of the plastic strain to deformation. Some issues arise: first of all, is friction the only phenomenon responsible for the residual elongation? Then,

is the elongation solely due to the magnetic force stretching the coils from the turns, or is there a contribution of the plastic conservation of volume? There are indeed other clues that that suggest plastic deformation plays a role in the training process: strain gauges measure a decrease in the residual prestress after consecutive current ramps and quenches. We will propose a model that reproduces this decrease in the preload after subsequent ramps, also correlating its amplitude to the amount of springback.

Besides these elastoplastic aspects of ratcheting, there is also interest in defining the limits of a linear model for the coil analysis. The precompression is easily found for a linear model, but how does this estimate apply to an elastoplastic coil? Besides having a nonlinear characteristic curve, it is a non-conservative material, and is sensitive to all the previous loadsteps, such as precompression, springback and training. Other issues are the discrepancy between the estimates of the peak stress in the linear and elastoplastic model, and the order of magnitude of the residual plastic elongation along the coil axis.

7.2 Model

The analysis focuses on a simplified quadrupole geometry resembling the LARP quadrupole: a coil composed of 8 sector windigs, 30^o each, $20\,mm$ thick with a $90\,mm$ bore. The model is bidimensional, using ANSYS Element 42 enhanced with elatoplastic behaviour, plane strain.

The elastoplastic model uses a 6 points multilinear approximation of the stress–strain curve reaching $200\,MPa$, reproducing the data collected by D. Chichili for *Fermilab-Conf-99/052*. As the data reach a maximum stress of $100\,MPa$, the portion going from $100\,MPa$ to $200\,MPa$ was assumed to be tangent to the data right before $100\,MPa$. The yield stress is assumed to be $8\,MPa$, and the Young Modulus $39\,GPa$.

Options for the hardening law are a kinetc, an isotropic, or a mixed law. We observe from Fig. 7.4 that, while the material yields at very low stress, after hardening it follows a linear pattern for a range of stresses that is much wider than twice the initial yield stress. A kinetic model is therefore not appropriate (Fig. 7.5), and we used an isotropic law (Fig. 7.6).

The coil is constrained radially at the outer radius, and in the azimuthal direction along the horizontal plane (Fig. 7.3). Because the model is not conservative, the whole loading path must be reproduced. First of all the preload of the coil is simulated; the amount of such precopression Δ must be found iteratively as the minimum precompression that prevents the azimuthal amplitude of the coil from changing. The analysis is performed for different

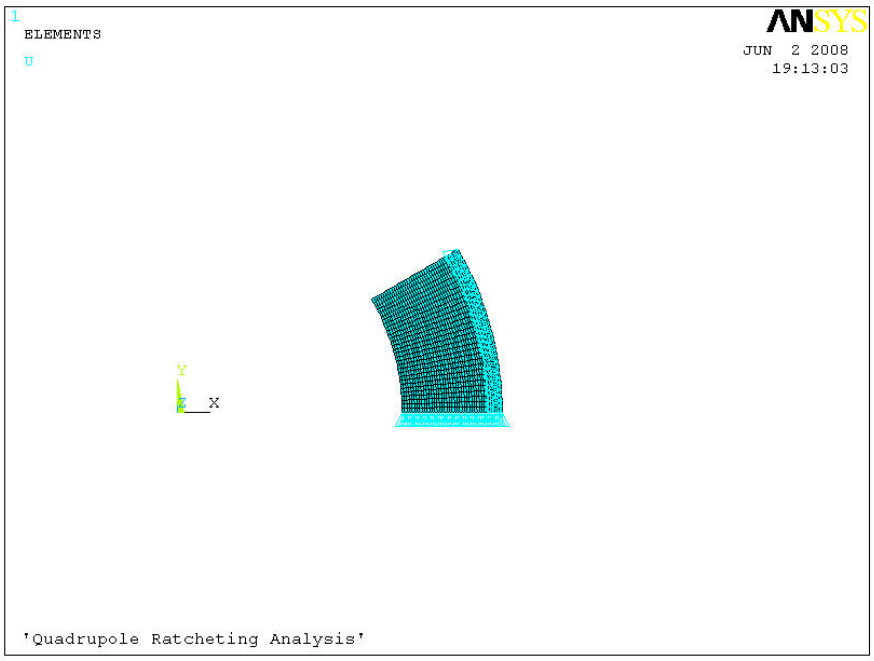

Figure 7.3: Coil sector geometry and constraints.

values of the springback, in order to correlate it to the loss of preload and to the amount of precompression necessary. The model was solved for a springbacks of 0%, 10%, 20%, 30%. Once that the precompression has been reduced to the calculated Δ, the loads are due to the Lorentz force: the first 10 training steps are simulated, approximating a typical training curve with a polynomial function (Fig. 7.7). After each loading, the quench brings all the Lorentz loads back to 0.

The critical current density and the Lorentz force distribution are calculated with the parametric model.

7.3 Results and Conclusions

The phenomenon of ratcheting

The plain strain model shows a residual axial plastic strain on the coil. Its order of magnitude is the same order of magnitude as the experimental residual rod strain measured by [21] (Fig. 7.8(a)). This suggests that axialplastic deformations due to cross–sectional loads play an important part in the phe-

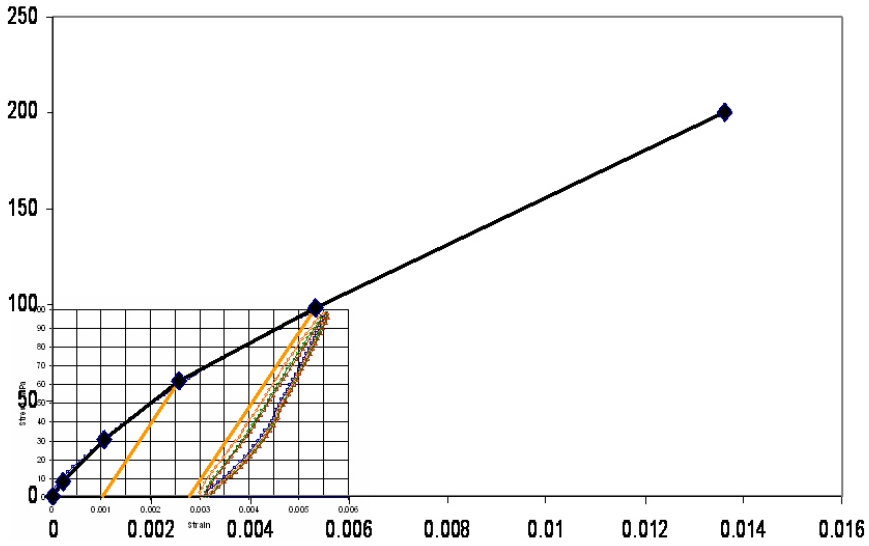

Figure 7.4: A mulilinear model for the material properties.

nomenon known as *ratcheting*.

Focusing on the effects of plasticity on the training process, we reproduced the loss of preload that occurs after consecutive quenches, as an effect of plastic deformation. The loss of prestress, which is a function of the training path, was correlated to the amount of prestress (Fig. 7.9). We notice that the amount of prestress loss decreases sharply with the amount of springback, suggesting that a large springback has a beneficial effect in reducing the uncontrolled variations of the preload during the training process. The preolad variation is negligible for a 30% springback. This phenomenon is easily explained considering that a large springback hardens the material by exploring the "'virgin"' zone which won't induce plastic deforrmations during the training.

There is however a downside of increasing the springback: the higher the springback, the higher the required precompression itself, as shown in Fig. 7.10, showing a sharper increase for higher springback values; e.g., a 30% springback requires a 30% increase in the minimum precompression, causing an overall increase in the maximum compression the coil has to sustain of 70%.

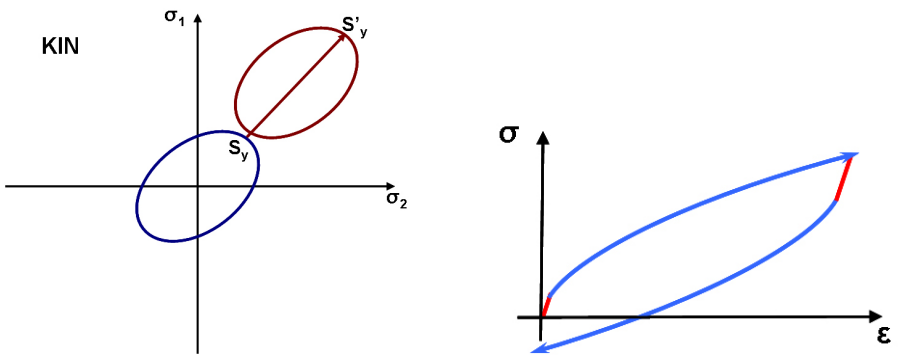

(a) Kinetic hardeing in the Haigh–Westergaard plane.

(b) Kinetic hardening in the $\sigma - \epsilon$ plane.

Figure 7.5: Kinetic hardening.

Table 7.1: Parameters used in the analytical approximation

	$E = 39\,GPa$	$E = 18\,GPa$	Multilinear
$max\,(\sigma_r)$	$68\,MPa$	$68\,MPa$	$69\,MPa$
$max\,(\sigma_\theta)$	$119\,MPa$	$119\,MPa$	$117\,MPa$

Quality of linear estimates

In linear statically indeterminate problems, the stress distribution is not influenced by the Young modulus. The situation is slightly different for coils, which are modeled as both statically determinate and nonlinear, but the change in maximum stress is very mild. First of all, we should determine the Young modulus of the linear coil we use as a reference: a first option is the same Young modulus of the nonlinear coil, $39\,GPa$. Unfortunately this hardly reproduces the stiffness of the material. A second option consists in determining the Young modulus that best approximates the stres–strain curve in the range of interest: $18\,GPa$ (Fig. 7.11).

The two linear models do not show significant difference between each other. Furthermore, the elastoplastic model provides maximum stress estimates that are in substantial accordance with the linear model: as shown in Tab. 7.1 and Fig. 7.12 discrepancies are below 2%.

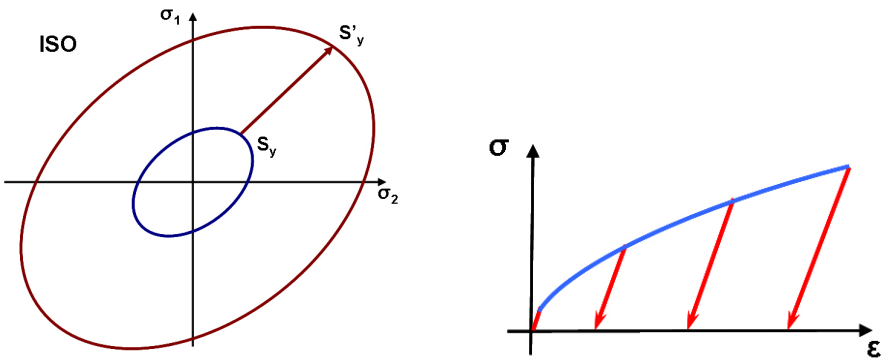

(a) Isotropic hardening in the Haigh–Westergaard plane.

(b) Isotropic hardening in the $\sigma - \epsilon$ plane.

Figure 7.6: Isotropic hardening.

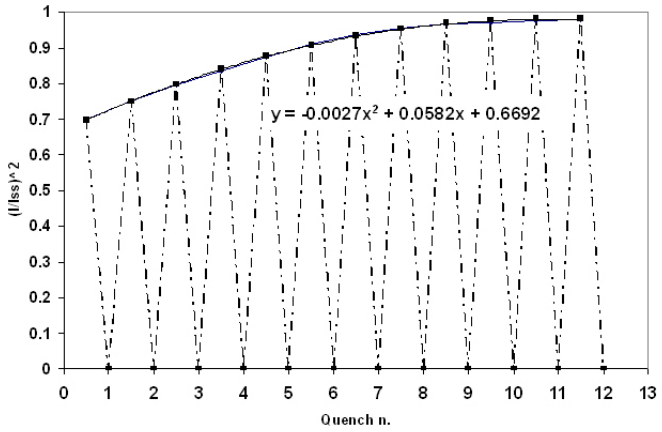

Figure 7.7: Simulation of the training process.

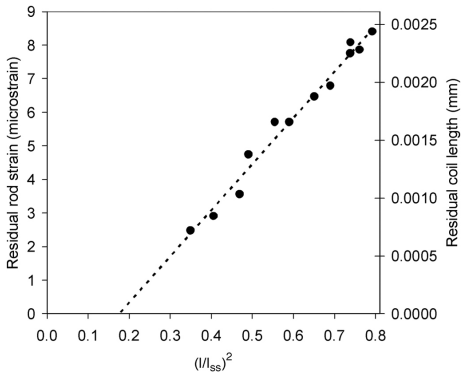

(a) Experimental data from the quadrupole magnet SQ02.

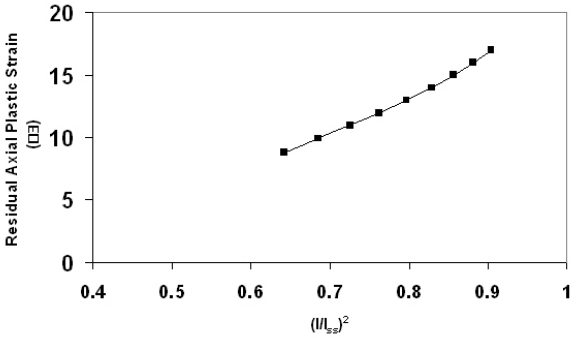

(b) Plastic axial strain in the elastoplastic plane strain model.

Figure 7.8: Comparison of the residual strain in the two models.

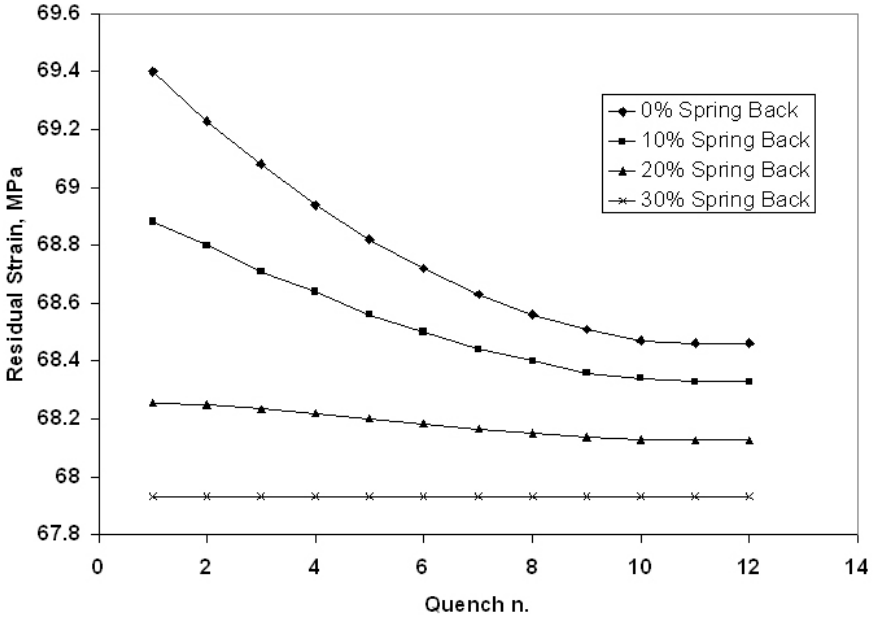

Figure 7.9: Loss of prestress vs quench number.

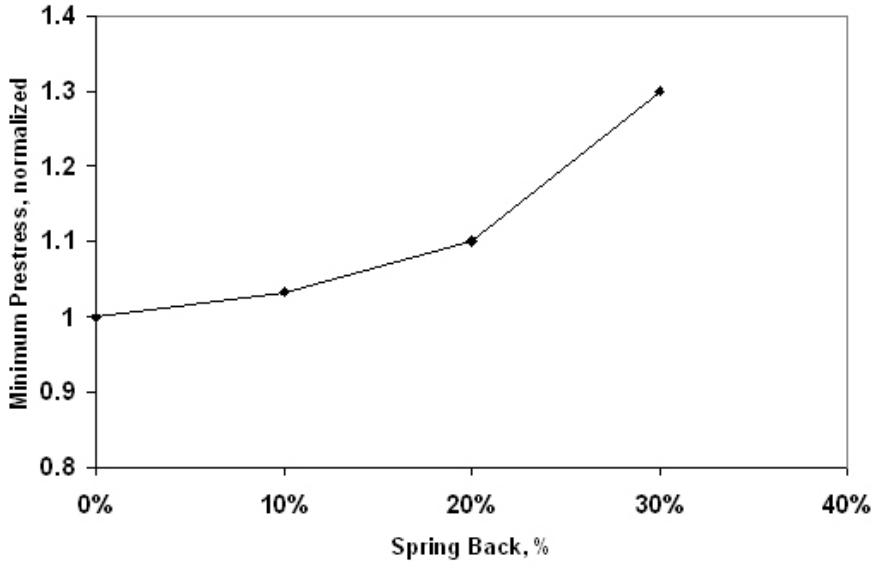

Figure 7.10: Increase of the minimum precompression due to the springback effect.

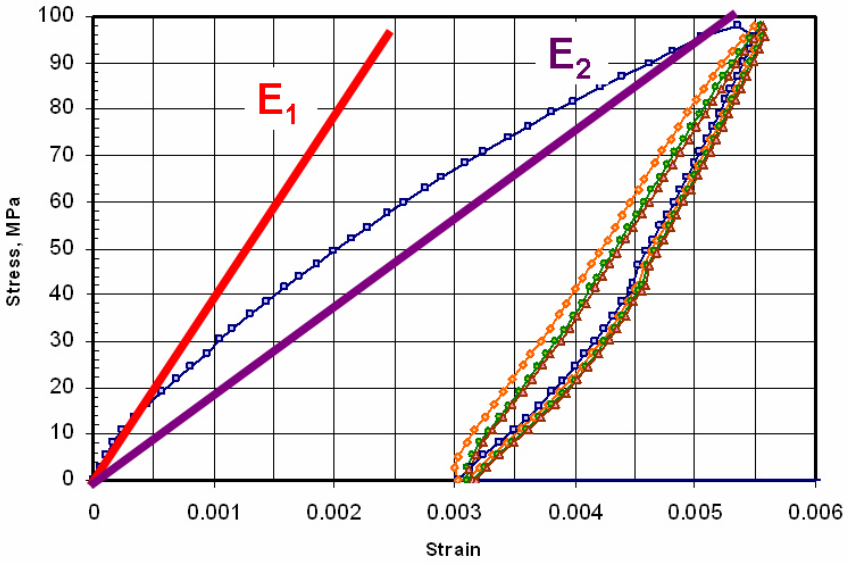

Figure 7.11: Approximation of the Young modulus.

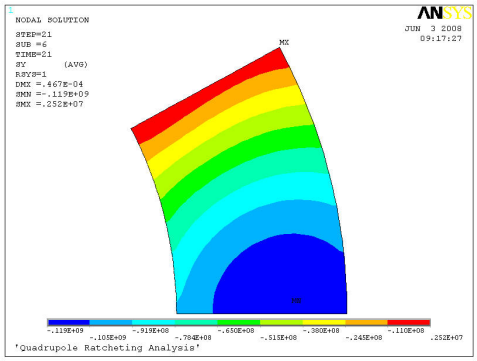

(a) Elastic model, $E = 39\,MPa$.

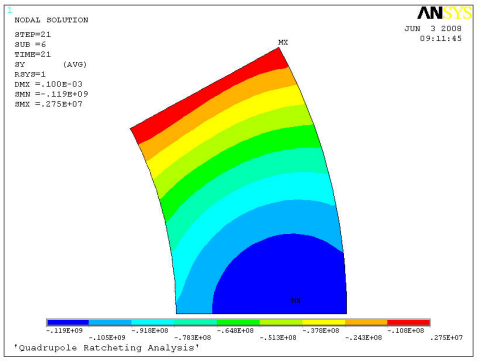

(b) Elastic model, $E = 18\,MPa$.

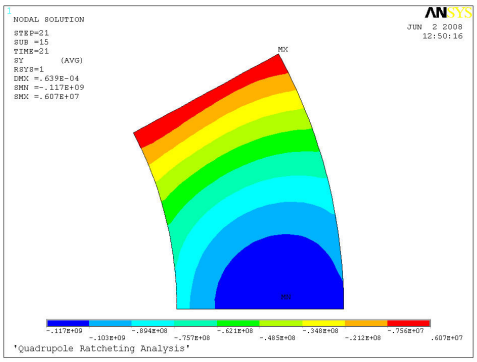

(c) Elastoplastic model.

Figure 7.12: Azimuthal stress distribution.

Chapter 8

Conclusions

Pushing accelerator magnets beyond 10 T holds a promise of future upgrades to machines like the Tevatron at Fermilab and the LHC at CERN. Exceeding the current density limits of $NbTi$ superconductor, Nb_3Sn is at present the only practical superconductor capable of generating fields beyond 10 T. Several Nb_3Sn pilot magnets, with fields as high as 16 T, have been built and tested, paving the way for future attempts at fields approaching 20 T. High current density conductor is required to generate high fields with reduced conductor volume. However this significantly increases the Lorentz force and stress. Future designs of coils and structures will require managing stresses of several 100's of MPa and forces of 10's of MN/m. The combined engineering requirements on size and cost of accelerator magnets will involve magnet technology that diverges from the one currently used with $NbTi$ conductor.

Two recent articles, [14] and [13], performed a parametric analysis to address the relationship between design parameters, superconductor properties, magnet performance and the azimuthal stress. In this work we extended the analysis including the radial stress and finding that, for high performance coils, it will exceed the azimuthal stress. We then devised a simple experiment to determine an equivalent stress for magnet performance. The interaction between the azimuthal and the radial stress was analysed for a wide superconducting quadrupole, concluding that for very high field quadrupoles the radial stress is not only higher, but also inherently involved in determining the quench performance.

A parametric analysis of the electromechanical effects on the field quality was also performed. Finally, we developed an elastoplastic FEM model. It was used to check the results of the parametric model, and to address some of the non–linear phenomena left out of the parametric analysis, such as *ratcheting* and *spring–back*. The results of the elastoplastic model led to a deeper understanding of the correlation between the mounting process of the

magnets and its loss of prestress during the current cycles.

On the whole, we addressed how far the engineering of high field magnets can be pushed, and what are the issues and limitations before such magnets can be used in particle accelerators.

We can summarize some of the main observations that stem from the analyses performed:

- The radial stress is negligible for small coil widths, and it exceeds the azimuthal stresses at high fields and large thicknesses. Larger coil widths will require a model for the equivalent stress. An experiment was proposed in this direction.
- Improvements in magnet performance with increasing coil thickness become negligible when the coil area is already high. A 20 T dipole can hardly be obtained without a substantial effort in the development of Nb_3Sn cable properties.
- At very high fields the effect of the bore diameter on the overall amount of conductor, the peak stress, and the stored energy in dipoles is minor.
- For quadrupoles, the $150\,MPa$ limit is only exceeded for very large apertures ($r_i > 45\,mm$).
- For optimum performance, a quadrupole should be designed in order to have $|\sigma_\theta|_{MAX} = |\sigma_r|_{MAX}$.
- The interaction between aximuthal and radial stress in thick quadrupoles can appropriately be neglected, and the quench performance is affected primarily by the radial stress.
- The amount of prestress loss during the training process decreases sharply with the amount of springback, while the amount of prestress (in mm) increases.
- Linear models provide good estimates of the maximum stress, but gross estimates of strains and displacements.

The models and the results were discussed within the *High Field Magnets Group* at Fermilab and presented at the *Fermilab Accelerator Physics and Technology Seminar* on July 1, 2008.

Bibliography

[1] E. Barzi, T. Wokas, e A. Zlobin, "Sensitivity of Nb/sub 3/Sn Rutherford-type cables to transverse pressure." *Applied Superconductivity, IEEE Transactions on* (2005)15(2 Part 2):1541–1544.

[2] P. Limon et al., "Design Study for a Staged Very Large Hadron Collider." *Fermilab-TM-2149, June* (2001)4.

[3] E. Malamud, "Very arge Hadron Collider." (????).

[4] M. Wilson, "Superconducting materials for magnets." *CERN CAS School on Superconductivity* (1995).

[5] R. Scanlan, D. Dieterich, e H. Higley, "Conductor development for high field dipole magnets." *Applied Superconductivity, IEEE Transactions on* (2000)10(1):288–293.

[6] K. Mess, P. Schmuser, e S. Wolff, *Superconducting Accelerator Magnets*. World Scientific (1996).

[7] C. Boffo, "Magnetization measurements at 4.2 K of multifilamentary superconducting strands." *FNAL technical note* (????)pagine 99–074.

[8] C. Pande e M. Suenaga, "A model of flux pinning by grain boundaries in type-II superconductors." *Applied Physics Letters* (1976)29:443.

[9] E. Gregory, I. Inc, e C. Waterbury, "Conventional wire and cable technology." *Proceedings of the IEEE* (1989)77(8):1110–1123.

[10] S. Foner e B. Scwartz, "Superconductor materials science." *NATO advanced study institute superconducting materials-science and technology* (1981)19.

[11] E. Barzi, G. Ambrosio, P. Bauer, J. Rey, R. Yamada, e A. Zlobin, "Progress report on superconducting strand and cable R&D." *Fermilab, TD-01-013, February* (2001)14.

[12] J. Londenhovius, E. Hornveld, A. den Ouden, W. Wessel, e H. ten Kate, "Progress in the development of Nb 3 Sn conductors based onthe "Powder in tube" method with finer filaments." *Applied Superconductivity, IEEE Transactions on* (1999)9(2):1451–1454.

[13] P. Fessia, F. Regis, e E. Todesco, "Parametric Analysis of Forces and Stresses in Superconducting Quadrupole Sector Windings." *IEEE TRANSACTIONS ON APPLIED SUPERCONDUCTIVITY ASC* (2007)17(2):1269.

[14] S. Caspi e P. Ferracin, "Limits of Nb 3 Sn Accelerator Magnets." *Particle Accelerator Conference, 2005. PAC 2005. Proceedings of the* (2005) pagine 107–111.

[15] J. Brandt, N. Bartlett, R. Bossert, J. Carson, J. Konc, G. Lee, J. Cook, S. Caspi, M. Gordon, e F. Nobrega, "Coil end design for the SSC collider dipole magnet." *Particle Accelerator Conference, 1991. Accelerator Science and Technology., Conference Record of the 1991 IEEE* (6-9 May 1991)pagine 2182–2184 vol.4.

[16] K. Mess, P. Schmuser, e S. Wolff, *Superconducting Accelerator Magnets*. World Scientific (1996).

[17] E. Kramer, "Scaling laws for flux pinning in hard superconductors." *Journal of Applied Physics* (2003)44:1360.

[18] L. Summers, M. Guinan, J. Miller, e P. Hahn, "A model for the prediction of Nb 3 Sn critical current as a function of field, temperature, strain, and radiation damage." *Magnetics, IEEE Transactions on* (1991) 27(2):2041–2044.

[19] E. Todesco e L. Rossi, "An Estimate of the Maximum Gradients in Superconducting Quadrupoles." *IEEE TRANSACTIONS ON APPLIED SUPERCONDUCTIVITY ASC* (2007)17(2):1153.

[20] H. Brechna, "Superconducting Magnet Systems." *New York* (????).

[21] P. Ferracin, S. Caspi, e A. Lietzke, "Towards Computing Ratcheting and Training in Superconducting Magnets." *Applied Superconductivity, IEEE Transactions on* (2007)17(2 Part 2):2373–2376.

[22] A. Devred, "Quench origins." *AIP Conference Proceedings* (1992) 249:1262.

[23] S. WIPF, "Stability and degradation of superconducting current-carrying devices." Rapporto tecnico, LA-7275, Los Alamos Scientific Lab., NM (USA) (1978).

[24] M. Wilson, R. Wolf, e G. CERN, "Calculation of minimum quench energies in Rutherford cables." *Applied Superconductivity, IEEE Transactions on* (1997)7(2):950–953.

[25] S. Caspi, W. Gilbert, W. Hassenzahl, G. Lambertson, R. Meuser, J. Rechen, R. Schafer, e R. Warren, "Mechanical and helium cooling factors in dipole magnet training." *Magnetics, IEEE Transactions on* (1981)17(1):443–446.

[26] S. Caspi, R. Meuser, e R. Wolgast, "Mechanical properties of Nb 3 Sn stranded superconducting potted cable windings." *Magnetics, IEEE Transactions on* (1983)19(3):728–732.

[27] C. Chichili, T. Arkan, e I. Terechkine, "Niobium-Tin Magnet Technology Development at Fermilab." (1999).

[28] D. Chichili, J. Hoffman, e A. Zlobin, "Investigation of alternative materials for impregnation of Nb/sub 3/Sn magnets." *Applied Superconductivity, IEEE Transactions on* (2003)13(2):1792–1795.

[29] D. Chichili, T. Arkan, J. Ozelis, e I. Terechkine, "Investigation of cable insulation and thermo-mechanical propertiesof epoxy impregnated Nb 3 Sn composite." *Applied Superconductivity, IEEE Transactions on* (2000) 10(1):1317–1320.

[30] K. Chow e G. Millos, "Measurements of modulus of elasticity and thermal contraction ofepoxy impregnated niobium-tin and niobium-titanium composites." *Applied Superconductivity, IEEE Transactions on* (1999) 9(2 Part 1):213–215.

[31] K. Couturier, P. Ferracin, W. Scandale, E. Todesco, e D. Tommasini, "Thermomechanical properties of the coil of the superconducting magnets for the Large Hadron Collider." *Applied Superconductivity, IEEE Transactions on* (2002)12(2):1804–1812.

[32] P. Ferracin, W. Scandale, E. Todesco, D. Tommasini, L. Div, e G. CERN, "Modeling of coil pre-stress loss during cool-down in the main dipoles of the Large Hadron Collider." *Applied Superconductivity, IEEE Transactions on* (2002)12(1):1705–1708.

[33] P. Fessia e I. Canseco, "3D FEM Modeling of the Moil Ends of the LHC Main Dipole." *Applied Superconductivity, IEEE Transactions on* (2006) 16(2):1290–1293.

[34] S. CASPI, P. FERRACIN, e S. GOURLAY, "Graded high field Nb? 3 ?Sn dipole magnets." *IEEE transactions on applied superconductivity* (2006)16(2):354–357.

[35] M. Reytier, A. Devred, M. Durante, C. Gourdin, e P. Vedrine, "Characterization of the thermo-mechanical behavior of insulatedcable stacks representative of accelerator magnet coils." *Applied Superconductivity, IEEE Transactions on* (2001)11(1 Part 3):3066–3069.

[36] A. Devred, T. Bush, R. Coombes, J. DiMarco, C. Goodzeit, J. Kuzminski, M. Puglisi, P. Radusewicz, P. Sanger, R. Schermer, et al., "About the mechanics of SSC dipole magnet prototypes." *AIP Conf. Proc* (1992) 219:1309–1374.

[37] J. Cortella, A. Devred, e A. Wandesforde, "Mechanical performance of full-scale prototype quadrupole magnetsfor the SSC." *Applied Superconductivity, IEEE Transactions on* (1993)3(1):699–704.

[38] R. Meuser, "Magnetic field for a thick cos-nθ winding." *Engineering Note M* (????)5254.

[39] R. Meuser, "Stress in thick cos-nθ winding." *Engineering Note M* (????) 5256.

[40] A. Asner, "Cylindrical Aperture Multipoles with Constant Current Density Sector Windings." *CERN, SI/Note MAE/69-15* (????).

[41] F. Asner, *High Field Superconducting Magnets*. Oxford University Press (1999).

[42] A. Zlobin, G. Ambrosio, N. Andreev, E. Barzi, B. Bordini, R. Bossert, R. Carcagno, D. Chichili, J. DiMarco, L. Elementi, et al., "R&D of Nb/sub 3/Sn accelerator magnets at Fermilab." *Applied Superconductivity, IEEE Transactions on* (2005)15(2 Part 2):1113–1118.

[43] G. Ambrosio, N. Andreev, T. Arkan, E. Barzi, D. Chichili, V. Kashikhin, P. Limon, T. Ogitsu, J. Ozelis, I. Terechkine, et al., "Conceptual design of the Fermilab Nb 3 Sn high fielddipole model." *Particle Accelerator Conference, 1999. Proceedings of the 1999* (1999)1.

[44] S. Caspi e P. Ferracin, "Toward Integrated Design and Modeling of High Field Accelerator Magnets." *Applied Superconductivity, IEEE Transactions on* (2006)16(2):1298–1303.